



HAL
open science

Reinforced concrete structures: A review of corrosion mechanisms and advances in electrical methods for corrosion monitoring

Romain Rodrigues, Stephane Gaboreau, Julien Gance, Ioannis Ignatiadis, Stéphanie Betelu

► To cite this version:

Romain Rodrigues, Stephane Gaboreau, Julien Gance, Ioannis Ignatiadis, Stéphanie Betelu. Reinforced concrete structures: A review of corrosion mechanisms and advances in electrical methods for corrosion monitoring. *Construction and Building Materials*, 2020, pp.121240. 10.1016/j.conbuildmat.2020.121240 . hal-02979786v2

HAL Id: hal-02979786

<https://brgm.hal.science/hal-02979786v2>

Submitted on 27 Dec 2022

HAL is a multi-disciplinary open access archive for the deposit and dissemination of scientific research documents, whether they are published or not. The documents may come from teaching and research institutions in France or abroad, or from public or private research centers.

L'archive ouverte pluridisciplinaire **HAL**, est destinée au dépôt et à la diffusion de documents scientifiques de niveau recherche, publiés ou non, émanant des établissements d'enseignement et de recherche français ou étrangers, des laboratoires publics ou privés.

1 Reinforced concrete structures: a review of corrosion mechanisms and
2 advances in electrical methods for corrosion monitoring

3 Romain Rodrigues^a, Stéphane Gaboreau^b, Julien Gance^a, Ioannis Ignatiadis^b, Stéphanie Betelu^{b*}

4 ^a: IRIS Instruments, 1 avenue Buffon, 45100 Orléans, France.

5 ^b: BRGM (French Geological Survey), 3 avenue Claude Guillemin, 45060 Orléans Cedex 2, France.

6 * Corresponding author:

7 Stéphanie Betelu: s.betelu@brgm.fr

8 **Abstract**

9 Steel corrosion is the main cause of deterioration of reinforced concrete (RC) structures. We provide
10 an up-to-date review on corrosion mechanisms and recent advances in electrical methods for
11 corrosion monitoring. When assessing corrosion mechanism, the inherent heterogeneity of RC
12 structures and the significant effect of environmental factors remain major issues in data
13 interpretations. The steel surface condition and local inhomogeneities at the steel-concrete interface
14 appear to have an important effect on corrosion initiation. Considering uniform corrosion in
15 atmospherically exposed reinforced concrete, the two main influencing factors of the corrosion
16 process are the water content and the pore structure at the steel-concrete interface. However,
17 irrespective of the depassivation mechanism, i.e. carbonation or chloride-induced corrosion, non-
18 uniform corrosion is expected to be the main process for RC structures due to local variations in
19 environmental exposure or the presence of interconnected rebars with different properties. Future
20 studies may then be focused on their effect on macrocell corrosion to gain further insights in the
21 corrosion mechanisms of RC structures. Concerning corrosion monitoring using electrical methods, the
22 half-cell potential technique with potential mapping is accurate for locating areas with a high corrosion
23 risk. Recent developments in the measurement of concrete resistivity have shown that the use of
24 electrical resistivity tomography allows to consider appropriately the inherent heterogeneity of
25 concrete and provides more insights on transport phenomena (e.g. water and salts ingress) in the
26 material. Nevertheless, during the corrosion propagation stage, the polarization resistance remains
27 the most important parameter to be determined as it provides quantitative information of the
28 corrosion rate. If conventional three-electrode configuration methods can supply an accurate
29 determination in the case of uniform corrosion, they often fail in the case of macrocell corrosion in
30 field experiments. Recent advances have shown that a four-electrode configuration without any
31 connection to the rebar can rather be used for the non-destructive testing and evaluation of corrosion.
32 If studies are still required to quantify the corrosion rate, this method appears sensitive to localized
33 corrosion and thus more suitable to field investigations. Finally, the coupling of numerical simulations
34 with complementary electrical and other non-destructive testing methods is essential for consolidating
35 the results to provide a better diagnosis of the service life of RC structures.

36 **Keywords:** steel-reinforced concrete; carbon steel; corrosion mechanism; corrosion rate; non-
37 destructive testing.

38 **1. Introduction**

39 Concrete and cement-based materials are among the main man-made materials used world-wide in
40 both civil and industrial structures, due to their high mechanical strength and low porosity.
41 Reinforcement with steel rebars has improved the performance of structural elements without
42 modifying the macroscopic cementitious matrix properties [1]. Properly designed and adapted to its
43 environment, reinforced concrete (RC) is an extremely durable material as the concrete is a protective
44 barrier for the rebars. This allowed the development of RC structures, such as bridges, dams or nuclear
45 powerplants [2–4]. Nevertheless, such materials degrade over time, becoming more fragile.

46 One of main fragilities is related to corrosion of the steel rebars, an electrochemical process that
47 involves the anodic dissolution of iron and the cathodic reduction of oxygen, the pore solution of
48 concrete acting as the electrolyte. This phenomenon develops under the influence of aggressive
49 agents, e.g. CO₂ and Cl⁻, that infiltrate the concrete up to the rebar [5–9]. The degradation of the
50 protective layer formed on steel surface in sound concrete results in accelerated corrosion of the rebar,
51 affecting progressively the performance of RC structures. The resulting corrosion products precipitate
52 and generate tensile stress, promoting the appearance of cracks to an unacceptable level regarding
53 their service life [5–9]. Such degradation can result in the collapse of structures such as bridges or
54 buildings. When the first cracks are noticed on the concrete surface, corrosion has generally reached
55 an advanced stage and maintenance action is required. The continuous aging of structures created
56 several decades ago results in aggravated situations as many operate beyond their service life,
57 drastically increasing the economic impact of corrosion [10,11]. The control of such infrastructures is
58 thus of major importance, requiring reliable monitoring techniques that can be used without
59 disturbing the integrity of the structures.

60 Several techniques have been developed for understanding the mechanism and kinetics of the
61 corrosion of steel in concrete. Some techniques focus on determining concrete properties for
62 evaluating the ingress of aggressive agents, while others focus on the rebar properties [12–21]. Among
63 such techniques, electrical/electrochemical methods have been widely developed as they allow the
64 evaluation of the corrosion rate, which is essential when determining the need for future maintenance
65 of RC structures once the steel rebar is depassivated. Three main parameters are generally determined
66 for assessing this parameter: corrosion potential, concrete resistivity, and polarization resistance.

67 This review describes first the constituents of RC structures, i.e. cement-based materials, carbon steel
68 rebar and steel-concrete interface. We then present didactically an up-to-date knowledge of corrosion
69 mechanisms of steel in concrete as a prerequisite to appropriate the different phenomena and
70 evaluate the main factors influencing the corrosion rate. The review is then focused on the use of
71 electrical methods for the non-destructive testing and evaluation (NDT) of corrosion, with the current
72 state-of-the-art monitoring techniques, their advantages and drawbacks, and recent advances in
73 indirect electrical methods which do not required any connection to the reinforcement for the
74 assessment of corrosion, which have been largely ignored in recent reviews. The interest of combining
75 several NDT for field inspection is also developed to overcome the limitation of measuring
76 instantaneous corrosion rates and to improve the estimation of the service life of RC structures. Finally,
77 we present conclusions and perspectives for future researches in corrosion science and engineering.

78 2. Composition of reinforced concrete structures

79 2.1. Cement-based materials

80 Cement-based materials are composed of binder (hydrated cement) and aggregates of different sizes
81 and compositions. Cement is produced by heating a mixture of limestone and raw clay minerals (or
82 other materials of similar bulk composition) [22]. Though OPC was the most common cement-based
83 material used world-wide over the past decades, other cement formulations have been designed to
84 adapt the materials to their environmental setting. Organic and inorganic admixtures act on the
85 workability of cement-based materials or improve their performance. Supplementary cementitious
86 materials (SCMs), such as fly ash or blast furnace slag (BFS) [23,24], are also used as partial replacement
87 of clinker for reducing waste and greenhouse-gas emissions, as the cement industry is one of the
88 largest CO₂ emitters in the world [25]. Such materials differ in their microstructure and macroscopic
89 behaviour, but their description fall outside the scope of this review.

90 The reaction of cement with water, called hydration, results in the formation of a hydrated cement
91 paste (HCP). The latter is composed of many hydration products, e.g. calcium silicate hydrates (C-S-H)
92 and portlandite Ca(OH)₂, but also unhydrated cement particles [26–28]. Over a variable curing period,
93 the cement develops its physical and chemical properties. In laboratory experiments, curing can take
94 place under optimal conditions in terms of relative humidity (RH) and temperature, which allows the
95 definition of standard specimens for research purposes [29]. However, curing conditions are often
96 difficult to control in the field, for which reason a different standard practice has been proposed [30].
97 Hence, the results obtained from laboratory samples must be used with special care if the objective is
98 to extrapolate them to real structures as their intrinsic properties may significantly differ.

99 After curing, C-S-H represents ~50-60% of the weight of HCP and is responsible for its cohesion [31]; it
100 consists of lamellar nanoparticles with negatively charged silicate layers compensated by interlayer
101 calcium ions, the charge depending on the calcium-to-silica ratio [32]. Their surface chemistry and
102 inter-particles interaction are the driving force of the cohesive properties of hydrated cement,
103 controlling the interactions with charged molecules [31,33]. The role of confined water in C-S-H
104 micropores was demonstrated through molecular dynamic simulation [34,35]. Because of these
105 points, understanding the distribution of water in C-S-H and their thermodynamic and hydration
106 properties is of prime importance when considering the strength and transfer properties of cement
107 materials [36–41]. Nonetheless, all the hydrates must be considered as they play a role in the cement-
108 paste properties.

109 Over the service life of a structure, different thermodynamic equilibria between the solid and liquid
110 phases will develop in the cement-based material, governed by both its environmental setting and its
111 degradation level [42]. The solubility of each phase will dictate the composition of the pore water [43].
112 At an early stage, the pore solution pH is highly alkaline, between 12.5 and 13.5. With the leaching and
113 dissolution of the materials by chemical attacks, portlandite maintains a pH of about 12.5. During the
114 third stage, the pore solution pH is essentially controlled by C-S-H and is buffered in the range 12.5 to
115 10 [44]. Finally, at later stage, the pH is controlled by all stages of concrete degradation.

116 At a macroscopic scale, both microstructure and reactivity of hydrates control the physical and
117 chemical reactions affecting the durability of cement-based materials. The microstructure of the
118 cement paste is highly heterogeneous through the coagulation of nanometric hydrates whose
119 heterogeneities range from macroscopic to nanoscopic scales. In addition to the intra-particles (micro)

120 and inter-particles (meso) porosity of hydrates, the microstructure consists of capillary pores which
121 can range from nanometres up to millimetres. The volume and size of these macropores depend upon
122 the water-to-cement (w/c) ratio, the size of the aggregates and the degree of hydration [45–50]; they
123 are mainly interconnected through a mesoscopic pore network. The presence of aggregates in cement-
124 based materials also introduces important changes with the formation of additional porous regions,
125 known as interfacial transition zones (ITZs). As ITZ may in part be caused by artefacts from sample
126 preparation for microscope analysis, e.g. edge rounding, scratches or imperfect cuts, the experimental
127 protocol for specimen preparation must be reported to avoid any misleading [51].

128 Cracks also are important features in the microstructure of concrete, introducing additional porosity
129 in HCP. Cracks and microcracks are caused by a multitude of different physical and chemical processes,
130 such as mechanical loading, shrinkage, creep, thermal variations, and expansive chemical reactions
131 [22]. To some extent, almost all cementitious materials are affected by one or more of these processes
132 at different times and, consequently, cracks are endemic to the material. A good knowledge of the
133 structure and microstructure of the concrete is thus essential for assessing concrete durability.
134 Notably, the determination of pore throat and pore size distribution is required for assessing the
135 constrictivity and tortuosity of concrete. Both parameters are mainly determined by mercury intrusion
136 porosimetry (MIP) [52], kerosene porosity, or by imaging methods, e.g. backscattered electron (BSE)
137 imaging [28,53–55] and X-ray micro-computed tomography (X-ray μ CT) [56,57]. The last technique is
138 also used for estimating the size and distribution of aggregates in the structure. Spectral induced
139 polarization can also provide relevant information on the mean pore size, pore size distribution and
140 connected porosity of low pH concrete [58].

141 **2.2. Carbon steel reinforcement bars**

142 The role of steel reinforcement bars (rebars) is to improve the mechanical properties of the structure,
143 as they provide tensile strength, ductility and crack-growth resistance [1]. Several types of rebar can
144 be used, e.g. carbon steel, epoxy-coated steel, galvanized steel, stainless steel and different alloy
145 steels, but only carbon steel is considered in this review. Generally, ribbed rebars are used in RC
146 structures to provide a strong and interlocking connection between steel and concrete.

147 The chemical composition—metallic and non-metallic elements—of the rebar may vary considerably
148 as several steel grades exist in the world. The distribution of the microstructural phases of steel, e.g.
149 ferrite, cementite, pearlite, martensite, austenite and/or bainite, and the presence of lattice defects
150 or inclusions (e.g. manganese sulphide MnS) can influence corrosion susceptibility, but only few
151 studies are available on this purpose for the corrosion in cement-based materials. If the influence of
152 steel microstructure on corrosion susceptibility has been demonstrated under immersed conditions in
153 simulated concrete pore solution [59–62], the ferritic-martensitic microstructure having generally a
154 better corrosion resistance, the effect of non-uniform water distribution in porous material exposed
155 to atmospheric conditions must be investigated to determine the corrosion susceptibility in concrete.

156 After hot rolling and forging, a thin and brittle oxide coating called *mill scale* spontaneously forms on
157 steel surface. It is mainly composed of wüstite (FeO), magnetite (Fe₃O₄), hematite (α -Fe₂O₃) and
158 maghemite (γ -Fe₂O₃) [63]. A *native rust* layer later forms during transport, handling and storage of the
159 rebar. Some defects such as cracks, voids and crevices are common between the steel and these initial
160 oxide layers [64]. The composition, thickness and electrochemical properties of both mill scale and
161 native rust are thus very different from one steel to another due to the different manufacturing
162 processes [63–65]. Consequently, even the as-received grade is not well defined, which creates

163 difficulties for ensuring reproducibility of the measurements [65]. If mill scale and native rust can be
164 removed by different processes, e.g. sandblasting, chemical cleaning or mechanical polishing [66], the
165 results from such processes must be used with special care as they are generally not performed for
166 engineered structures.

167 The role of mill scale and native rust layer on the corrosion resistance of steel is still unclear [67–69].
168 Some studies indicate that it does not affect the corrosion rate or may have a beneficial effect due to
169 the protective behaviour of the layer in the case of a dense and uniform mill scale [70,71], but most
170 studies affirm that it has a negative effect on the corrosion rate as it inhibits the development of an
171 effective passive layer on the rebar or decreases its electrical resistance [72–77]. It was also shown
172 that the corrosion rate is greater for rebars exposed to natural weathering (pre-rusted rebars) than for
173 the as-received rebars [78]. The initial surface state of the rebar and the distribution of native rust are
174 thus major parameters controlling the corrosion susceptibility, and a non-uniform mill scale layer can
175 create weak points for corrosion initiation [79,80]. Hence, as for cement-based materials, a detailed
176 description of the rebar grade, composition, microstructure and initial surface condition is necessary
177 for a correct interpretation of the data and the development of database for the assessment of
178 corrosion mechanisms.

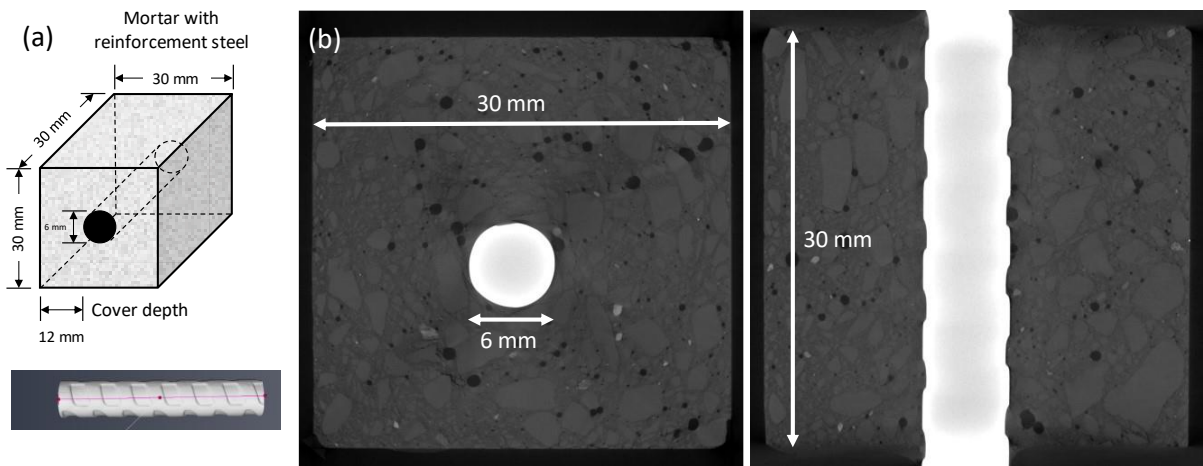
179 **2.3. Steel-concrete interface**

180 The steel-concrete interface is the most important part of the structure when it comes to determining
181 corrosion mechanisms and corrosion rates of steel rebar [63,80,81]. The embedding of steel in
182 concrete is intended to protect the steel from corrosion. Indeed, in the alkaline medium of the pore
183 solution, a passive film forms spontaneously on the steel surface during the first days/weeks of
184 exposure [82–84]. Such passivation is initiated by the formation of adsorbed species (FeOH_{ads} and
185 $\text{Fe}(\text{OH})_{\text{ads}}^+$, HFeO_2^- and $\text{Fe}(\text{OH})_2$ [85]), and the aging of this passive film results in a progressive decrease
186 in the corrosion rate to values below $0.1 \mu\text{m year}^{-1}$ (often described as “no corrosion takes place”). This
187 change is attributable to thickening of the film and to the decrease in Fe^{2+} content in its inner layer
188 [86,87], which corresponds to the oxidation of magnetite Fe_3O_4 to Fe(III) oxide and oxyhydroxide, e.g.
189 Fe_2O_3 or FeOOH [88–90]. The passive film shows an *n*-type semiconductive behaviour [91,92], but this
190 reaction results in decreasing the electronic conductivity of the film, as Fe(III) oxides are less
191 conductive than magnetite [90]. The resulting passive film is about 10-15 nm thick and is mainly
192 composed of iron oxides and oxyhydroxides, with a progressive increase in valence state and in
193 hydroxide content from inner to outer interface [87,93]. Some elements of the cement paste, e.g. Ca^{2+} ,
194 Na^+ and K^+ , can also occur in the passive film, affecting its properties [94,95].

195 The concrete part of the interface can be seen as another ITZ [63]. The casting direction and orientation
196 of the rebar in the structure affect the distribution of $\text{Ca}(\text{OH})_2$ and the porosity of HCP at the steel-
197 concrete interface. For example, the area under a horizontal rebar is exposed to very different
198 conditions, having a $\text{Ca}(\text{OH})_2$ content close to 0 and a much higher porosity than the bulk concrete
199 [96,97]. Conversely, for vertical rebars, the steel-concrete interface is relatively uniform without
200 obvious macroscopic defects [97,98]. This difference is explained by the settlement, segregation and
201 bleeding of fresh concrete that can result in the accumulation of defects under horizontal rebar [98].
202 When several horizontal rebars are present in the structure, the upper ones have generally more
203 defects, which is known as the top-bar effect. Special attention must be paid during concrete pouring
204 to limit the formation of these defects that can be preferential seat for corrosion initiation. Other
205 defects, such as cracks, slips and separations, are the result of tensile load on the structure [63]. They

206 all affect the quality of the interface, and thus the corrosion rate [99]. The coalescence of ITZs and
207 cracks can form interconnected porous channels that dramatically increase concrete permeability,
208 creating preferential pathways for the ingress of aggressive agents to the rebar. Finally, the use of
209 spacers and the presence of welding spots can induce supplementary local heterogeneities.

210 The local characteristics of the steel-concrete interface are important parameters as the latter is the
211 seat of the corrosion process. Several techniques can be used to determine the chemistry and
212 microstructure of the interface, such as EDS and BSE imaging [96,100,101]. Special care must be done
213 during sample preparation for such analyses to reduce as much as possible any damage to the steel-
214 concrete interface [102,103]. Alternatively, X-ray μ CT can be used to examine non-destructively the
215 rebar/cement contact and any heterogeneities such as air voids (Fig. 1).

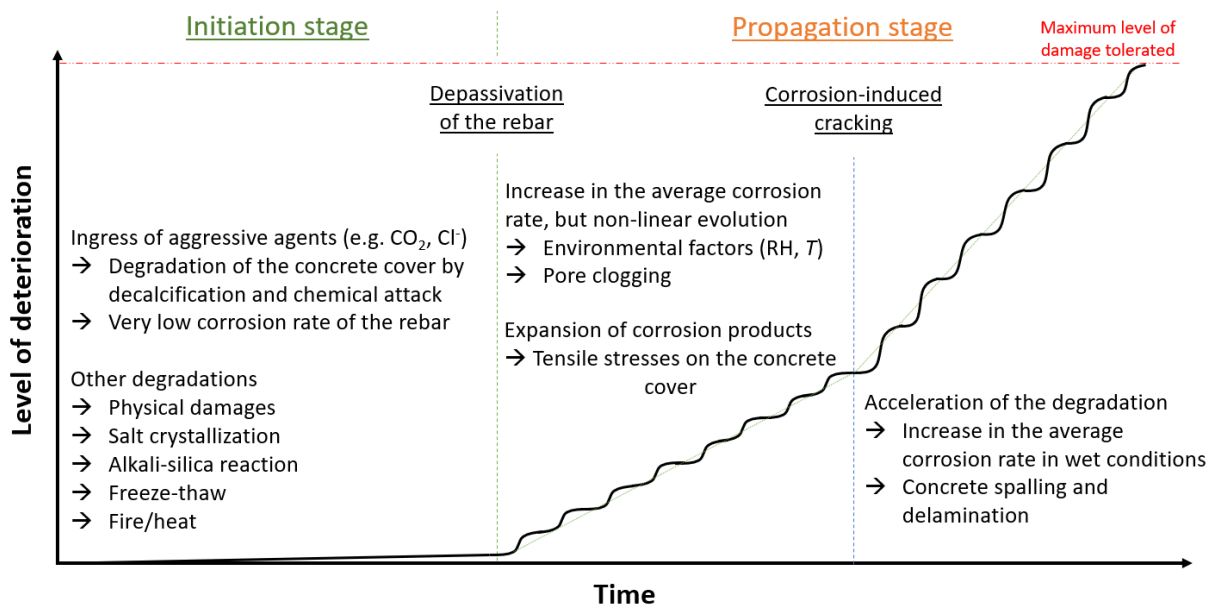


216

217 **Figure 1.** (a) Schematic representation of a mortar sample [cement (CEM I 52.5 R, Lafarge)=25 wt%, sand (0-
218 4 mm)=75 wt%, w/c ratio=0.5] with one ribbed black carbon steel rebar ($\Phi=6$ mm). (b) X-ray micro-computed
219 tomography 2D slices acquired under 140 kV and a 26 μ m voxel size. The slices show concrete heterogeneities
220 (shape and orientation of the aggregates, presence of air bubbles), the shape of the rebar and the structure of
221 the steel-concrete interface. Courtesy: S. Gaboreau.

222 **3. Corrosion mechanisms of carbon steel in concrete**

223 As proposed by Tuutti [104], the service life of RC structures can be divided into two main time periods:
224 an initiation stage and a propagation stage. The first corresponds to the ingress of aggressive agents—
225 CO₂ and chloride—in the concrete to the rebar, resulting in a progressive disruption of the passive film
226 on the steel surface. The propagation stage is the active state of corrosion until the degree of corrosion
227 reaches the damage limit tolerated by building standards. Generally, steel corrosion is considered in a
228 passive state if the current density is below 0.1 μA cm⁻², and in the active state for values over 1 μA
229 cm⁻² [105]. Based on Tuutti’s model, other models considered the change in corrosion rate during the
230 service life of reinforced concrete [106–108], or included additional stages for differentiating rust
231 expansion, cover cracking and spalling/delamination in the definition of service life (Fig. 2) [109–111].
232 However, the level of deterioration is not linear as concrete cracking and spalling may accelerate the
233 corrosion rate, whereas the production of corrosion products in cracked concrete may fill the pores,
234 thus decreasing the corrosion rate.



235
236 **Figure 2.** Schematic representation of the service life of RC structures, adapted from Tuutti’s diagram [106].

237 Estimating the service life of reinforced concrete requires knowledge of the two main stages of steel
238 corrosion in concrete [112]. Notably, models coupling transport and electrochemical processes are
239 required for improving the prediction of service life [111,113]. Hereafter we discuss the
240 thermodynamic and kinetic aspects of corrosion, the mechanisms of carbonation- and chloride-
241 induced corrosion—here developed separately but locally occurring simultaneously—and the
242 formation and consequence of iron corrosion products on the durability of RC structures. Table 1
243 summarizes the main conclusions of this section.

244 **Table 1.** Summary of the main conclusion regarding mechanisms of carbonation- and chloride-induced corrosion of steel in concrete.

Mechanism	Corrosion initiation	Corrosion propagation	Main corrosion products
Carbonation	<ul style="list-style-type: none"> * Ingress of CO₂ from the atmosphere <li style="padding-left: 20px;">Higher penetration rate in the 50-70% RH range <li style="padding-left: 20px;">Dissolution in water as carbonic acid * Decalcification of concrete <li style="padding-left: 20px;">Reaction with Ca-bearing hydrated phases <li style="padding-left: 20px;">Non-uniform carbonation front <li style="padding-left: 20px;">Decrease in the pH of the pore solution * Depassivation of the rebar 	<ul style="list-style-type: none"> * Corrosion rate is mainly influenced by the water content and the pore size distribution in the vicinity of the rebar for atmospherically exposed RC structures * Volume expansion of corrosion products <li style="padding-left: 20px;">Pore clogging <li style="padding-left: 20px;">Tensile stress in the concrete cover <li style="padding-left: 20px;">Formation of corrosion-induced cracks <li style="padding-left: 20px;">Increase in the average corrosion rate <li style="padding-left: 20px;">Concrete spalling and delamination 	<ul style="list-style-type: none"> * <u>Intermediate products:</u> <li style="padding-left: 20px;">Chukanovite Fe₂(OH)₂CO₃ <li style="padding-left: 20px;">Carbonate green rust GR(CO₃²⁻) <li style="padding-left: 20px;">Siderite FeCO₃ * <u>Final products:</u> <li style="padding-left: 20px;">Magnetite Fe₃O₄ <li style="padding-left: 20px;">Goethite α-FeOOH <li style="padding-left: 20px;">Lepidocrocite γ-FeOOH
Chloride	<ul style="list-style-type: none"> * Ingress of Cl⁻ from marine environment or the use of de-icing salts <li style="padding-left: 20px;">Non-uniform penetration of Cl⁻ in the material up to the rebar <li style="padding-left: 20px;">Series of depassivation/repassivation until the chloride content is high enough * Depassivation of the rebar 	<ul style="list-style-type: none"> * Autocatalytic mechanism of pitting <li style="padding-left: 20px;">Deepest pits are generally observed in the vicinity of interfacial air voids <li style="padding-left: 20px;">Formation of macrocell with high corrosion rates * Volume expansion of corrosion products <li style="padding-left: 20px;">Pore clogging <li style="padding-left: 20px;">Tensile stress in the concrete cover <li style="padding-left: 20px;">Formation of corrosion-induced cracks <li style="padding-left: 20px;">Increase in the average corrosion rate <li style="padding-left: 20px;">Concrete spalling and delamination 	<ul style="list-style-type: none"> * <u>Intermediate products:</u> <li style="padding-left: 20px;">Ferrous hydroxychloride <li style="padding-left: 20px;">Chloride green rust GR(Cl⁻) * <u>Final products:</u> <li style="padding-left: 20px;">Magnetite Fe₃O₄ <li style="padding-left: 20px;">Goethite α-FeOOH <li style="padding-left: 20px;">Lepidocrocite γ-FeOOH <li style="padding-left: 20px;">Feroxyhyte δ-FeOOH <li style="padding-left: 20px;">Akaganeite β-FeOOH (Cl⁻ excess)
Combined	<ul style="list-style-type: none"> See above Carbonation of Friedel's salt and other chloride-binding phases will release free Cl⁻ [114–116] 	<ul style="list-style-type: none"> See above The corrosion rate is higher when both Cl⁻ and CO₂ act together as compared to their individual contribution [117,118] 	<ul style="list-style-type: none"> See above

246

3.1. Electrochemical, thermodynamic and kinetic aspects of corrosion

247

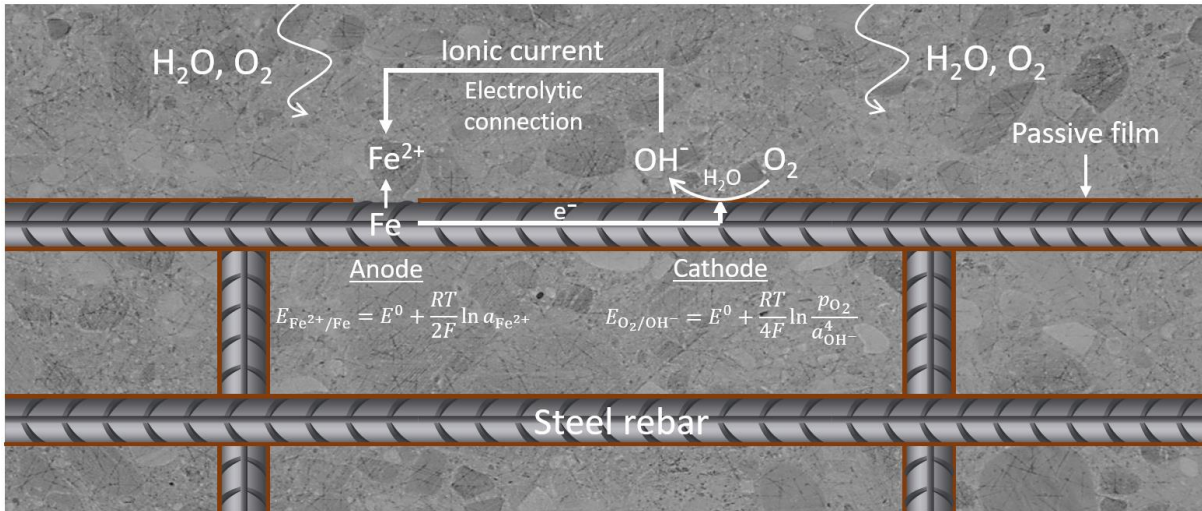
The corrosion of steel in concrete is an electrochemical process that involves the anodic dissolution of iron and, generally, the cathodic reduction of oxygen [119,120]. Depending on the availability of oxygen and the pH near the steel surface, it is also possible to observe the reduction of proton [121]. Finally, an electrical connection between the anode and the cathode is required for transferring the electrons, and an electrolytic environment for transferring the ions in solution (Fig. 3).

248

249

250

251



252

253

Figure 3. Schematic representation of the corrosion of steel in concrete, involving iron oxidation, oxygen reduction, and the electrical connection and ionic current between the anodic and cathodic sites.

254

255

The general principle of steel corrosion in concrete can be explained with the stability diagram of the Fe/H₂O system (potential-pH or Pourbaix diagram) [122]. Depending upon the experimental conditions, i.e. total Fe content and temperature, the predominance of species can be quite different (Fig. 4). As shown in section 2.2, the thin (~10-15 nm) and passive film developed on the steel surface is preserved under alkaline conditions (passivation domain). If this passive layer remains intact, iron is in the passivation domain and corrosion is slow (less than 0.1 μA cm⁻², “passive rebar”). Unfortunately, the continuous degradation of reinforced concrete in environments containing CO₂ and Cl⁻ affects the integrity of the passive layer. Iron changes to the corrosion domain, which results in the acceleration of corrosion (higher than 1 μA cm⁻², “actively corroding rebar”) and the progressive loss of steel cross section associated with the formation of corrosion products.

256

257

258

259

260

261

262

263

264

265

The electrochemical kinetics of corrosion are given by the Butler-Volmer equation (Eq. 1) [123]:

$$i = i_0 \left\{ \exp \left[\frac{\alpha_a n F}{RT} (E - E_{\text{corr}}) \right] - \exp \left[- \frac{\alpha_c n F}{RT} (E - E_{\text{corr}}) \right] \right\} \quad (\text{Eq. 1})$$

266

where i is the current density (A m⁻²), i_0 is the exchange current density or corrosion current density i_{corr} (A m⁻²), α_a and α_c are the anodic and cathodic charge transfer coefficient, respectively, n is the number of electrons exchanged in the reaction, F is the Faraday constant (96485 C mol⁻¹), R is the universal gas constant (8.314 J mol⁻¹ K⁻¹), T is the absolute temperature (K), E is the electrode potential (V) and E_{corr} is the corrosion potential (V). The term $\frac{\alpha n F}{RT}$ is equivalent to the term $\frac{\ln(10)}{\beta}$, where β is the

267

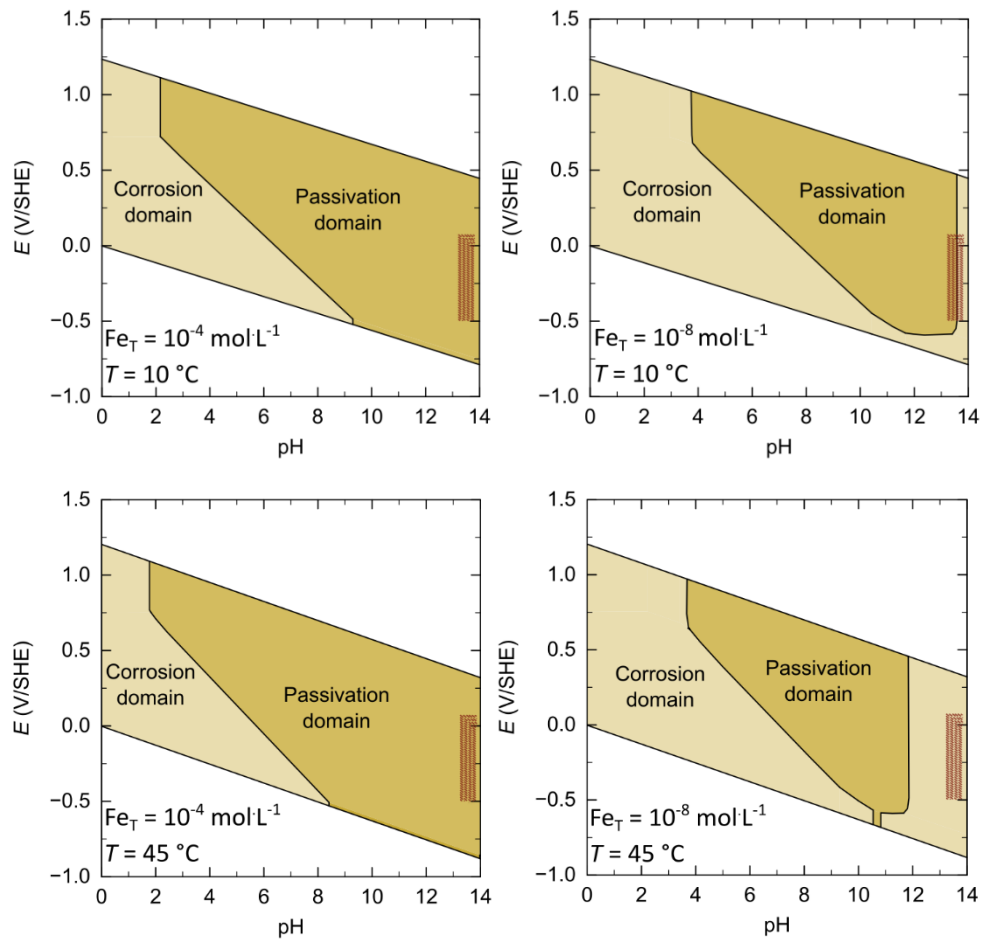
268

269

270

271 Tafel slope (special case of the Butler-Volmer equation, see section 4.3). As it will be developed in the
272 following sections, the corrosion rate depends upon:

- 273 • the water content [124,125]. When RH increases to ~70%, the adsorption of water vapour
274 occurs on external surfaces of C-S-H [38], and the resulting water film is thin and can be
275 considered electrically inactive (high resistance to ionic transport). The further increase in RH
276 from ~70 to ~95% enables the adsorption of multilayer water molecules and the filling up of
277 mesopores [38], decreasing the resistance to ionic transport in concrete;
- 278 • the temperature, which affects the kinetic parameters of the corrosion process, such as Tafel
279 slopes, exchange current density and equilibrium potential [126,127];
- 280 • the pore size distribution [124,125] and the presence of interfacial voids [128];
- 281 • the transport properties of aggressive agents in concrete, notably their diffusion coefficients
282 [129,130], and the availability of dissolved oxygen in the cathodic areas, i.e. presence of a
283 cathodic limited current or not [131];
- 284 • the transport of Fe^{2+} and the nature and distribution of precipitated corrosion products [132].



285

286

287 **Figure 4.** Simplified stability diagrams of the Fe/H₂O system indicating the corrosion domain (dissolved iron
288 species) and the passivation domain (precipitated iron species) in the domain of water stability for two total iron
289 content and two temperatures. The hatched area represents the pH and potential range generally reported for
290 carbon steel in sound OPC concrete. These predominance diagrams were obtained with PhreePlot software and
291 the Thermodem database [133]. Fe-bearing phases considered for calculation were Fe(OH)₂, magnetite (am),
292 ferrihydrite (6L), goethite and lepidocrocite, which are the main corrosion products of steel in concrete.

293

3.2. Carbonation-induced corrosion

294

3.2.1. CO₂ penetration and concrete carbonation

295 Atmospheric carbon dioxide ($p\text{CO}_2 \approx 0.04\%$) can penetrate into cement-based material mainly by
296 absorption into interconnected capillary pores on the concrete surface and by diffusion in depth
297 through the pore network and microcracks [134]. CO_2 diffusion coefficient increases when increasing
298 the water-to-cement ratio as the total porosity of the cement paste increases. The rate of CO_2
299 penetration is highest at low RH, when the pores are mostly air-filled [135–137]. The presence of salt
300 in concrete also contributes to block the ingress of CO_2 due to pore clogging [138]. During its ingress,
301 CO_2 dissolves in the pore water and forms carbonic acid H_2CO_3 . According to the speciation of CO_2
302 [139], carbonic acid dissociates in HCO_3^- and CO_3^{2-} depending on the pH of the pore solution.

303 Carbonation of concrete is the reaction between CO_2 and Ca-bearing hydrated phases, e.g. portlandite,
304 C-S-H and ettringite. The reaction kinetics appear governed by the exposure conditions [134,140]. All
305 reactions with hydrated phases occur in solution and are therefore more important and more rapid in
306 saturated concrete. However, as the rate of CO_2 penetration is highest at low RH, it is often reported
307 that the carbonation rate is highest in the 50-70% RH range [135,141]. Environmental exposure affects
308 the rate of carbonation; for example, the more rainy days, the lower the carbonation rate [142]. This
309 rate depends also on concrete porosity, and thus on the w/c ratio. A low w/c ratio and a high
310 compressive strength are required to limit as much as possible the carbonation depth, especially in
311 severe environmental conditions [138,143,144]. It is also dependent on the temperature, the CO_2
312 partial pressure, the alkaline reserve in the concrete (CO_2 binding capacity), and the presence of cracks
313 [134,145,146]. All these parameters are required for an accurate modelling of carbonation processes
314 in RC structures [147–150].

315 Carbonation induces changes in mechanical properties and microstructure of cement-based materials
316 [134,151,152]. It results notably in the formation of calcium carbonates CaCO_3 , calcite being the most
317 stable phase [134]. For OPC concrete, its precipitation results in a lower permeability through total
318 porosity reduction [153] and loss of interconnectivity due to pore clogging as CaCO_3 occupies a larger
319 volume than $\text{Ca}(\text{OH})_2$ [154]. However, as the capillary porosity increases [155], the ionic migration
320 through the cement paste can be increased because of carbonation. But as shrinkage and cracking of
321 the concrete can occur in parallel, it is difficult to predict the change only due to carbonation [134].

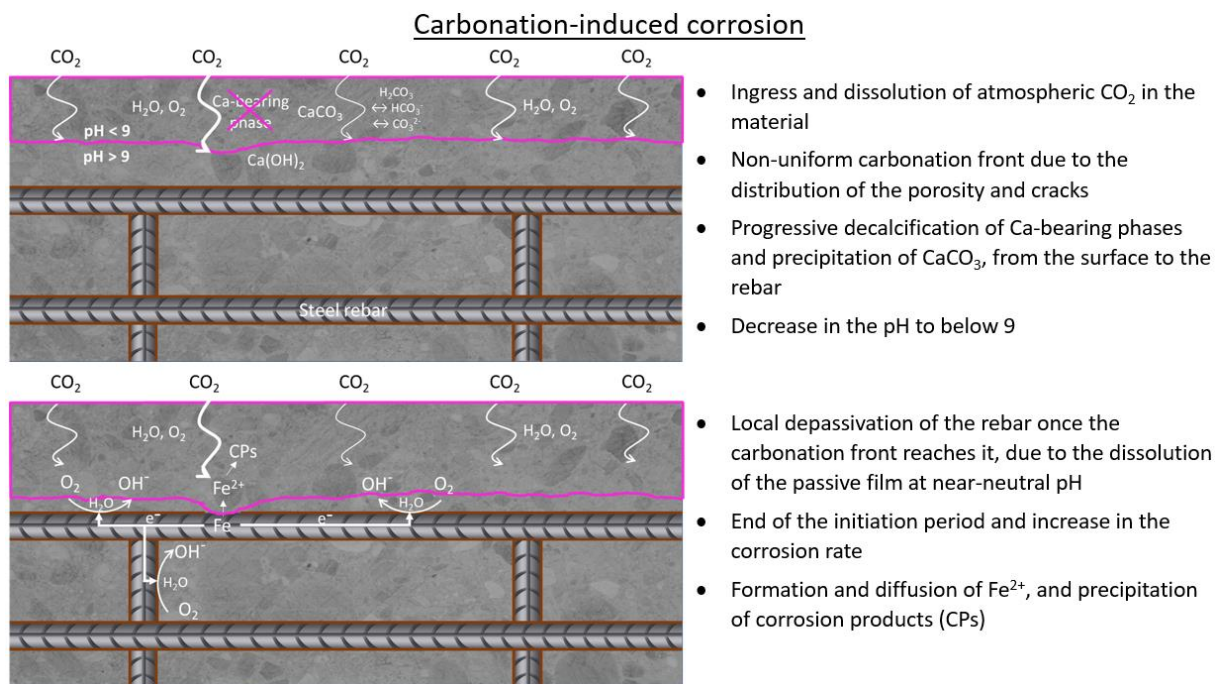
322 As the carbonation of concrete exposed to atmospheric conditions is a slow process, especially for OPC
323 concrete (a few tens of millimetres in 20 years [156]), accelerated laboratory tests are generally
324 performed in an CO_2 -rich atmosphere under conditions where the rate of carbonation is maximum
325 ($\approx 50\text{-}70\%$ RH). As shown by several authors, these accelerated tests are representative of the natural
326 carbonation in terms of changes in mineralogy, microstructure, water retention and cracking as long
327 as the CO_2 content is low ($p\text{CO}_2 < 3\text{-}4\%$), even if carbonation is only partial and the formation of
328 metastable CaCO_3 phases, i.e. aragonite and vaterite, is promoted instead of calcite [157,158].

329

3.2.2. Depassivation and corrosion mechanisms

330 Despite possible self-healing of concrete, carbonation is responsible for a decrease in pH of the pore
331 solution from above 13 to below 9, which results in dissolution of the passive layer of the rebar when
332 the carbonation front reaches its surface [150,159]. According to the Pourbaix diagram (Fig. 4), the

333 process will progressively change from the passivation domain to that of corrosion [160,161]. It is
 334 commonly assumed that the corrosion induced by carbonation is generalized and relatively
 335 homogeneous [92]. Considering this case, steel is uniformly depassivated, and the anodic and cathodic
 336 areas are located at adjacent locations. The term ‘microcell corrosion’ is used for describing this
 337 situation [162]. However, because of the heterogeneous structure of concrete (cracks, pore size
 338 distribution and interconnectivity), the carbonation front is seldom perfectly uniform on RC structures,
 339 and a spatial variability in the carbonation depth near the rebar can be observed [163]. The local
 340 variation in indoor and outdoor exposure is also responsible for the steepness of the reaction front
 341 [164]. This non-uniformity will create different steel-concrete interface along the same rebar, allowing
 342 the formation of ‘macrocell corrosion’ [156]. In addition, the presence of load-induced cracks will affect
 343 the steel-concrete interface independently of the crack-opening size, promoting local carbonation and
 344 damage of the interface [165]. In structures where steel rebars with different conditions are
 345 interconnected, macrocell corrosion is thus expected to be the main corrosion process [162,166]. It is,
 346 however, still important to consider both microcell and macrocell components, as the neglect of one
 347 of these components may result in underestimating the degree of corrosion [167–169]. A schematic
 348 representation of the supposed mechanism of carbonation-induced corrosion is shown in Fig. 5.



349
 350 **Figure 5.** Schematic representation of the mechanism of carbonation-induced corrosion of steel in concrete
 351 according to the literature cited in the text.

352 The evolution of the corrosion rate in carbonated concrete is still not fully understood. For each
 353 concrete composition, it is highly dependent upon water content and pore size distribution [170].
 354 Different degree of saturation and porosity could thus explain the different corrosion rates observed
 355 in carbonated concrete. Some authors reported that the corrosion rate increases up to 90-95% RH
 356 before decreasing due to a limitation of the oxygen availability at high RH, indicating the presence of
 357 a cathodic limited current [104,129,171]. However, other authors reported that the corrosion rate
 358 increases continuously up to 99% RH [124,125,170]. Even at high RH, the material is hardly fully water-
 359 saturated as saturation cannot happen only by capillary condensation or capillary suction in large pores
 360 (the size being dependent on the pore geometry). This suggests that cathodic control of the corrosion

361 rate due to a limited availability of O_2 is relevant only under long-term immersion, i.e. when all gaseous
362 and dissolved O_2 is depleted in concrete [124]. This confirms that the two main influencing factors of
363 the corrosion rate of steel in atmospherically exposed RC structures are the water content and the
364 pore structure [125]. Consequently, corrosion is under activation control: the corrosion rate increases
365 during wetting exposure until the electrochemically active surface is water-filled, and then decreases
366 during drying exposure [172]. This mechanism controlling the corrosion rate has been proposed for
367 uniformly depassivated rebars in very thin samples. Further studies are required to confirm the validity
368 of the kinetics of iron corrosion for larger cover depth and when the macrocell component is also
369 considered, as non-uniform corrosion is expected on real structures.

370 *3.3. Chloride-induced corrosion*

371 *3.3.1. Chloride penetration*

372 The presence of chloride in the concrete can result from chloride-contaminated components of
373 aggregates or contaminated construction water, or by diffusion from the environment, e.g. exposure
374 to a marine environment (e.g. XS microenvironment with wetting/drying cycles) or the use of de-icing
375 salts (i.e. $CaCl_2$, $MgCl_2$, $NaCl$) in winter [7]. The penetration of chloride occurs mainly through capillary
376 pores as free chlorides Cl^- by capillary suction, diffusion and permeation [7]. Thus, the initiation time
377 of corrosion strongly depends upon transport parameters, such as the diffusion coefficient of total
378 chloride in concrete [173].

379 It is, however, difficult to predict correctly this parameter as it may be influenced by many others. First,
380 the diffusion is affected by pore size distribution and pore interconnectivity in the concrete, which is
381 related to the w/c ratio. It is recommended to use a low w/c ratio (0.4-0.5) for increasing the length of
382 the initiation stage, as the total porosity will be decreased [174]. Second, a part of the free chlorides
383 can be physically adsorbed on different hydrates such as C-S-H and monosulfoaluminates (AFm), or
384 can chemically react with other phases such as tri-calcium aluminate (C_3A) to form Friedel's salt when
385 the chloride content is sufficient [175,176]. Physical adsorption depends mainly on the specific surface
386 area of the cement paste, while chemical adsorption through formation of Friedel's salt is mainly
387 related to the monocarboaluminate content in the paste [177]. SCMs with high alumina and calcium
388 content can also play a role in the chloride binding capacity, and thus on the durability of RC, by limiting
389 Cl^- ingress to the rebar [177]. Finally, diffusion of Cl^- is affected by water content, temperature, and the
390 properties of the electrical double layer [176,178,179]. The diffusion coefficient varies also in the ITZs
391 of concrete as a function of their volume and tortuosity [180]. As for CO_2 and other aggressive species,
392 the presence of cracks in the concrete or the presence of defects at the steel-concrete interface may
393 provide further preferential paths for the ingress of chloride to the steel surface [181–184].
394 Irrespective of the factors affecting chloride penetration, determining the rate of Cl^- ingress is required
395 for modelling the service life of the initiation stage of corrosion [185–187].

396 For accelerating the rate of Cl^- ingress and thus to initiate more rapidly chloride-induced corrosion,
397 several procedures were investigated, e.g. mixing chloride salt in the cement paste or the
398 electromigration/rapid chloride permeability test (RCPT). However, the results obtained by mixing
399 chloride salt directly in the cement paste can only be used for determining the effect of contaminated
400 aggregates or water, as the passive film will not form properly on the rebar [168] and the hydration
401 products will be different, affecting the microstructure of the concrete [65]. RCPT can also affect the

402 concrete microstructure [188] and thus cracks formation. Thus, the results obtained from accelerated
403 tests must be used with care if they aim at understanding corrosion mechanisms.

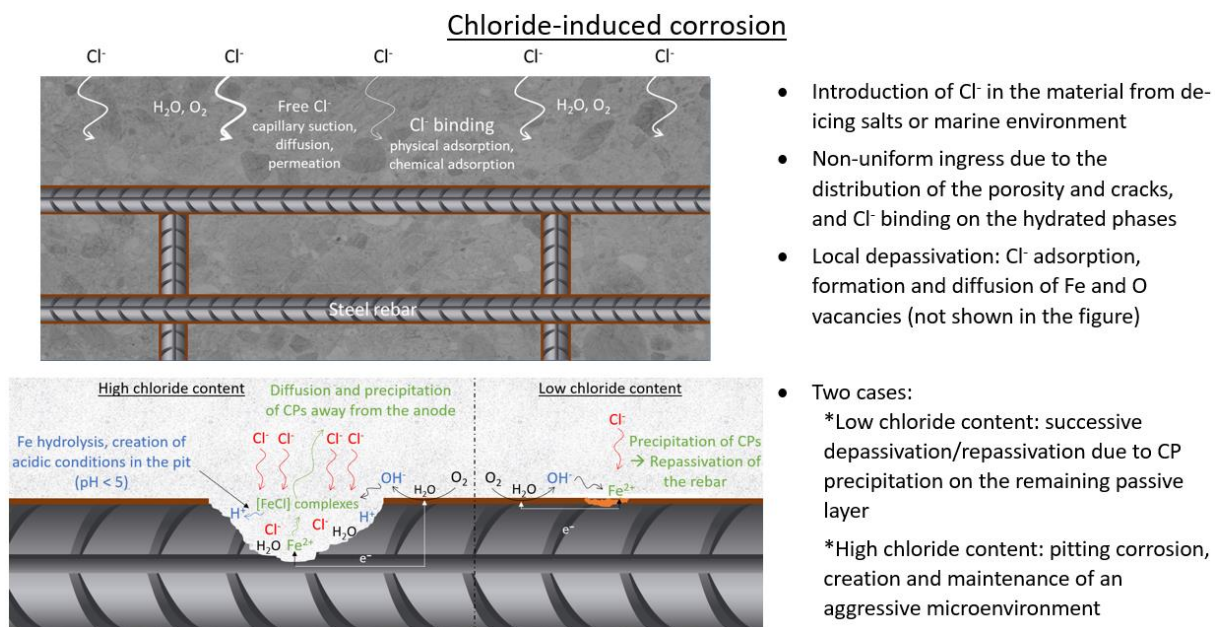
404 *3.3.2. Depassivation and corrosion mechanisms*

405 As for carbonation-induced corrosion, there still is a lack in the physical understanding of the
406 depassivation mechanism of steel exposed to chloride ions [92,187]. Two models are generally
407 proposed: the ion exchange model [189] and the point defect model [190]. In the first one,
408 depassivation is the result of the adsorption and ingress of Cl^- through the outer film layer and the
409 progressive thinning of the inner film until dissolution. In the second one, chloride ions remain
410 adsorbed on the film surface and act as a catalyst in the formation of Fe vacancies on the
411 oxide/electrolyte interface, which then diffuse to the oxide/metal interface while O vacancies diffuse
412 in the opposite direction. The combination of Fe vacancies results in the formation of voids and thus
413 in depassivation of the rebar. It appears that the lattice structure of this film and the presence of
414 defects strongly affect the depassivation mechanism [191]. Recent experiments of steel corrosion in
415 simulated concrete pore solutions have shown the modification of the structure and electronic
416 properties of the passive film exposed to chloride. Notably, an increase in the $\text{Fe}^{3+}/\text{Fe}^{2+}$ ratio was
417 observed in association with a decrease in film thickness [91,93,192–194]. The donor density N_D of the
418 passive film increases in the presence of chloride, resulting in a higher electric conductivity and thus
419 lower corrosion resistance of the film, suggesting the incorporation of chloride ions in the passive film
420 [195]. However, molecular dynamics and density functional theory simulations support the point
421 defect model, as no ingress of chloride has been observed in any simulation [196,197].

422 It is often reported that a minimum chloride content is required for observing the depassivation of
423 steel, so-called the critical chloride content or the chloride threshold value C_{crit} . It is expressed either
424 as the total chloride content relative to binder weight [198], or as the chloride ion activity relative to
425 the pH of the pore solution [199]. Even if only free chlorides are suspected to cause steel corrosion
426 [200], chlorides bounded onto solid phases represent a potential reservoir of free chlorides for
427 corrosion [198]. This is notably observed in the case of the carbonation of chloride-contaminated
428 concrete as carbonation decreases the chloride-binding capacity of hydrates [116,201]. C_{crit} ranges
429 from 0.04 to 8.34% by binder weight, or from 0.01 to 45 in terms of $[\text{Cl}^-]/[\text{OH}^-]$ molar ratio [199]. It
430 depends on many parameters such as RH, temperature, the pH of the pore solution, local
431 characteristics at the steel-concrete interface and the exposed area of rebar [64,77,202–208]. Though
432 the concept of the chloride threshold value is well accepted, it does not allow an accurate estimation
433 of service life in all cases, even with complex transport models [187,209]. In addition, C_{crit} values
434 obtained from small-scale laboratory samples are hardly applicable to real structures as the
435 preparation conditions are not as well controlled in the field [210] and local inhomogeneities at the
436 steel-concrete interface create a size effect [211]. A test method for mimicking realistic conditions in
437 laboratory specimens is still required [65]. If the weakest-link theory is a suitable option to consider
438 the size effect of corrosion [211], a more practical solution consists in measuring C_{crit} value on samples
439 taken from existing structures. This overcomes the limited applicability of laboratory data and provides
440 case-specific input data to improve the prediction of the service life of the investigated structure [187].

441 Once the passive film is locally disrupted, anodic dissolution occurs if the water content and oxygen
442 availability are sufficient for the cathodic reduction [212,213]. Due to the localized presence of chloride
443 in the concrete, iron dissolution generates small pits though the surrounding steel surface still retains

444 its passive film. Chloride ions are attracted to the metal dissolution sites for maintaining
 445 electroneutrality [214], resulting in the enhancement of iron solubility in the pit due to the formation
 446 of iron chlorocomplexes and chloride green rust GR(Cl⁻) [215]. Pit stability depends upon the
 447 competitive migration between Cl⁻ and OH⁻, which depends on the mobility and concentration of both
 448 ions. In the case of insufficient Cl⁻, a depassivation/repassivation sequence is expected to occur due to
 449 the precipitation of iron(II) hydroxide inside the pit [216]. A sufficient [Cl⁻]/[OH⁻] ratio is thus needed
 450 for achieving stable pit growth. After iron dissolution, the hydrolysis of ferrous iron ions creates local
 451 acidification in the pit [217,218] and iron chloride ions Fe(H₂O)_(n-m)Cl_m^{(z-m)+} will diffuse outside the pit
 452 where they will be dissociated being no longer stable under higher pH conditions. Due to the presence
 453 of well-defined anodic and cathodic areas, chloride will migrate back to the anode for further chloride
 454 attack, while ferrous iron ions will migrate to the cathode in an oxygen-rich region, where it will
 455 precipitate. As a result, an aggressive microenvironment is preserved in the pit, and an autocatalytic
 456 process explains the corrosion process in chloride-contaminated concrete. A schematic representation
 457 of the supposed mechanism of chloride-induced corrosion of steel is shown in Fig. 6.



458

459 **Figure 6.** Schematic representation of the mechanism of chloride-induced corrosion of steel in concrete
 460 according to the literature cited in the text.

461 Macrocells with very high corrosion rates are expected in chloride-induced corrosion [219], resulting
 462 in important local thinning of steel depending on concrete resistivity [216], driving voltage and
 463 cathode-to anode ratio [216]. The growth of anodic sites is more rapid close to the anode/cathode
 464 boundary than deeper down in the centre of the pit, due to the non-uniform distribution of current
 465 densities [123]. Hence, the extension of the pit is greater across the surface than in depth and the ratio
 466 between maximum and average corrosion depth, also called the “pitting factor”, ranges between 2.5
 467 and 10 [220,221]. Corrosion should thus be measured over the entire defective area to predict
 468 accurately the mechanical behaviour of a corroded structure [222].

469 In marine environments, in which RC structures are partially immersed, the cathode-anode distance is
 470 an important parameter in the corrosion process. Indeed, it has been shown that the macrocell
 471 corrosion current can be provided by a cathode located at large distances from the anode [223,224].
 472 Experiments and numerical simulations have shown that a non-negligible current can be provided by

473 cathodes located in unsaturated zones up to several meters away from the anodic area, depending on
 474 the geometry of the structure and its resistivity, which was here considered uniform [224]. Hence,
 475 even if O₂ is depleted near the anodic areas, the cathodic reaction may not be the rate-determining
 476 step of corrosion as it can occur far away from them. Nonetheless, resistivity differs in immersed zones
 477 compared to tidal and unsaturated zones [225], affecting the distribution of the current between
 478 anodic and cathodic areas. Further studies are thus required to gain more insights on this macrocell
 479 current by considering representative gradients of concrete resistivity in marine environment.

480 **3.4. Nature and reactivity of corrosion products and their impact on durability of the material**

481 Different corrosion products (CPs) are observed in RC structures. Table 2 lists possible CPs in concrete
 482 with their volume expansion [5,214,226,227].

483 **Table 2.** List of possible iron corrosion products in concrete with their volume expansion (NC=unknown).

Corrosion products	Formula	Valence	Volume expansion
Iron(II) hydroxide	Fe(OH) ₂	Fe(II)	3.7
Chukanovite	Fe ₂ (OH) ₂ CO ₃		NC
Siderite	FeCO ₃		NC
Ferrous hydroxychloride	β-Fe ₂ (OH) ₃ Cl		NC
Chloride green rust	Fe ^{II} ₃ Fe ^{III} (OH) ₈ Cl, 2 H ₂ O	Fe(II-III)	NC
Carbonate green rust	Fe ^{II} ₄ Fe ^{III} ₂ (OH) ₁₂ CO ₃ , 2 H ₂ O		NC
Sulphate green rust	Fe ^{II} ₄ Fe ^{III} ₂ (OH) ₁₂ SO ₄ , 8 H ₂ O		NC
Magnetite	Fe ₃ O ₄		2.1
Hematite	α-Fe ₂ O ₃	Fe(III)	2.1
Maghemite	γ-Fe ₂ O ₃		2.4
Iron(III) hydroxide	Fe(OH) ₃		4.2
Ferrihydrite	Fe ₂ O ₃ , 3 H ₂ O		6.5
Goethite	α-FeOOH		3.0
Akaganeite	β-FeOOH (β-FeO _{1-x} (OH) _{1+x} Cl _x)		3.5
Lepidocrocite	γ-FeOOH		3.2
Feroxyhyte	δ-FeOOH		2.8

484 Iron dissolution results first in the production of ferrous iron Fe²⁺ in solution. Then, iron(II) hydroxide
 485 Fe(OH)₂ is assumed to be the main precursor of precipitated CPs [218]. If several intermediates can
 486 then be formed, they are rapidly oxidized in the presence of oxygen. With a low oxygen supply, partial
 487 oxidation is common, resulting in the formation of magnetite Fe₃O₄. With a high oxygen supply,
 488 complete oxidation results in the formation of Fe(III) oxides and oxyhydroxides, collectively referred
 489 to as “rust”. The occurrence of CPs depends mainly on the nature of the rebar and the environmental
 490 parameters.

491 The presence of the rust layer is of great importance as it is directly implied in the mechanism of steel
 492 corrosion. It acts as a porous electrode where oxygen reduction can occur [228]. Notably, the exchange
 493 current density of O₂ reduction is higher where rust is present as compared to a surface where only
 494 mill scale occurs [229]. The reduction of rust, notably FeOOH, can also be seen as the cathodic reaction
 495 related to iron dissolution [230,231]. Due to the difference in electric conductivity and morphology of

496 the different CPs, determining their local distribution is important as it can influence the rate-
497 determining step of corrosion [232].

498 *3.4.1. Nature and distribution of CPs in carbonation-induced corrosion*

499 In carbonated media, chukanovite $\text{Fe}_2(\text{OH})_2\text{CO}_3$, siderite FeCO_3 and carbonate green rust $\text{GR}(\text{CO}_3^{2-})$ are
500 expected to form as intermediates, and the oxidation of chukanovite results in the formation of
501 lepidocrocite and goethite [233]. Feroxyhyte can also be observed in addition to these two products
502 [234]. Because of the very low solubility of iron oxyhydroxides at near-neutral conditions in carbonated
503 concrete, they tend to precipitate in the porosity at the vicinity of the rebar to form a 'corrosion layer'
504 [218]. The accumulation of precipitates under confined conditions will cause an expansive pressure,
505 resulting in cracks formation in concrete.

506 The transport of Fe^{2+} away from the rebar must thus be considered for the evolution of the corrosion
507 rate and the formation of corrosion-induced cracks. It depends on (i) Fe^{2+} content and (ii) concrete
508 porosity. Indeed, precipitation will occur only after Fe^{2+} saturation in the solution is reached. If the
509 corrosion rate is slow, which is the case of natural corrosion in carbonated concrete, no saturation of
510 Fe^{2+} ions is expected close to the steel surface, resulting in their diffusion away from the interface
511 [132]. According to Nernst equation, increasing Fe^{2+} content in the vicinity of the rebar increases the
512 anodic reversible potential, resulting in a decrease of the corrosion rate. Hence, an increase in total
513 porosity of concrete will facilitate the diffusion of Fe^{2+} away from the rebar, resulting in a decrease of
514 the anodic reversible potential and in the increase of the effective corrosion current density [125].

515 Nonetheless, a maximum effective current density is expected beyond a certain opening of the pore
516 structure, from which the system tends to behave as a bulk solution in terms of transport properties
517 (no more transport limitation due to concrete porosity) [125]. The diffusion of Fe^{2+} away from the rebar
518 competes with the diffusion of O_2 in the opposite direction. Hence, the diffusion of Fe^{2+} can be very
519 limited, depending on the pH, as it is oxidized in Fe^{3+} and precipitates rapidly as $\text{Fe}(\text{III})$ -bearing species,
520 Fe^{3+} being much less soluble than Fe^{2+} . We must note that even if a thick corrosion layer develops at
521 the vicinity of the rebar, a "virtual" diffusion of Fe^{2+} can still occur across this layer through electron
522 transfer in the $\text{Fe}(\text{III})$ layer, i.e. sorption of one Fe^{2+} on one side and release of another Fe^{2+} on the
523 other side, as proposed for Fe diffusion at the steel-bentonite interface [235].

524 *3.4.2. Nature and distribution of CPs in chloride-induced corrosion*

525 For chloride-induced corrosion, several intermediates can be formed, such as ferrous hydroxychloride
526 or chloride green rust $\text{GR}(\text{Cl}^-)$, which is thermodynamically stable in the alkaline pore solution and can
527 be observed near the rebar [215,236]. A large variance in the final CPs is reported in the literature, the
528 products being a mixture of magnetite, goethite, lepidocrocite and/or ferrihydrite [237–239]. In
529 addition, in the presence of a large excess of chloride, ferrous hydroxychloride $\beta\text{-Fe}_2(\text{OH})_3\text{Cl}$ is
530 suspected to be formed as an intermediate product before its oxidation in $\text{GR}(\text{Cl}^-)$, which can be later
531 oxidized into akaganeite with an increased chloride content [240,241]. Currently, there is no physical
532 explanation for this variance, probably because the mechanism of steel depassivation is still not fully
533 understood [92].

534 In addition to the local acidic conditions induced in the pit, the presence of chloride increases the
535 solubility of Fe^{2+} ions, which prevents their rapid precipitation and allows their diffusion and migration

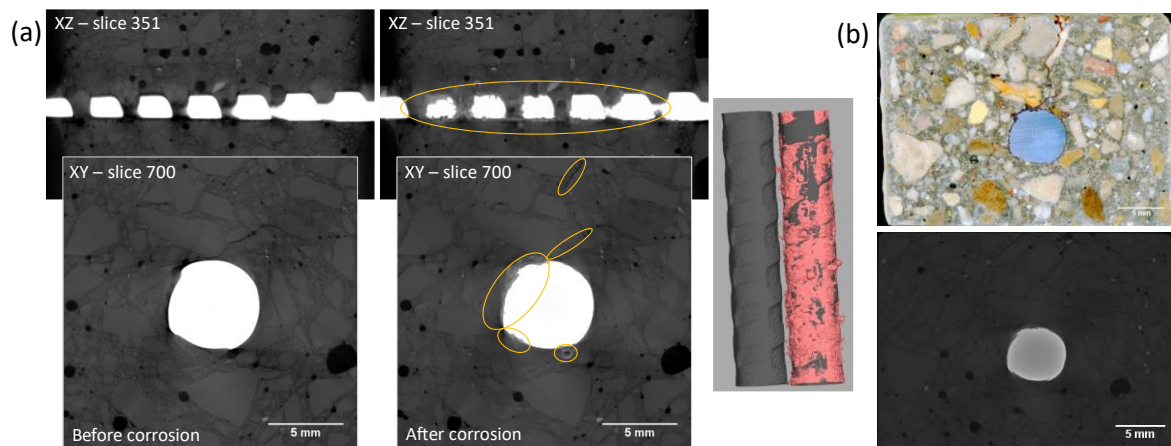
536 away from the pit [218]. CPs accumulate first between the steel and the mill scale and then penetrate
537 adjacent porous zones [242]. This penetration strongly depends upon the distribution of the hydration
538 products and the concrete porosity around the rebar. As they diffuse away from the pit, ferrous
539 chloride ions are no longer stable due to the higher pH of the pore solution and rapidly precipitate,
540 filling the pores ('corrosion-filled paste') [243] and impeding further diffusion of Fe^{2+} . As corrosion
541 continues, new CPs tend to precipitate near the surface of the rebar, which finally results in the
542 formation of corrosion-induced cracks [244]. Hence, major localized loss of steel cross-section may
543 occur before the appearance of cracks on concrete surface in the case of chloride-induced corrosion.

544 *3.4.3. Impact on the structural performance of RC structures*

545 The formation of solid-state CPs plays a major role in the structural performance and service life of RC
546 structures [92]. Even if it can be up to 6.5, as shown in Table 2, the expansion coefficient of the mixture
547 of CPs in concrete generally varies between 2 and 4 [245–247]. This volume expansion will exert a
548 radial pressure on concrete, generating corrosion-induced cracks if CPs grow under confined
549 conditions [239,248,249]. The cracking process can be split into three stages: corrosion products filling,
550 concrete cover stress and concrete cover cracking [250]. If the first stage progressively modifies the
551 porosity and can help in preventing corrosion if pore clogging occurs, the two other stages result in
552 accelerated corrosion as they create preferential paths for the ingress of aggressive agents. The time-
553 to-cracking of the concrete related to steel corrosion is thus largely dependent upon its porosity.

554 Moreover, environmental parameters such as temperature can accentuate the cracking process.
555 Indeed, the morphology of the oxide layer can change with temperature [251], and partially reversible
556 redox reactions have been observed during temperature cycling between 5 and 45 °C [252]. The
557 valence state of the shell and the hydroxide content (i.e. oxidation and hydration: transformation of
558 magnetite into goethite or lepidocrocite) is positively correlated with temperature increase, leading to
559 an augmentation in the corrosion potential of the rebar [253]. Thus, the corrosion potential is more
560 linked to redox activity of the oxide layer than to oxygen availability, as the concentration of oxygen
561 decreases with a temperature increase [252]. The opposite trend is observed when temperature
562 decreases (i.e. dehydration and reduction), resulting in a "breathing" of the shell with temperature
563 cycling that can affect the stability of the passive film [253].

564 The development of CPs and the possible formation of corrosion-induced cracks can be monitored
565 with scanning electron microscopy (SEM), energy dispersive X-ray spectrometry (EDS), X-ray diffraction
566 (XRD), Raman spectroscopy and X-ray μ CT (Fig. 7) [128,254–258]. Four different parts can be observed
567 in the material: the steel, the dense product layer, the transformed medium and the binder [259,260].
568 The mill scale can also be sometimes differentiated [261,262]. As the rust distribution is generally non-
569 uniform on the steel surface [263], several models have been developed for predicting corrosion-
570 induced concrete cracking [264–266]. Though the models adequately predict the time-to-cracking for
571 the experiments for which they were calibrated, their predictions may not be as accurate for fitting
572 the results obtained in other studies with different experimental conditions [267]. Hence, the
573 development of a general model for corrosion cracking is still required.



574
 575 **Figure 7.** (a) X-ray μ CT 2D slices acquired on a mortar sample like the one of Fig. 1, comparing the same sample
 576 before and after corrosion. The 2D slices are extracted from the 3D volume at the same position to visualize the
 577 development of corrosion products. The rebar is shown before and after corrosion by thresholding the corrosion
 578 products (in pink). X-ray μ CT images show that the corrosion products fill the porosity (air voids) and generate
 579 cracks on the mortar around the rebar up to its surface (surrounded in yellow). (b) Comparison of surfaces by
 580 optical and X-ray μ CT acquisition. After accelerated corrosion, the sample was cut to observe the distribution of
 581 corrosion products in the sample. Though X-ray μ CT is a great technique to determine the distribution of phase
 582 and porosity of the material, some corrosion products are hardly detected. Courtesy: S. Gaboreau.

583 **4. Electrical methods for non-destructive testing and evaluation of corrosion**

584 Non-destructive testing and evaluation (NDT) of the corrosion of steel in concrete is a major issue for
 585 predicting the service life of reinforced concrete structures [18]. Among the different techniques,
 586 electrical methods allow evaluating the corrosion rate, a parameter of prime importance for estimating
 587 the service life of RC structures in the propagation stage. These methods require the use of an electrical
 588 system with two-, three- or four-electrode configurations to determine three main parameters:
 589 corrosion potential E_{corr} , concrete resistivity ρ and polarization resistance R_p [268]. Table 3 summarizes
 590 the different techniques presented in detail in this section, with their methodology and main
 591 advantages and drawbacks.

592 **Table 3.** List of electrical methods for the assessment of the corrosion rate of steel in concrete, with their main advantages and drawbacks.

Method	Methodology	Advantages and drawbacks
Corrosion potential/ Half-cell potential	Measurement of the open-circuit potential difference between the rebar and a reference electrode placed on the concrete surface or embedded in the concrete	<ul style="list-style-type: none"> ✓ Fast measurement ✓ Allow the identification of the main defect points with high corrosion risk ✗ No quantitative information of the corrosion rate ✗ Absolute value is highly affected by concrete conditions (geometry, resistivity, presence of cracks), composition of the pore solution (pH, chloride or sulphide content), the condition of the steel rebar (cathode-to-anode ratio), the availability of oxygen near the steel surface and environmental factors (RH, T) <ul style="list-style-type: none"> ➔ Results must be interpreted only as potential gradients ✗ Electrical connection to the rebar is required <ul style="list-style-type: none"> ➔ Measurements can be performed using at least two reference electrodes placed on concrete surface and the results must be interpreted as potential vectors [269–271]
Concrete resistivity (Wenner configuration)	Injection of a direct or alternating current between the two outer electrodes and measurement of the resulting potential difference between the two inner electrodes Usual parameter: <ul style="list-style-type: none"> • $0.01 < f \text{ (kHz)} < 10$ 	<ul style="list-style-type: none"> ✓ Fast measurement ✓ Provide insights on concrete durability ✓ Allow the identification of the main defect points with high corrosion risk ✓ Corrosion rate can be estimated based on recommendations and correlations with concrete resistivity ✗ No unique correlation could be determined between the two parameters ✗ Absolute value is highly affected by concrete conditions (geometry, resistivity, presence of cracks), composition of the pore solution, environmental factors (RH, T), and the presence of the rebar <ul style="list-style-type: none"> ➔ Electrical resistivity tomography (ERT) must be performed to consider accurately the inherent heterogeneity of concrete and to account for the rebar effect in the measurement

Linear polarization resistance (LPR)	<p>Linear sweep voltammetry in the anodic or cathodic direction around the corrosion potential</p> <p>Usual parameters:</p> <ul style="list-style-type: none"> • Sweep rate = 10 mV min⁻¹ • $E_{\text{corr}} \pm 10\text{-}20$ mV 	<ul style="list-style-type: none"> ✓ Fast measurement ✓ Good agreement with gravimetric loss in case of active corrosion ✗ Electrical connection to the rebar is required ✗ Use of the Stern-Geary relation to convert R_p in corrosion current ✗ Concrete resistivity must be determined using another technique to compensate the ohmic drop ✗ Determining the polarized area on RC structures is challenging ✗ The corrosion rate in the case of passive corrosion is overestimated <ul style="list-style-type: none"> ➔ Slower sweep rate (<2.5 mV min⁻¹) must be used to improve the measurement of corrosion rate in this case
Tafel scan	<p>Methodology similar to LPR</p> <p>Usual parameters:</p> <ul style="list-style-type: none"> • Sweep rate = 10 mV min⁻¹ • $E_{\text{corr}} \pm 150\text{-}250$ mV 	<ul style="list-style-type: none"> ✓ Provide directly the corrosion current instead of R_p ✗ Electrical connection to the rebar is required ✗ Can cause irreversible changes to the rebar due to the strong polarization ✗ Determining the polarized area on RC structures is challenging
Galvanostatic pulse (GP)	<p>Injection of a direct current between the rebar and a counter electrode during, and measurement of the resulting potential difference between the rebar and a reference electrode</p> <p>Usual parameters:</p> <ul style="list-style-type: none"> • $I = 5\text{-}500$ μA ($\Delta E < 20$ mV) • $t = 5\text{-}30$ s 	<ul style="list-style-type: none"> ✓ Fast measurement in general ✓ Good agreement with gravimetric loss in case of active corrosion ✗ Electrical connection to the rebar is required ✗ Use of the Stern-Geary relation to convert R_p in corrosion current ✗ Determining the polarized area on RC structures is challenging ✗ The corrosion rate in the case of passive corrosion is overestimated <ul style="list-style-type: none"> ➔ Longer measurement time (>100 s) must be used to improve the measurement of corrosion rate in this case
Electrochemical impedance spectroscopy (EIS)	<p>Injection of an alternating potential between the rebar and a counter electrode during, and measurement of the resulting current between the rebar and a reference electrode</p> <p>Usual parameters:</p> <ul style="list-style-type: none"> • $E = 10$ mV RMS 	<ul style="list-style-type: none"> ✓ Good agreement with gravimetric loss in case of active and passive corrosion ✓ Provide insights on the corrosion mechanism ✗ Electrical connection to the rebar is required ✗ Selection of the electrical equivalent circuit is of prime importance to determine accurately R_p ✗ Use of the Stern-Geary relation to convert R_p in corrosion current ✗ Measurement time is long

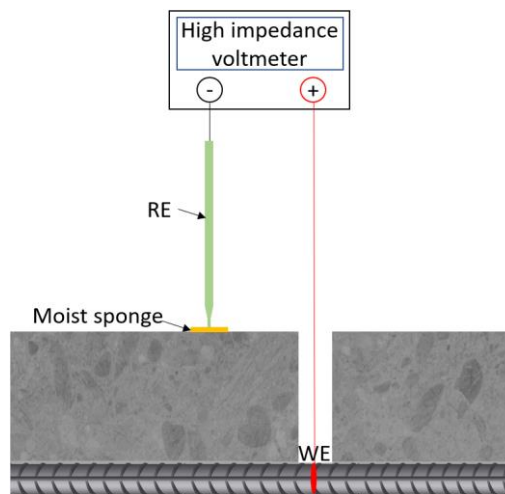
	<ul style="list-style-type: none"> • $10^{-3} < f \text{ (Hz)} < 10^5$ 	<ul style="list-style-type: none"> ➔ Possibility to limit the use of low frequencies but the accuracy of the R_p value obtained in this case may be less accurate, irrespective of the selected EEC ➔ Alternatively, harmonic analysis of the signal obtained at only one low frequency in the time-domain can be done to obtain the corrosion current ✗ Determining the polarized area on RC structures is challenging
Indirect GP	Methodology similar to GP, but using a four-electrode configuration placed on the concrete surface, where two probes are used to inject the direct current and two probes are used to measure the resulting potential difference	<ul style="list-style-type: none"> ✓ Fast measurement in general ✓ Good agreement with gravimetric loss in case of active corrosion and passive corrosion for highly resistive concrete ✓ No electrical connection to the rebar is required ✓ 'Self-confinement' of the current to determine the polarized area ✗ Simulations are required to determine the current distribution in the material ✗ Studies are still required to quantify accurately the corrosion rate
Indirect EIS	Methodology similar to EIS, but using a four-electrode configuration placed on the concrete surface, where two probes are used to inject the alternating current and two probes are used to measure the resulting potential difference	<ul style="list-style-type: none"> ✓ Method sensitive to non-uniform corrosion that can separate the contribution of actively corroding areas and passive areas ✓ No electrical connection to the rebar is required ✗ Measurement time is long ✗ Studies are still required to provide quantitative information on the corrosion rate

594 **4.1. Corrosion potential**

595 Corrosion potential E_{corr} , also referred to as half-cell potential, is the open circuit potential (OCP) of the
596 rebar.

597 **4.1.1. Measurement**

598 The measurement is done with a two-electrode configuration, connecting the rebar—the first half of
599 the cell—and a reference electrode (RE)—the other half of the cell—through a high-impedance
600 voltmeter (Fig. 8) [272]. The method was first referenced as the ASTM C876 standard test method for
601 half-cell potentials of uncoated reinforcing steel in concrete. A local breakout of the concrete cover is
602 generally required to create a sound contact as the rebar is not readily accessible [273]. The reference
603 electrode is a silver-chloride electrode, a copper-sulphate electrode (CSE), or a saturated-calomel
604 electrode (SCE), which are mostly commercialized as liquid- or gel-filled electrodes. This kind of RE is
605 placed on the concrete surface, requiring a good electrolytic contact with the concrete. This is generally
606 ensured using a sponge wetted with an appropriate solution with a similar pH than that of the pore
607 solution to reduce as much as possible junction potentials [274]. As the position of the electrode and
608 the type of electrolytic contact both affect the OCP measurements, this information must be reported
609 in all studies.



610
611 **Figure 8.** Schematic diagram of the measuring system of corrosion potential using a surface reference electrode.

612 Alternatively, concrete-embeddable solid-state metal/metal oxide reference electrodes such as
613 manganese oxide MnO_2 , activated-carbon and graphite electrodes or pseudo-reference electrodes
614 with graphene-cement composites have shown a good stability in concrete for several months or years
615 [275–278]. Silver-based screen-printed electrodes provide another cost-effective sensing system
616 [279]. This is particularly interesting for new structures as the electrodes can directly be embedded
617 during their construction, and for existing structures after maintenance actions [280]. As the pore
618 solution ensures the electrolytic contact with embeddable electrodes, the contact resistance is less
619 problematic and the liquid junction potential is expected to be more constant over time, which can
620 then improve the quality of the data. However, the system is less flexible as the electrodes are fixed.

621 As the inspection of RC structures can be challenging, recent advances have indicated the feasibility of
622 using climbing robots/flying drones for the monitoring of the corrosion potential [281]. The advantages

623 of this approach are to guarantee the operator safety, especially in locations hardly accessible, and
624 potentially to decrease the global cost of inspection.

625 *4.1.2. Interpretation of results and recommendations*

626 As corrosion is non-uniform along the rebar, differences in electrochemical and streaming potential
627 values are expected between actively corroding and passive areas. The distribution of the
628 equipotential lines in the material will be affected by the electric current flowing between these areas.
629 Hence, the use of the half-cell potential technique requires the definition of a grid of measurements
630 on the structure. The measured values can widely range in the water stability domain. Irrespective of
631 the reference electrode used, they should be reported *versus* the standard hydrogen electrode (SHE)
632 at the measurement temperature. The results can be presented as table, map or in statistical
633 representations, depending on the size of the element and the number of data acquired [282].

634 The first version of the ASTM C876 standard recommended to interpret the corrosion potential based
635 on the absolute values for evaluating the probability of corrosion in the measured area [283]. For
636 values over -200 mV/CSE (≈ 116 mV/SHE), the probability of steel corrosion activity is less than 10%.
637 For values below -350 mV/CSE (≈ -34 mV/SHE), the probability of steel corrosion activity is over 90%;
638 in between the probability of such activity remains uncertain.

639 For a better insight into areas with a high corrosion risk, the RILEM recommendations (2003) [282] and
640 the revised ASTM C876 standard (2009) [283] advise the use of potential gradients rather than absolute
641 potential values. The proposed methodology consists of mapping the potential of the entire area of
642 inspection and comparing the relative potential values. This requires the definition of an accurate grid
643 of measurements points, as a decrease in grid space increases the probability of finding the precise
644 location of actively corroding spots [284]. If the grid size remains regular during measurements, it is
645 also possible to use statistical representations, e.g. histograms, frequency distribution or cumulative
646 probability plot, in order to compare more globally different parts of the structure [282]. Also, even if
647 there is no electrical continuity along the rebar, meaningful information about macrocell corrosion can
648 still be obtained using potential gradients [285].

649 *4.1.3. Relation to corrosion rate*

650 Many studies have tried to relate the corrosion potential to the corrosion rate, but no quantitative
651 correlation has been found. When measurements are made in highly controlled conditions (RH, T), a
652 robust correlation exists between the two parameters for small specimens, especially for the high
653 corrosion probability range [286]. However, in field investigation, the environmental factors cannot be
654 so controlled. In addition, measurements are influenced by several other factors, e.g. concrete
655 conditions (geometry, resistivity, cover depth, presence of cracks), the composition of the pore
656 solution (pH, chloride or sulphide content), the condition of the steel rebar (cathode-to-anode ratio),
657 and the availability of oxygen near the steel surface [168,272,284,287,288]. For example, very negative
658 potential values can simply be the results of a low level of oxygen. Hence, it is strongly recommended
659 to perform measurements at once in short time, as much as possible, in order to limit any variation of
660 these influencing factors. Despite being one of the most used technique for corrosion monitoring in
661 field, the half-cell potential technique must be used only as a qualitative test for locating areas with a
662 high corrosion risk on RC structures.

4.2. Concrete resistivity

Concrete resistivity (ρ , expressed in Ω m)—also referred to as electrical resistivity—is the ability of the material to oppose electrical circulation [289]. The initial resistivity of concrete is generally between 10 and 10^6 Ω m [290,291]. This value is mainly influenced by the w/c ratio, the type of binder, the size of the aggregates and the conditions of curing and storage, as they affect pore solution composition and concrete porosity [291,292]. Both parameters are important as they govern the corrosion process. Due to concrete degradation by the ingress of aggressive agents or the formation of corrosion-induced cracks, the resistivity is expected to change during the entire service life of RC structures. It is thus necessary to monitor concrete resistivity over time to assess the evolution of corrosion process.

4.2.1. Measurement

The resistivity is directly linked to the concrete resistance R_{Ω} (Ω) with the following equation (Eq. 2):

$$\rho = kR_{\Omega} = k \frac{\Delta V}{I} \quad (\text{Eq. 2})$$

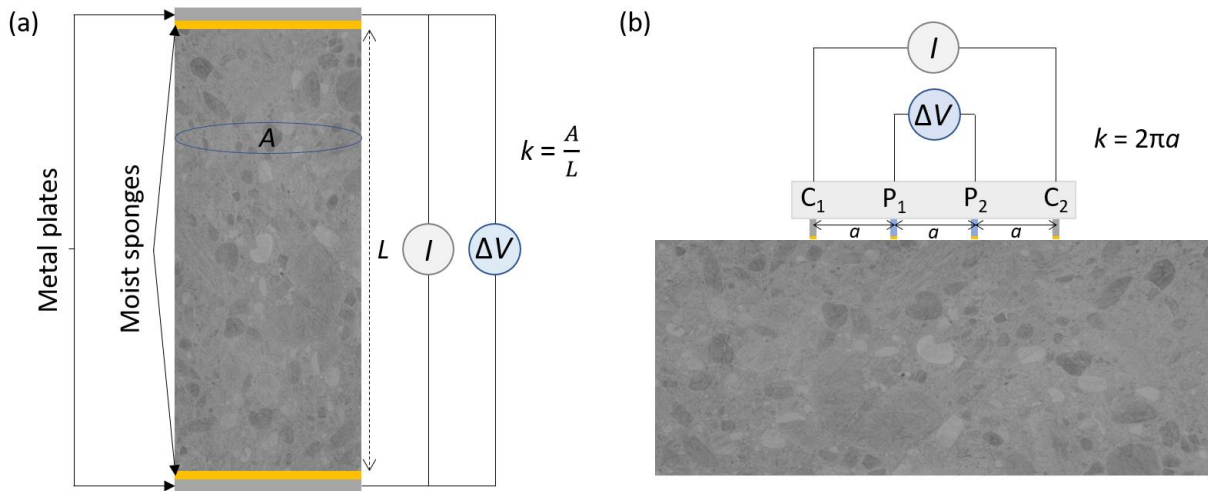
where ΔV is the potential difference (V), I is the injected current (A), and k is a geometric factor (m) that depends on the geometry and size of the sample, but also on the experimental device. Indeed, different procedures exist for measuring concrete resistivity [291]. In the bulk resistivity cell (uniaxial configuration, Fig. 9a), two parallel metal plates with moist sponges or a conductive gel, placed at the ends of the concrete sample, apply a current and the resulting potential difference on the two plates is measured [293]. In this case, the geometric factor k is (Eq. 3):

$$k = \frac{A}{L} \quad (\text{Eq. 3})$$

where A is the cross-sectional area perpendicular to the current (m^2) and L is the sample length (m). Even if the measurement of resistivity is rapid, this technique is used in laboratory experiments but hardly applicable to field work. The resistivity can also be measured using a four-electrode device (generally equipped with stainless-steel probes) on the concrete surface, in which two electrodes C_1 and C_2 inject a current and two electrodes P_1 and P_2 measure the resulting potential difference. Two systems are commonly used, the linear four-point probe and the square-array four-point probe, but other configurations, for example with embedded probes, exist as well [294]. In Wenner configuration (Fig. 9b), where C_1 and C_2 are the two external electrodes and P_1 and P_2 are the two internal electrodes with a similar probe spacing a (m), the geometric factor is (Eq. 4):

$$k = \frac{2\pi}{\frac{1}{a} - \frac{1}{2a} - \frac{1}{2a} + \frac{1}{a}} = 2\pi a \quad (\text{Eq. 4})$$

It is important to note that the use this relation assumed that the concrete is homogeneous and isotropic with a semi-infinite geometry, which is not the case for small concrete samples. To correct boundary effect and determine accurate geometric factors, it is possible to perform numerical simulations to determine a correcting factor for Eq. 4 [295] or to calibrate the device using an electrolyte of known resistivities in a core holder of similar geometry than the concrete sample.



694

695 **Figure 9.** Schematic representation of the resistivity measurement. (a) Bulk resistivity, (b) Surface resistivity in
 696 the Wenner configuration (typically, $a = 5$ cm).

697 The material and size of the electrodes and the way the electrolytic contact with the concrete surface
 698 is made can also affect the measurements, as can the measuring frequency. If the concrete resistivity
 699 can be measured either in DC or in AC mode, measurements are generally made in AC mode to avoid
 700 electrodes polarization [290,296]. Generally, measurements are carried out in the frequency range of
 701 0.5 to 10 kHz in the bulk configuration, and in the range of 0.01 to 10 kHz in the Wenner configuration
 702 [297]. Impedance spectroscopy must be done to determine the frequency at which the imaginary part
 703 of the impedance (reactance) is minimum to correctly assess the concrete resistance. This frequency
 704 must be defined case by case as it varies with concrete microstructure and moisture conditions.

705 *4.2.2. Relation to concrete durability*

706 From the concrete resistivity, one can determine the formation resistivity factor F_R , that represents
 707 the microstructural aspect of the concrete [294], according to the modified parallel law (Eq. 5):

$$F_R = \frac{1}{\varphi_R \beta_R} = \frac{\rho}{\rho_0} \quad (\text{Eq. 5})$$

708 where φ_R is the porosity of the system and β_R is the connectivity of the pore system, ρ is the resistivity
 709 of the bulk sample, and ρ_0 is the resistivity of the pore solution [298]. The formation factor is also
 710 defined as the ratio of the resistivity of the bulk sample and the resistivity of the pore solution [299].
 711 It can thus be used for determining the capillary porosity and pore tortuosity of fresh and hardened
 712 concrete [300,301]. This factor is also related to the diffusion coefficient through the Nernst-Einstein
 713 relationship (Eq. 6) [302,303]:

$$F_R = \frac{D_0}{D} \quad (\text{Eq. 6})$$

714 where D_0 is the self-diffusion coefficient of the ionic species in water (e.g. $D_0 = 2.032 \cdot 10^{-9} \text{ m}^2 \text{ s}^{-1}$ for Cl^-)
 715 and D is the effective diffusion coefficient ($\text{m}^2 \text{ s}^{-1}$). After determining the resistivity of the pore solution
 716 experimentally or theoretically [304–306], the diffusion coefficient of chloride in concrete can be
 717 determined in order to estimate the time to corrosion initiation by using Fick's second law of diffusion
 718 [294,307]. It is also possible to combine the formation factor with Langmuir or Freundlich adsorption

719 isotherm, and to predict either chloride ingress with the Nernst-Planck equation [308,309] or the
720 apparent chloride diffusion coefficient in concrete [310]. The use of concrete resistivity therefore is a
721 good indicator of the concrete durability in terms of ion diffusivity and fluid transport [311–313].

722 The measurement of concrete resistivity is influenced by several parameters that can adversely affect
723 the determination of the formation factor. The main such factors are water content and temperature;
724 an increase in one of these two increases the ionic transport in the pore solution and decreases the
725 resistivity of the concrete [291,314–316]. The effect of temperature is even more complicated as it
726 also affects the solubility of the hydrated phases in concrete, resulting in a change in pore solution
727 composition [317]. Normalization of the temperature effect on concrete resistivity has been used for
728 predicting the resistivity variation due to temperature changes [318]. As the concrete surface interacts
729 directly with the surrounding atmosphere, the exposure conditions must be correctly defined as they
730 will impact the concrete resistivity and create a resistivity gradient. As discussed in Section 3.2.1,
731 concrete carbonation results in a progressive change of the concrete microstructure, also creating a
732 resistivity gradient in the concrete [319].

733 When using a four-electrode configuration, other parameters must be considered when performing
734 the measurement as some assumptions are made to interpret the data, i.e. concrete is homogeneous
735 and isotropic with a semi-infinite geometry [320]. The size and geometry of the specimen must then
736 be considered accurately for determining the geometrical factor k as the assumption of a semi-infinite
737 medium cannot be respected for small samples [314,321]. In addition, the presence of cracks and the
738 distribution of aggregates in the concrete are inconsistent with a homogeneous and isotropic material
739 [291]; regardless of the type of cracks, the measurements will be under- or over-estimated if they are
740 made nearby [322]. Finally, the presence of rebar affects the measurement of resistivity as a distortion
741 of the current field or a short-circuit are likely to occur (known as rebar effect) [291,323,324],
742 decreasing the part of the current flowing only in the concrete. Several studies have shown that the
743 rebar diameter and spacing, the concrete cover depth, the direction of the probe, the probe spacing
744 and the distance from the rebar all affect the measurements [295,324–332]. Hence, the
745 recommendation suggests measuring the concrete resistivity as far as possible from the reinforcement
746 to obtain the most accurate value [290,296]. If measurements are performed close to the rebar mesh,
747 the most suitable configuration to determine the resistivity has the probe located parallel to and
748 midway between the top rebars [329]. If measurements are done in front of a rebar, a rebar factor can
749 be defined and applied in Eq. 4 for correcting the resistivity for the rebar effect [295,333].

750 *4.2.3. Relation to corrosion rate*

751 Many studies have tried to correlate concrete resistivity with corrosion rate of steel, as the rate-
752 determining step of corrosion can be related to the ionic transport between anode and cathode which
753 is dependent on concrete resistance [334]. It is generally assumed that the corrosion rate is inversely
754 proportional to concrete resistivity, especially when corrosion is in active state [334–339]. According
755 to RILEM recommendation, the risk of corrosion is high when concrete resistivity is lower than 100 Ω
756 m and negligible when it is higher than 1000 Ω m for OPC concrete [290,296]. However, it is not
757 specified whether these values consider the rebar effect while it highly decreases the measured
758 apparent resistivity. Even if a wide scatter exists [105], accurate correlations between the two
759 parameters have been proposed [340,341] and empirical correlations have also been successfully
760 determined for the monitoring of real structures (e.g. [342]). However, this apparent relationship does

761 not mean that the resistance of concrete dominates the overall resistance of the process. In fact, it can
762 be attributed to the degree of pore water saturation as both parameters are influenced by the water
763 content. Indeed, increasing the water content lowers concrete resistivity and increases corrosion rate,
764 and vice versa [170].

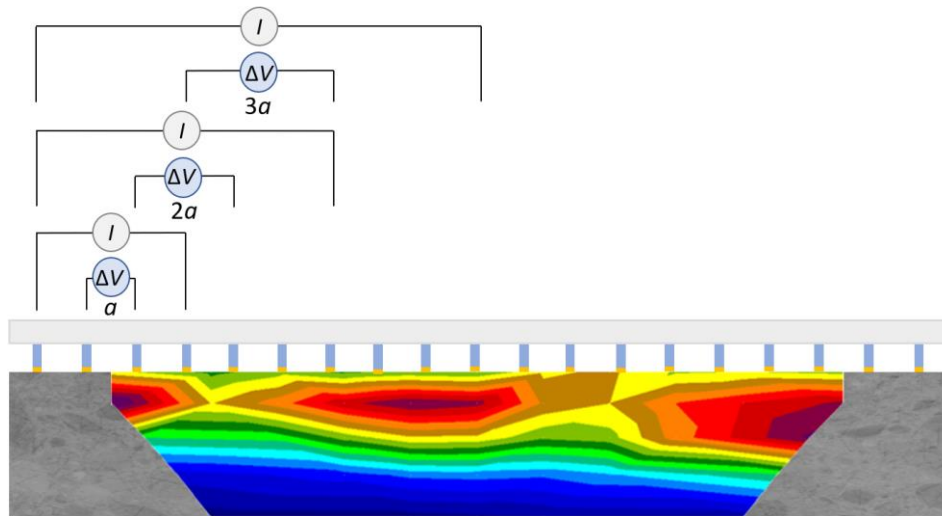
765 If the RILEM recommendation is still commonly used, the range of resistivity values for assessing
766 corrosion activity varies with the studies. For example, the limit of resistivity values indicating high
767 corrosion intensity varies between 50 and 200 Ω m, while the limit of resistivity values indicating low
768 corrosion intensity varies between 85 and 2000 Ω m [334]. This discrepancy can notably be related to
769 the influence of the type of binder on the absolute value of resistivity [334]. It has been shown that a
770 rebar can corrode at relative similar rates when embedded in a low resistive mortar prepared only
771 with Portland cement or in a high resistive mortar prepared with a mix of Portland cement and fly ash
772 [343]. If the cement type is known, the absolute resistivity can be compared to reference value for that
773 cement type obtained in laboratory in the relevant exposure conditions to determine more accurately
774 the risk of corrosion [105,290]. Otherwise, it is very challenging to use these critical values in the case
775 of existing structures with lacking information about their composition. Finally, we must remember
776 that the specimen size has a great influence on the corrosion process [211], which can explain the
777 scatter between laboratory and field experiments.

778 Hence, no general correlation between concrete resistivity and corrosion rate could be determined
779 [337,343–345]. It has also been shown that concrete resistivity and corrosion rate evolve differently
780 with temperature, the first following an Arrhenius-type equation [346] and the second following the
781 Eyring law [347], which could also explain the absence of a general correlation between them. To sum
782 up, the use of concrete resistivity can be interesting for evaluating non-destructively the risk of
783 corrosion and estimating the range of corrosion rate when the cement type is known. It is also possible
784 to compare the gradient in resistivity to obtain a meaningful information on the risk of corrosion, as
785 for the half-cell potential technique. However, it cannot be used as a unique method for determining
786 precisely the corrosion rate. It is nevertheless a parameter of prime interest that must be measured as
787 accurately as possible for further determination of the corrosion rate, as discussed in sections 4.3.1
788 and 4.3.2.

789 *4.2.4. Interest of electrical tomography*

790 The concrete resistivity measured as presented in the above sections corresponds to an “apparent”
791 resistivity that considers all elements in the investigated area. Therefore, this value only reflects an
792 average value on a defined volume and does not consider the inherent heterogeneity of concrete
793 [348]. A multi-electrode device, consisting of an assemblage of single devices with four electrodes, can
794 be used to perform an electrical resistivity tomography (ERT) of the concrete [348,349]. With such
795 method, it is possible to determine the resistivity at different levels/depths in order to reconstruct the
796 spatial distribution of the resistivity in the material (Fig. 10). Results are presented as pseudo-sections
797 showing the distribution of apparent resistivities in the material. Inversion models are then required
798 to determine the “true” resistivities at the corresponding depth of the concrete from the measured
799 apparent resistivities. Softwares such as Res2Dinv and Res3Dinv are commonly used for such inversion,
800 especially in geophysics [350], but further research is required to define a standardized method for
801 measuring and inversion modelling in reinforced cement-based materials [351]. After performing the
802 inversion algorithm, pseudo-sections of true resistivities are obtained. As a result, the rebar effect

803 observed on the apparent resistivities has been removed as the resistivities are now correctly
804 distributed in the volume [352].



805

806 **Figure 10.** Schematic representation of a multi-electrode device in Wenner configuration for ERT measurements.
807 Several probes spacing, e.g. a , $2a$ and $3a$ as shown in the figure, are required to investigate the concrete section
808 in depth. A 2D pseudo-section of true resistivities after inversion with Res2Dinv is also provided to illustrate
809 possible results. Courtesy: J. Gance.

810 One limitation when performing ERT is the variation in contact resistance between the electrodes and
811 the concrete surface, which affects the quality of the obtained data. Systems using embeddable
812 electrodes are being developed to ensure a good electrolytic contact during the entire measurement
813 [353,354]. Other limitation concerns the low spatial resolution of electrical tomography [351]. It has
814 to be noted that the probe configuration has an impact on the sensitivity of the measurement: for
815 example, the Wenner array has a good sensitivity to vertical changes but a low sensitivity to horizontal
816 changes [350]. Thus, using several probe configurations and spacing, complementary data may be
817 obtained to increase the data quality and the spatial resolution. An accurate grid of electrodes is thus
818 required for the monitoring of RC structures.

819 Studies have shown that ERT can be used to visualize the carbonation process, the ingress of water
820 and chloride and all transport properties in the material over time, in both undamaged and cracked
821 cement-based materials [351,355–358]. Indeed, for Portland-based materials, an increase in concrete
822 resistivity can generally be attributed to the carbonation front due to pore clogging while a decrease
823 can be attributed to the ingress of water and chlorides or the formation of cracks. However, all these
824 phenomena are susceptible to occur simultaneously depending on the exposure environment. It is
825 then necessary to determine first the influence of each phenomenon separately on the range of
826 resistivity values in order to determine if it is possible to differentiate the contribution of each
827 parameter on the resistivity profile. ERT measurements must be done over time to compare the
828 relative evolution of resistivity pseudo-sections to determine the actual level of concrete deterioration.
829 The results could also be used to determine the diffusion of CO_2 , carbonates and chlorides in the
830 material to better predict the length of the initiation stage. During the propagation stage, ERT
831 measurements could give insights on the water content of the material, especially in the vicinity of the
832 rebar, to determine if steel corrosion occurs in wet or dry conditions at the time of the measure.
833 Despite all these opportunities, many challenges in electrical tomography remain open to its
834 applicability in field studies [351].

835

4.3. Polarization resistance

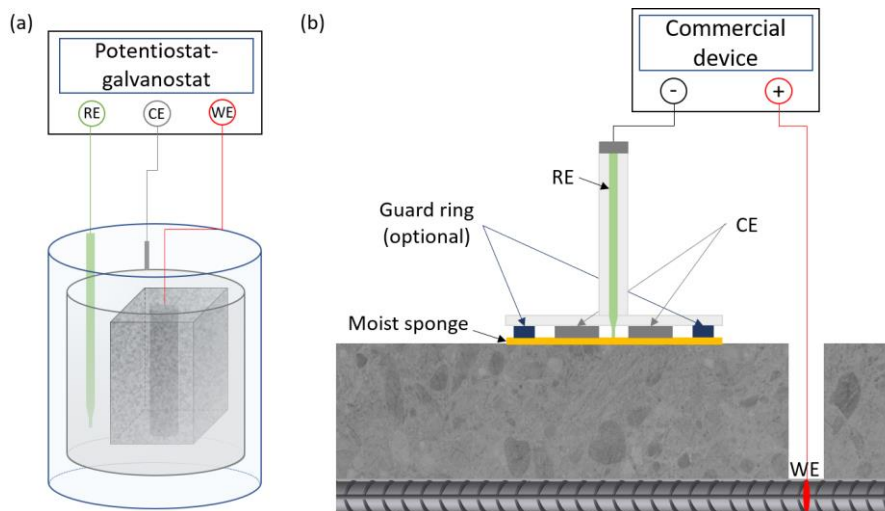
836 Polarization resistance (R_p , expressed in Ω) is the resistance of the rebar to oxidation during the
837 application of an external potential, i.e. during polarization of the rebar. Several electrochemical
838 methods have been developed for determining R_p [105,338,359], using three- or four-electrode
839 configurations. The different techniques discussed hereafter are based on the application of an
840 external perturbation on the system to polarize the rebar. The electrochemical noise technique, which
841 appears as a great tool for corrosion analysis because measurements are performed without any
842 electrical perturbation, is not discussed as its applicability to RC structures is still limited.

843

4.3.1. Measurement in three-electrode configuration

844 In the three-electrode configuration, the electrochemical system consists of a working electrode (WE)
845 —the steel rebar—, a reference electrode (RE, as described in section 4.1.1) used for measuring the
846 rebar potential, and a counter electrode (CE, generally stainless steel, titanium or platinum) that closes
847 the electrical circuit (Fig. 11). Providing a description of the electrode configuration is important as all
848 three electrodes can influence the measurement [360,361]. Hence, data on the type and position of
849 the RE, the material and the geometry of the CE, and the use of surface electrodes with a specific
850 electrolytic contact or embedded electrodes should be provided in all studies [362].

851

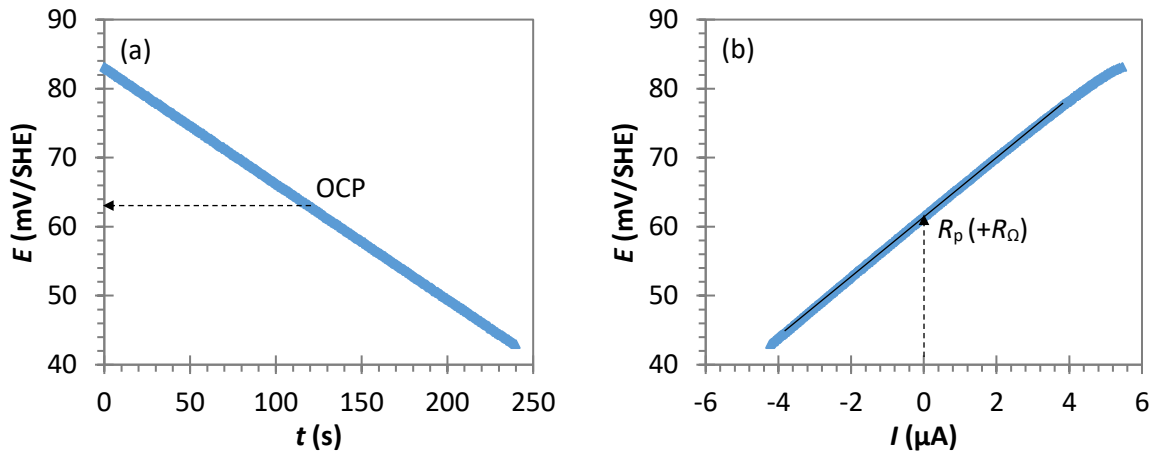


852 **Figure 11.** Schematic representation of a three-electrode configuration. (a) For laboratory experiments,
853 measurements are generally performed on small samples in solution using a potentiostat-galvanostat; the rebar
854 acts as the working electrode (WE), the reference electrode (RE) is generally a saturated calomel electrode (SCE)
855 and the counter electrode (CE) is a mesh cylinder that surrounds the sample to homogenize as much as possible
856 the current distribution in the material. Alternatively, RE and CE can be embedded in concrete. (b) In the field,
857 measurements are generally made with a commercial device equipped with a RE in the centre and a CE (disc with
858 inner and outer diameter), both placed on a moist sponge on the concrete surface. Optionally, an auxiliary
859 electrode known as the guard ring is used to supposedly confine the current to a known area of steel.

860 The linear polarization resistance (LPR) technique consists of applying a small potential sweep on the
861 rebar around its open circuit potential (generally $OCP \pm 10-20$ mV, either in the anodic or in the cathodic
862 direction) and recording the resulting current (Fig. 12) [117,363]. Alternatively, the measurement can
863 be made by applying a current sweep and recording the resulting potential [364]. Polarization
864 resistance is given by the tangent for zero net current of the potential-current curve (Eq. 7).

$$\frac{\Delta E}{\Delta I} = R_p \quad (\text{Eq. 7})$$

865 Please note that the slope is not directly equal to R_p , but represents the sum of polarization resistance
 866 and concrete resistance [16]. It is therefore necessary to compensate the ohmic drop R_Ω to determine
 867 IR-free values of R_p [105,365]. If another technique must be used in complement to determine R_Ω ,
 868 some instrumentation directly incorporates an automatic compensation of the ohmic drop.

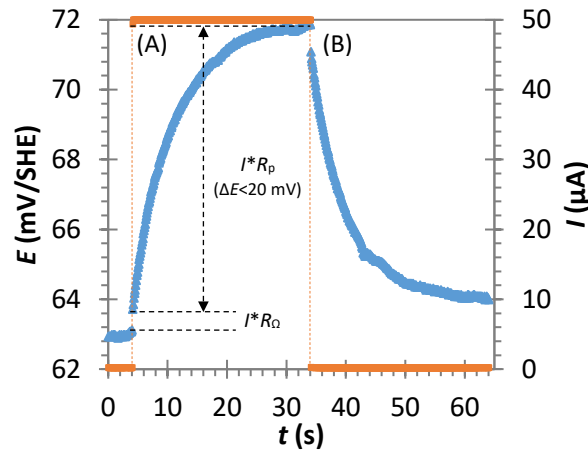


869
 870 **Figure 12.** Example of an LPR measurement in the cathodic direction from +20 mV to -20 mV vs. OCP. (a)
 871 Evolution of the potential with time applying a potential sweep of 10 mV min^{-1} , (b) Evolution of the potential
 872 with a current during the potential sweep, allowing the determination of R_p .

873 The sweep rate is a critical parameter for accurate evaluation of the polarization resistance, as it is
 874 required that the system is stabilized at each potential during the measurement. Typically, in
 875 agreement with gravimetric mass loss (ASTM G1 standard), a reliable measurement of R_p for active
 876 corrosion (i.e. current density values over $1 \mu\text{A cm}^{-2}$) can be obtained using a sweep rate between 2.5
 877 and 10 mV min^{-1} in potentiodynamic mode [105], 10 mV min^{-1} being the common recommended value
 878 (ASTM G5 standard). However, in the case of passive reinforcements, the corrosion current density is
 879 overestimated by a factor of between 2 and 10 compared to the gravimetric study using this sweep
 880 rate value [366]. To obtain a closer value than that expected for passive corrosion (i.e. below $0.1 \mu\text{A}$
 881 cm^{-2}), slower sweep rates—even less than 2.5 mV min^{-1} —should be used. In controlled conditions such
 882 as in laboratory experiments, this is not a problem as the time required for measuring generally is not
 883 a limiting factor, and LPR experiments can be systematic. However, for field investigations, as the
 884 measurement time is a critical parameter, the results obtained for passive rebar must be used with
 885 care as the polarization resistance will probably be underestimated [366,367].

886 The second method used for determining R_p is the pulse technique. The measurements are generally
 887 made in galvanostatic mode [368,369], but they can also be done in potentiostatic [370–372] or
 888 coulometric mode [373,374]. In the galvanostatic mode (galvanostatic pulse, GP), a low anodic DC
 889 current (generally $I_{\text{app}}=5\text{-}500 \mu\text{A}$) is applied to the reinforcement during a short time (typically 5-30 s
 890 for active corrosion) in anodic or cathodic direction and the transient potential is recorded until
 891 stabilization [105]. Rapidly after the polarization, a strong potential increase occurs due to the ohmic
 892 resistance of the concrete; a further progressive increase until reaching a steady state occurs
 893 afterwards due to the electrical double layer effect (Fig. 13). For validating the assumption of linearity

894 between current and potential, the potential shift should not exceed 20 mV [105]. When the current
 895 is turned off, a similar behaviour as that recorded during the charge occurs during discharge.



896

897 **Figure 13.** Example of GP measurement in the anodic direction showing the injection of 50 μA during 30 s and
 898 the evolution of ΔE with time during (A) the charge (current applied) and (B) the discharge (no current applied).

899 Based on the Randles circuit, which consists of the ohmic resistance R_Ω in series with a parallel
 900 combination of the double layer capacitance C_{dl} and the polarization resistance R_p , the polarization at
 901 any time t can be expressed as (Eq. 8):

$$E_t = I_{app} \left[R_p * \left[1 - \exp\left(\frac{-t}{R_p C_{dl}}\right) \right] + R_\Omega \right] \quad (\text{Eq. 8})$$

902 The expression is generally linearized for calculating R_p and C_{dl} (Eq. 9):

$$\ln(E_{max} - E_t) = \ln(I_{app} * R_p) - \frac{t}{R_p C_{dl}} \quad (\text{Eq. 9})$$

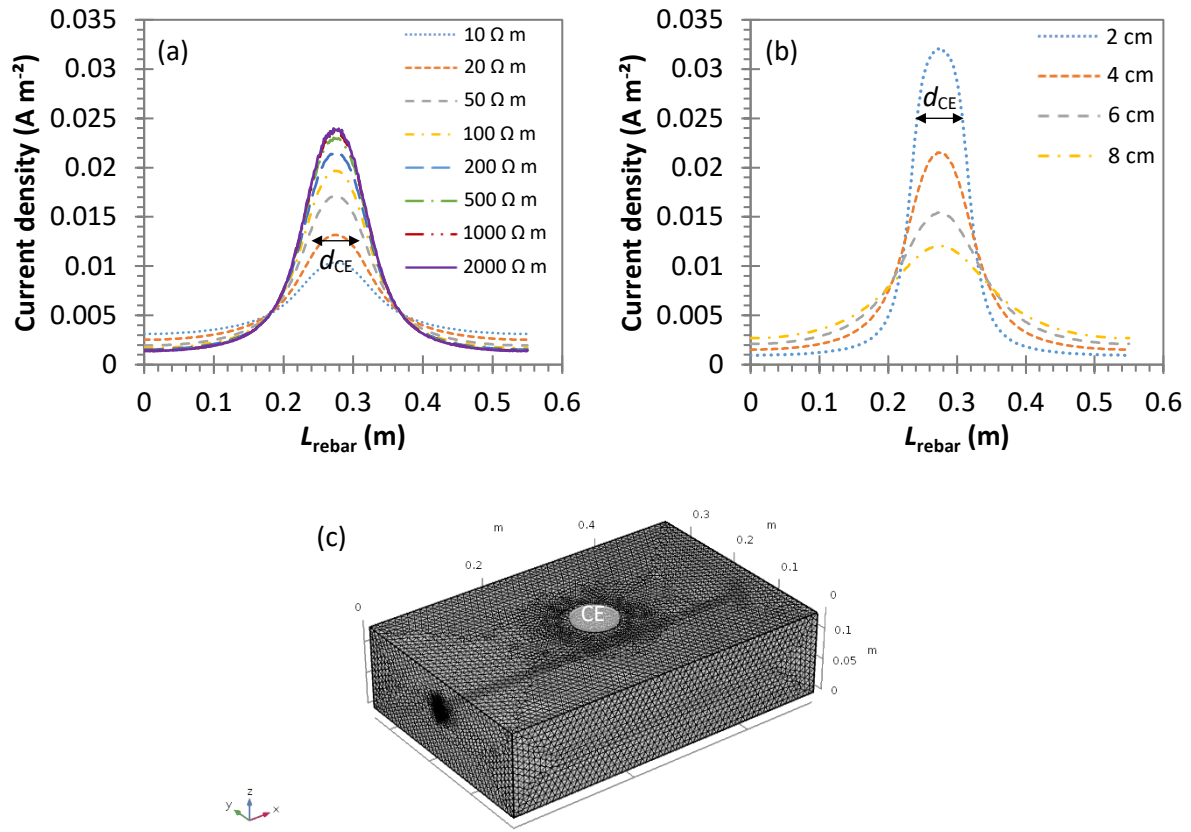
903 where E_{max} is the steady-state potential value. A curve fit can also be used for calculating the different
 904 parameters (Eq. 10):

$$E_t(t) = K_0 - K_1 \exp\left(\frac{-t}{K_2}\right) = I_{app}(R_p + R_\Omega) - (I_{app}R_p) \exp\left(\frac{-t}{R_p C_{dl}}\right) \quad (\text{Eq. 10})$$

905 Alternatively, a modified Randles circuit using a parallel combination of a constant phase element (CPE)
 906 and a polarization resistance R_p in series with a Warburg element Z_w , can be used for modelling the
 907 steel-concrete interface [375].

908 The area of the rebar that is polarized during measurement must be determined for an accurate
 909 conversion of the polarization resistance in corrosion rate. An auxiliary electrode—known as the guard
 910 ring (Fig. 11b)—is often used for confining the polarization to a known surface of the rebar, generally
 911 assumed to be the area below the counter electrode [376]. When modelling galvanostatic pulse
 912 measurements with a finite-element method, it was shown that in the case of uniform corrosion, for
 913 small concrete samples with one carbon steel rebar, a decrease in concrete resistivity or an increase
 914 in cover depth result in an increased lateral dispersion of the current on the rebar, i.e. in a decrease in
 915 the part of the current under the counter electrode, both in the presence (see [377]) or absence (see
 916 Fig. 14) of a guard ring. Thus, assuming that only the area below the CE is polarized, only a fraction of
 917 the total current impressed by the counter electrode must be considered for a correct assessment of

918 polarization resistance, this fraction depending mainly on concrete resistivity, cover depth, the
 919 geometry of the CE and the size of the sample (border effects).



920

921

922 **Figure 14.** Effect of concrete parameters on the distribution of current density along the upper ridge (the most
 923 strongly polarized part) of the rebar using the GP technique in the case of uniform corrosion ($i_0=10 \mu\text{A cm}^{-2}$). (a)
 924 Concrete resistivity ρ ($\Omega \text{ m}$) for 4 cm cover depth, (b) Cover depth (cm) for $\rho=200 \Omega \text{ m}$. Simulations solved a
 925 secondary current distribution in a temporal study (evaluated here at 30 s) with a finite-element method using
 926 COMSOL Multiphysics 5.3a software. The dimension of the concrete domain was $55 \times 34 \times 13 \text{ cm}^3$ with one low-
 927 carbon steel pure iron rebar ($\Phi=12 \text{ mm}$, $\sigma=5.10^6 \text{ S m}^{-1}$). The concrete domain acts as the electrolyte with uniform
 928 conductivity and electric isolation at the external boundaries of the material. Potential and current density
 929 distribution were solved with Ohm's law and charge conservation law in the concrete domain with extremely
 930 fine mesh. The corrosion reaction on the steel surface was modelled as boundary condition (electrode surface)
 931 using the general Butler-Volmer equation (Eq. 1, with $\alpha_a=\alpha_c=0.5$, $E_{\text{corr}}=-0.78 \text{ V}$, $T=20 \text{ }^\circ\text{C}$). (c) The counter electrode
 932 of the GP device was modelled using several geometries, here shown as a 7-cm-diameter cylinder on the concrete
 933 surface directly above the rebar centre. A current source was applied to the counter electrode at $100 \mu\text{A}$. The
 934 positive sign in the y-axis indicates anodic polarization.

935 In the case of passive rebar, longer times ($>100 \text{ s}$) are needed to reach a steady-state potential
 936 compared to active corrosion. This can be explained by the low capacity of the passive rebar to
 937 consume an anodic polarizing current, resulting in the lateral propagation of current into the rebar,
 938 especially when the latter is long [377]. Duration of the pulse is thus the most important parameter in
 939 the determination of polarization resistance as it can be significantly underestimated with short-time
 940 measurements [377,378]. Hence, as for the LPR technique, the results obtained from GP
 941 measurements in the field must be used with care in the case of passive reinforcements if the steady-
 942 state potential is not reached.

943 In the case of a non-uniform corrosion, where anodic and cathodic zones are spatially separated but
 944 electrically connected, the direction and magnitude of polarization will affect the current distribution
 945 on the rebar [379]. Generally, in anodic polarization mode, the anodic zones will receive more current
 946 per area than the cathodic zones, while the opposite is true in cathodic polarization mode [377,379].
 947 Due to the different ohmic and capacitive contributions of the anodic and cathodic areas, it is
 948 important to consider the spatial and time-dependent distribution of the impressed current to
 949 correctly interpret the results obtained from GP measurements [380].

950 The third method to determine R_p is electrochemical impedance spectroscopy (EIS) [381,382]. This
 951 consists of applying a small-amplitude alternating potential difference (5-20 mV peak-to-peak) or
 952 current at different frequencies f and measuring the resulting current or potential, respectively. For a
 953 potential modulation (Eq. 11):

$$E(t) = |\Delta E| \cos(\omega t) \quad (\text{Eq. 11})$$

954 the current response is (Eq. 12):

$$I(t) = |\Delta I| \cos(\omega t + \varphi) \quad (\text{Eq. 12})$$

955 where ω is the angular frequency (rad, with $\omega=2\pi f$) and φ is the phase ($^\circ$).

956 In AC condition, the property related to the opposition of a circuit to an electrical current is called
 957 impedance (Z). Each circuit element, whether resistor, capacitor or inductor, has an impedance. If the
 958 resistance created by a resistor is independent of the frequency ($Z_R=R$), the resistance created by a
 959 capacitor or an inductor depends on the frequency ($Z_C=\frac{1}{j\omega C}$ and $Z_L=j\omega L$), creating a phase shift between
 960 voltage and current. As the sinusoidal current or voltage can be represented as a rotating vector, the
 961 impedance can be divided into two components, a real component and an imaginary one (Eq. 13)
 962 [382]:

$$Z = Z_{re} + jZ_{im} \quad (\text{Eq. 13})$$

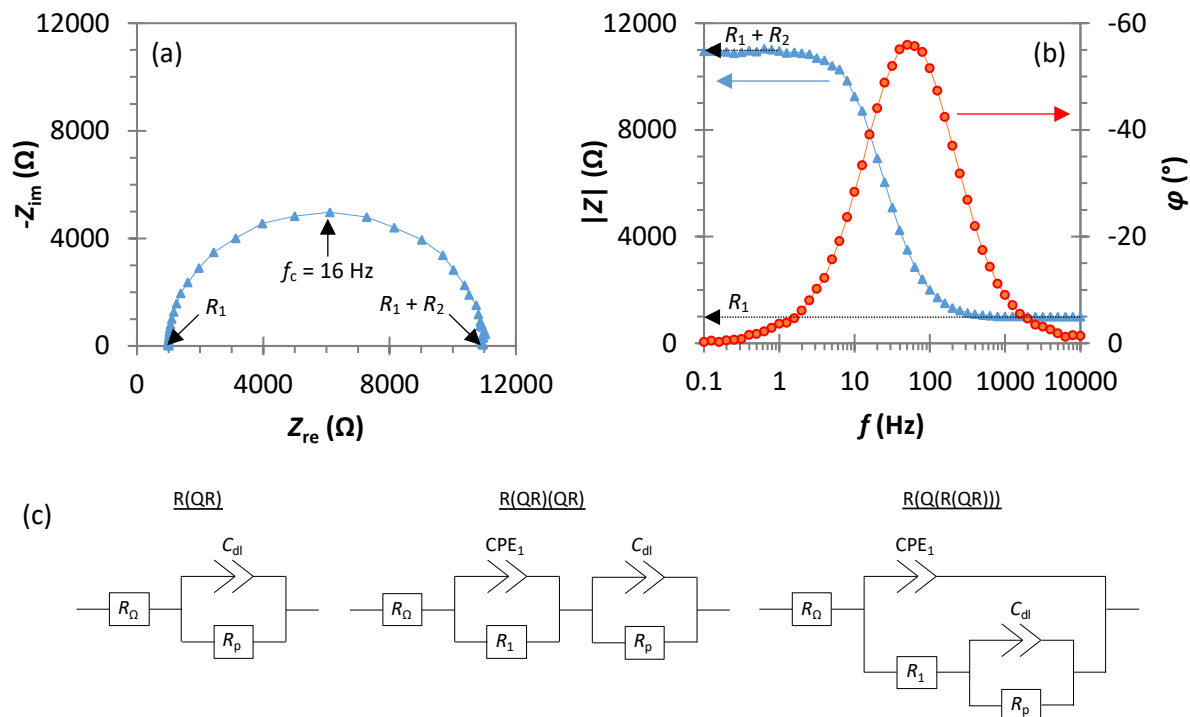
963 where the real component is the resistance R and the imaginary one is the reactance X (conductance
 964 or inductance). The modulus and phase of the impedance are then defined (Eqs. 14-15):

$$|Z(\omega)| = \sqrt{Z_{re}(\omega)^2 + Z_{im}(\omega)^2} \quad (\text{Eq. 14})$$

$$\varphi(\omega) = \tan^{-1}\left(\frac{Z_{im}(\omega)}{Z_{re}(\omega)}\right) \quad (\text{Eq. 15})$$

965 Different data plots are used to represent the results obtained by EIS. The Nyquist plot is obtained by
 966 plotting Z_{re} on the x-axis and $-Z_{im}$ on the y-axis (Fig. 15a). The R_p value is determined at low frequencies
 967 where the plot intercepts the x-axis (on the right side of the plot), considering the concrete resistance
 968 that is determined at high frequencies (on the left side). The Bode plot is obtained by plotting $\log(f)$ on
 969 the x-axis and $|Z|$ or φ on the y-axis (Fig. 15b). On a Bode plot using the Z modulus, the R_p value is
 970 determined according to the low-frequency plateau (on the left side), by considering the concrete
 971 resistance that is determined at high frequencies (on the right side). In practice, only part of the low-
 972 frequency loop is obtained, and the plot must be extrapolated for obtaining the R_p value by using an
 973 equivalent electrical circuit (EEC) [375,383,384]. Selection of the EEC is crucial to accurately evaluate
 974 the corrosion process. Among the different EECs [385–387], some of the most used for simulating steel

975 corrosion in concrete—involving several resistances and capacitors representing the properties of the
 976 electrolyte, the corrosion reaction or even the passive film—are shown on Fig. 15c. Commonly, the
 977 capacitive elements are replaced by constant-phase elements (CPE, also noted Q) to consider the non-
 978 ideal behaviour of the physical elements (leaking capacitor, $Z_{CPE} = \frac{1}{Q(j\omega)^n}$) [388,389].



979
 980
 981 **Figure 15.** Example of (a) Nyquist plot and (b) Bode plot obtained at 10 mV RMS between 10^4 and 10^{-1} Hz with
 982 10 points per decade using a dummy cell with parameters $R_1=1000 \Omega$, $R_2=10000 \Omega$ and $C=1 \mu\text{F}$. (c) Examples of
 983 electrical equivalent circuits for fitting the experimental results in the case of steel corrosion in concrete, from
 984 left to right: $R(QR)$, $R(QR)(QR)$ and $R(Q(R(QR)))$. In addition to the resistance of the electrolyte, the polarization
 985 resistance and the double layer capacitance, the additional parameters can be attributed to the passive film.

986 EIS is a powerful technique for mechanistic investigations as it can be used to determine several
 987 parameters, such as the bulk concrete properties at high frequencies [390–392], the mass-transfer
 988 phenomena and diffusion coefficients [393–395], or the properties of the passive film on the steel
 989 surface at low frequencies [90]. In alkaline solutions, it was shown that EIS measurements can provide
 990 insight into the mechanism of the cathodic reduction at the oxide layer of carbon steel, allowing
 991 characterization of the oxide film [396]. The proposed methodology includes the use of a power-law
 992 distribution and a complex capacitance representation of the data when using a CPE for describing the
 993 film impedance [396].

994 The main advantages of the two DC methods are the short time and “standard” equipment required
 995 for the measurements as compared to EIS. However, the latter generally provides a more accurate
 996 value of polarization resistance in the case of passive reinforcement [366]. If it is possible to limit the
 997 use of low frequencies to decrease to time required for analysis, the accuracy of the R_p value obtained
 998 in this case may be affected irrespective of the selected EEC. Alternatively, an analysis of the alternative
 999 current and potential in the time-domain can also be performed at only one selected frequency
 1000 [397,398]. The methodology consists of a fast-Fourier transform and subsequent harmonic analysis of
 1001 the time-domain signal. The advantage of the harmonic analysis is that it doesn’t required any

1002 conversion of the polarization resistance as it provides directly the corrosion current density and the
1003 Tafel constants, in addition to decreasing the measurement time. A good agreement with conventional
1004 techniques is found as long as the selected frequency is lower than the characteristic frequency f_c , i.e.
1005 the frequency at which the imaginary component of the impedance reaches its maximum [398]. More
1006 studies are still required to demonstrate the applicability of this technique for the monitoring of RC
1007 structures.

1008 Several drawbacks in the determination of the polarization resistance with this three-electrode
1009 configuration exist for field experiments. First, the area of the counter electrode must be larger than
1010 the reinforcement to avoid any perturbation during measurement [361], which is hardly feasible in
1011 real structures. It is also difficult to assess the area of steel polarized during the measurement. Though
1012 the use of a guard ring with modulation has been proposed to confine the current below the counter
1013 electrode, many studies have shown that it often fails and contributes to the polarization of the rebar,
1014 thus compromising the measurement [156,377,379,399–404]. Notably, in the case of macrocell
1015 corrosion, the polarized area can be different than the supposed confinement area if the anodic site is
1016 located far from the counter electrode [402]. During anodic polarization, the current from the counter
1017 electrode and the guard ring will preferentially polarize the active area as the current follows the path
1018 of lowest polarization resistance. During cathodic polarization, this current will spread over the passive
1019 areas, showing the incapacity of the guard ring to effectively confine the current whatever the
1020 polarization direction [405]. Finally, the main drawback of this configuration is the need of an electrical
1021 connection to the rebar, requiring breakout of local parts of the concrete to make the measurement.
1022 Alternatives have thus been proposed to tackle this issue, as discussed hereafter.

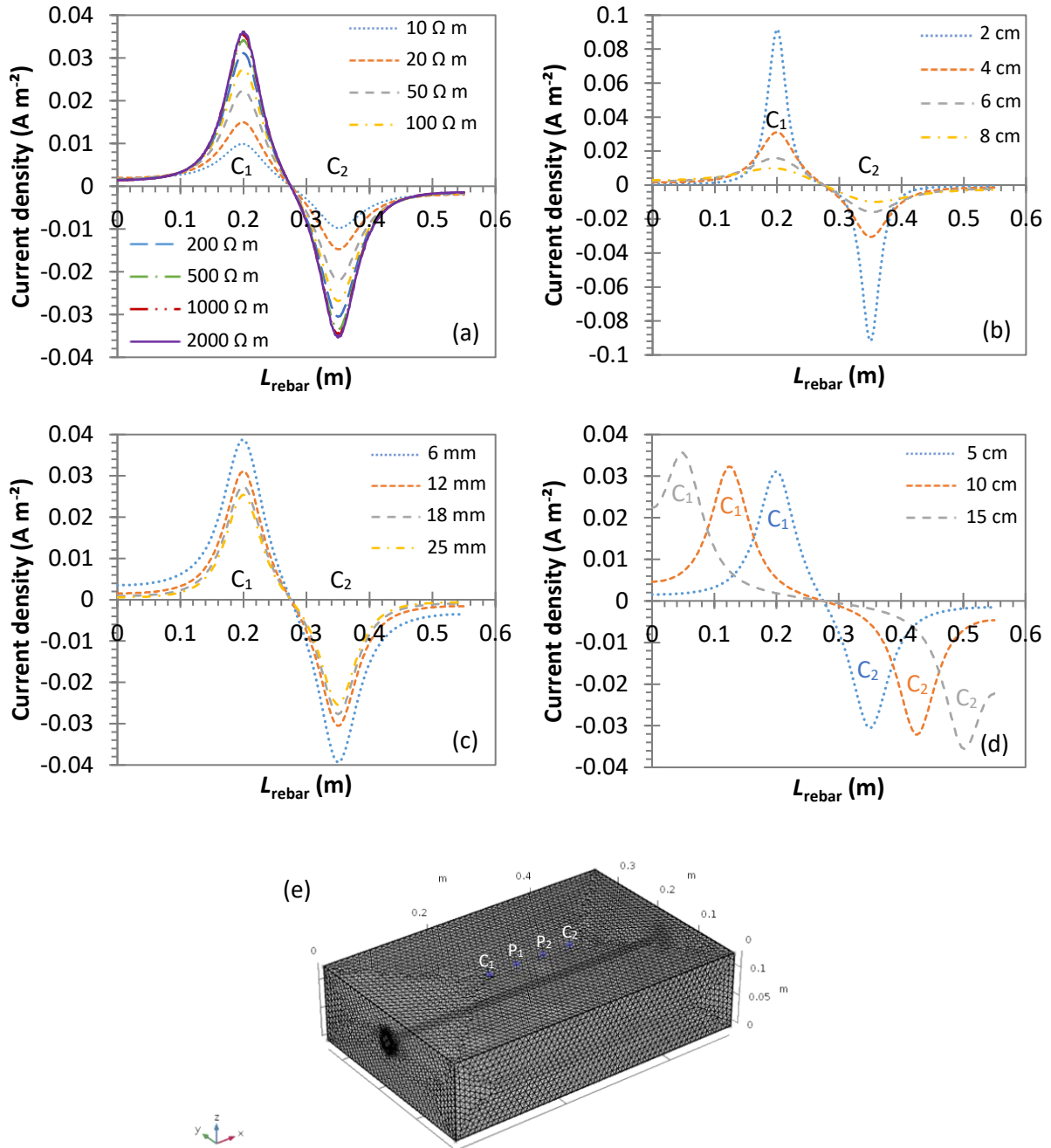
1023 *4.3.2. Measurement in four-electrode configuration*

1024 Several techniques have been proposed for estimating the polarization resistance without connection
1025 to the rebar, which can be referred to as indirect polarization, using a four-electrode array on the
1026 concrete surface [366,406–413]. The most common one is the Wenner configuration, where the four
1027 electrodes are aligned with a constant electrode spacing (as already shown in Fig. 9b). Measurements
1028 can be done by imposing a direct current [414–416] or an alternative current at several frequencies
1029 [417–421]. The DC method can be referred to as indirect GP—similar to time-domain induced
1030 polarization (TDIP) used in geophysics—while the AC method can be referred as indirect EIS—similar
1031 to spectral induced polarization (SIP) used in geophysics.

1032 The material of the potential electrodes can be an important parameter, especially for time-domain
1033 measurements. Indeed, the potential difference between two polarizable electrodes, e.g. stainless
1034 steel, is unstable due to self-potential. This self-potential must be accurately determined for correcting
1035 both polarization resistance and double layer capacitance obtained from the transient potential
1036 induced by the current injection. Electrodes of the second kind, e.g. Ag/AgCl or Cu/CuSO₄, can be used
1037 as they are more stable, non-polarizable and thus have lower self-potential values than stainless steel
1038 [422]. The size and geometry of the electrodes may also influence the measurement.

1039 In four-electrode configuration, only a fraction of the current injected on concrete surface polarizes
1040 the rebar, the rest will flow exclusively in concrete. The current distribution in the material depends
1041 on the time or frequency of measurement and the state of the rebar. For an actively corroding rebar,
1042 the distribution is very similar at high and low frequencies due to the low polarization resistance, the
1043 current penetrating the rebar perpendicularly to its surface [411]. The current distribution is symmetric

1044 about the centre of the device, one side being anodically polarized and the other being cathodically
 1045 polarized [377]. By numerical simulations, it was shown that an increase in the concrete resistivity, a
 1046 decrease in the cover depth and an increase in the rebar diameter result in the increase in the total
 1047 current that polarize the rebar [377]. In addition, the increase in the electrode spacing of the
 1048 monitoring device increases the total current that reach the rebar and the polarized area (Fig. 16).



1049

1050

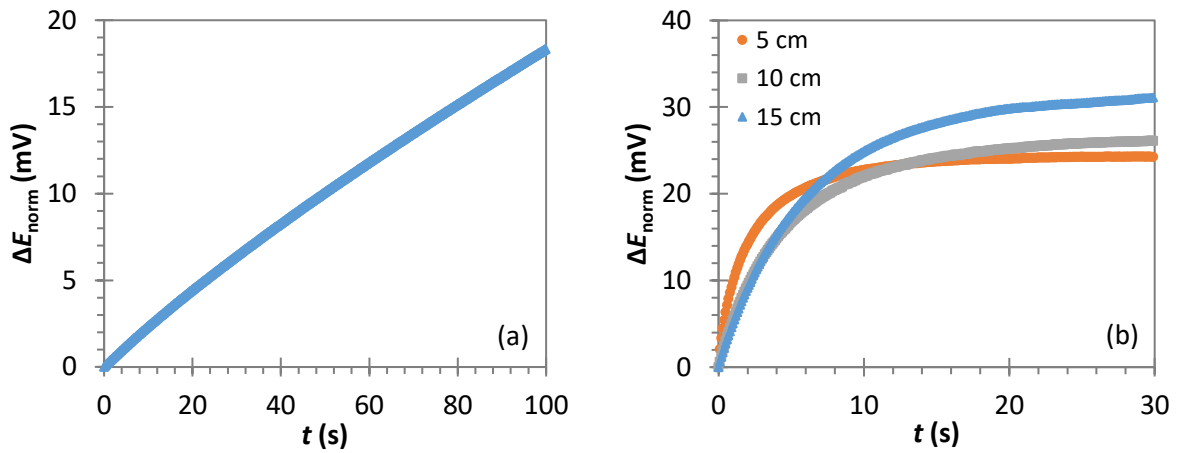
1051

1052

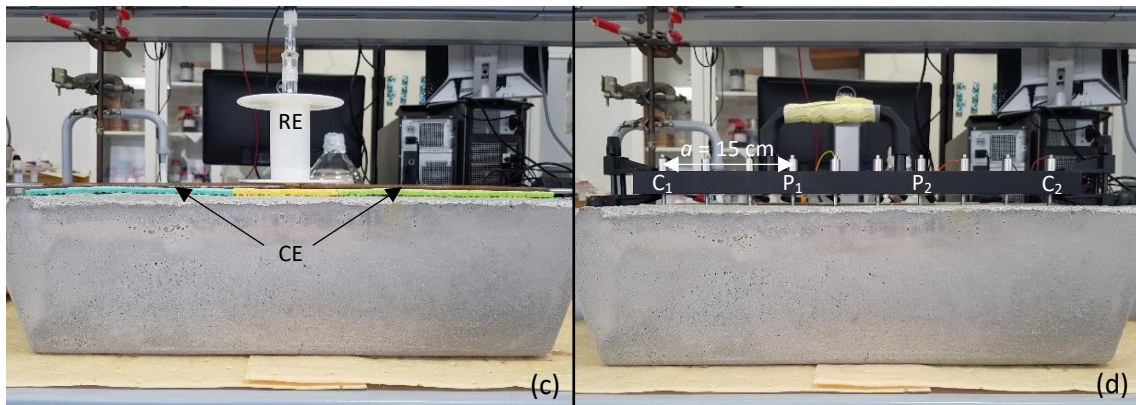
1053 **Figure 16.** Effect of concrete and monitoring parameters on the distribution of the current density along the
 1054 upper ridge of the rebar using the indirect galvanostatic pulse technique in case of uniform corrosion ($i_0=10 \mu\text{A}$
 1055 cm^{-2}). (a) Concrete resistivity ρ ($\Omega \text{ m}$) for 4 cm cover depth, $\Phi=12 \text{ mm}$ and electrode spacing $a=5 \text{ cm}$. (b) Cover
 1056 depth (cm) for $\rho=200 \Omega \text{ m}$, $\Phi=12 \text{ mm}$ and $a=5 \text{ cm}$. (c) Rebar diameter (mm) for $\rho= 200 \Omega \text{ m}$, 4 cm cover depth
 1057 and $a=5 \text{ cm}$ (d) Electrode spacing a (cm) for $\rho=200 \Omega \text{ m}$, 4 cm cover depth and $\Phi=12 \text{ mm}$. Details of the

1058 simulations and input parameters are on Fig. 14. The four electrodes of the Wenner device were modelled as
 1059 perfect point objects on the concrete surface (e). Point current sources impressed 100 μA in C_1 and $-100 \mu\text{A}$ in
 1060 C_2 . The positive sign in the y-axis indicates anodic polarization.

1061 For passive rebar, the distribution is quite different depending on the frequency. At high frequencies,
 1062 the interface behaves essentially as a capacitance and the current penetrates the rebar
 1063 perpendicularly to its surface as for actively corroding rebar, whereas at low frequencies the rebar acts
 1064 as an insulator and only a small part of the current polarizes the rebar [411]. The current distribution
 1065 is not symmetric due to the low capacity of a passive rebar to consume an anodic-polarizing current
 1066 compared to a cathodic-polarizing current. Hence, errors are expected when determining the
 1067 polarization resistance. However, the system tends to become symmetric with increasing resistivity,
 1068 resulting in a better estimation of the polarization resistance for highly resistive concrete ($>5000 \Omega \text{ m}$)
 1069 [411]. The time required for reaching the quasi-steady-state is substantially less as compared to the
 1070 conventional GP method, as shown by numerical simulations [406,412] and experiments (Fig. 17).



1071



1072

1073 **Figure 17.** GP measurements using (a) three-electrode and (b) four-electrode configurations on a passive rebar.
 1074 Experiments were done on a CEM I 52.5R (Lafarge) mortar sample ($55 \times 34 \times 13 \text{ cm}^3$, $w/c=0.4$) with one ribbed
 1075 carbon steel rebar (60 cm, $\Phi=12 \text{ mm}$, cover depth 3.3 cm), at constant relative humidity (dry conditions, ≈ 30 -
 1076 40% RH) and temperature ($23 \text{ }^\circ\text{C}$). In the three-electrode configurations (c), measurements were conducted with
 1077 a mercury/mercurous sulphate reference electrode located at the centre of the sample, and a stainless-steel
 1078 counter electrode ($55 \times 10 \text{ cm}$) placed on moist sponges on the sample surface directly above the rebar. In the
 1079 four-electrode configuration (d), stainless-steel or brass electrodes ($\Phi_i=3 \text{ mm}$, $\Phi_e=5 \text{ mm}$) were used in Wenner
 1080 configuration, centred directly above and parallel to the rebar. The electrolytic contact was made with moist
 1081 sponges placed inside the probes. Electrode spacing a was 5, 10 or 15 cm. A potentiostat-galvanostat (PMC-2000,

1082 Princeton Applied Research) was used for galvanostatic pulse measurements. The impressed current was 10 μA
 1083 between rebar and counter electrode in the three-electrode configuration, while it was 200 μA between C_1 and
 1084 C_2 in the four-electrode configuration. The results indicate that a quasi-steady-state is not reached after 100 s in
 1085 the three-point configuration, while it is almost reached after 30 s in the four-point configuration.

1086 This result could be explained by the fact that the current polarizing the rebar is not constant but
 1087 decreases with time before reaching a constant value, which depends notably on the exchange current
 1088 density i_0 and concrete resistivity (Fig. 18). For a constant i_0 , the increase in concrete resistivity results
 1089 (i) in an increase in the part of the current polarizing the rebar I_{rebar} , as the current preferentially flows
 1090 within the least resistive path (i.e. the rebar) and (ii) in a longer time required for reaching the quasi-
 1091 steady state. For a constant resistivity, the decrease in the exchange current density i_0 results in a
 1092 decrease in the total current polarizing the rebar.

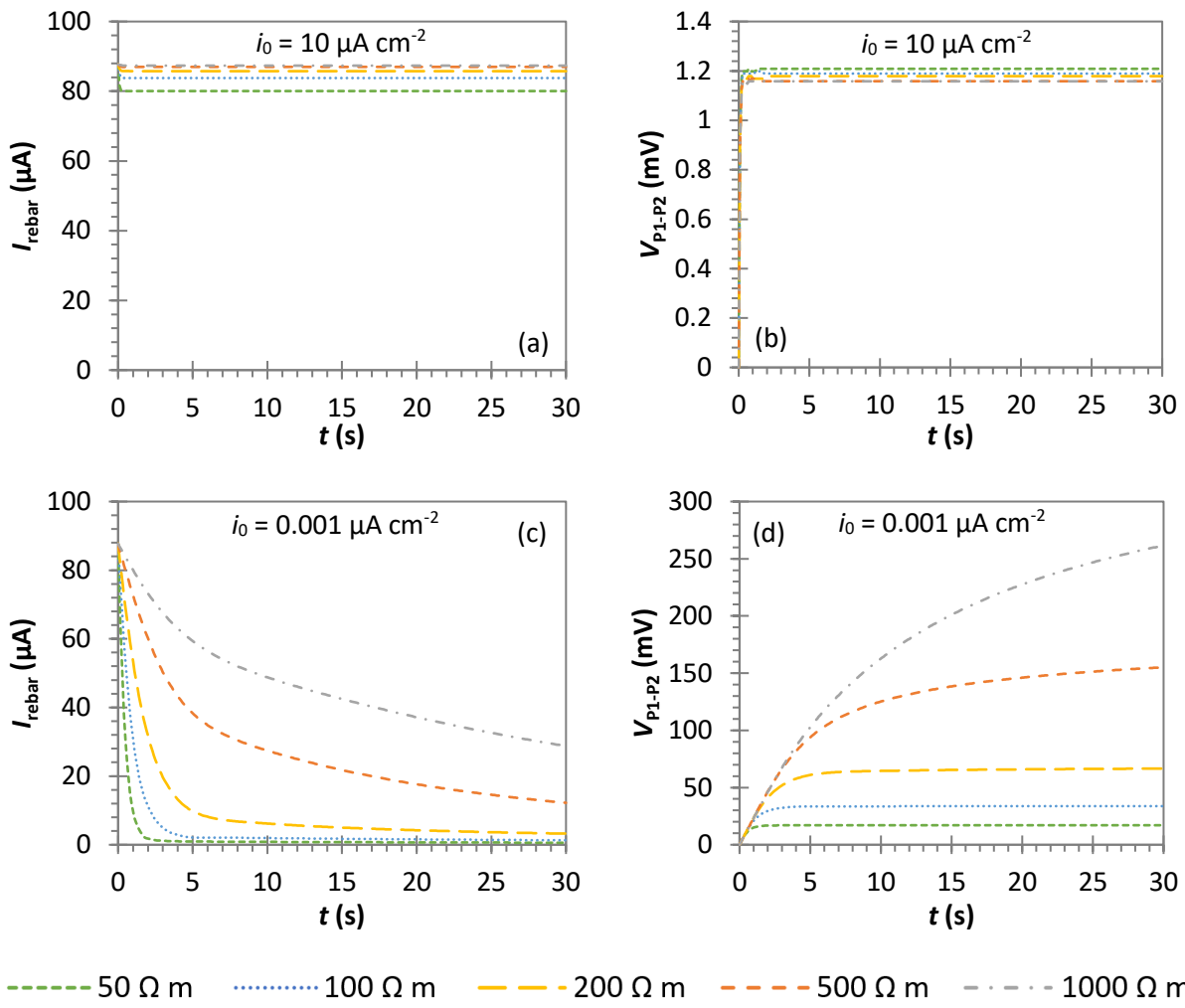


Figure 18. Effect of current exchange density i_0 , considering uniform corrosion, on the current polarizing the rebar and on the potential measured between P_1 and P_2 (the ohmic drop is not shown here as the first point was normalized to 0 V), for a double layer capacitance of 0.2 F m^{-2} and for resistivities between 50 and 1000 $\Omega \text{ m}$. (a and b) $i_0=10 \mu\text{A cm}^{-2}$ (active corrosion), (c and d) $i_0=0.001 \mu\text{A cm}^{-2}$ (passive corrosion). Simulation details are on Figs. 14 and 16. The cover depth was fixed at 3.3 cm, like the laboratory sample presented on Fig. 17. The parameters for the Butler-Volmer equation are $\alpha_a=\alpha_c=0.5$ and $E_{\text{corr}}=-0.78 \text{ V}$ for active corrosion and $\alpha_a=0.012$, $\alpha_c=0.5$ and $E_{\text{corr}}=0.16 \text{ V}$ for passive corrosion.

1103 In the case of non-uniform corrosion, it has been shown that indirect EIS method in Wenner
1104 configuration can be used to localize highly corroding areas if they are beneath to or at the vicinity of
1105 the current-injecting electrodes, as two distinct time constants can be observed instead of one time
1106 constant in uniform corrosion [421]. The authors attributed the high-frequency response to the
1107 actively corroding section and the low-frequency response to the passive areas. Otherwise, when the
1108 corroding area is located beneath the potential probes, almost no sign of active corrosion is detected.
1109 The sensitivity of this method to localize non-uniform corrosion is dependent on the length of the
1110 actively corroding area, the magnitude of the corrosion rate, and the resistivity of the cement-based
1111 material [421]. Using indirect GP method, it appears hardly possible to localize non-uniform corrosion
1112 based on a single measurement as a similar response is expected on the zero-frequency limit for both
1113 passive and localized corrosion [421]. It appears still possible to differentiate active and passive areas
1114 by performing several measurements along the rebar and comparing the results to a reference value.
1115 Reversing the polarization direction may also help to identify corroding areas. Indeed, in GP
1116 configuration, the cathodic and anodic zones will be primarily polarized near the cathodic and anodic
1117 probes, respectively [377]. However, even close to the cathodic probe, the anodic zones will receive
1118 more current per area than the cathodic zones, the magnitude depending on the cathode-to-anode
1119 ratio and the concrete resistivity [377]. It is then expected that the resulting potential difference will
1120 be different according to the polarization direction, but this aspect must be confirmed experimentally.

1121 Another advantage of the four-electrode configuration is the supposed self-confinement of the current
1122 in case of uniform corrosion when the rebar is long enough (>1 m), irrespective of concrete resistivity,
1123 cover depth, rebar diameter or exchange current density [411]. The sensitivity of the potential probes
1124 is different using the four-electrode compared to the three-electrode configuration. Even if a large
1125 section of the rebar is polarized, the potential probes may not be sensitive to changes that occur too
1126 far away from them. An effective polarized area which depends on the probe spacing can thus be
1127 defined [423]. If the highest sensitivity arrays are found near the potential electrodes, the measured
1128 potential difference differs depending on the probe configuration [350]. Thus, using several probe
1129 configurations and probe spacing, complementary data may be obtained to assess the different
1130 corrosion states on a single rebar [348].

1131 Current developments of the four-electrode configuration are thus very promising, but the method is
1132 not mature and required further experimental and numerical studies. Some parameters that must be
1133 considered for its correct assessment include the contact resistance between the electrodes and the
1134 concrete surface, the non-uniformity of corrosion, and the presence of rebar mesh with different
1135 corrosion states. Also, all simulations presented previously assumed homogeneous cover depth and
1136 concrete resistivity. Gradients in concrete resistivity representative of RC structures must be applied
1137 for correct assessment of the current distribution in the material. As the sensitivity of the indirect EIS
1138 to detection of non-uniform corrosion has been demonstrated, the use of electrical tomography can
1139 be very useful to determine the distribution of the polarization resistance along large rebars and to
1140 estimate the length of the actively corroding area. Due to the similarity with concrete resistivity
1141 measurement device, the development of a multi-electrode device for characterizing both concrete
1142 resistivity and polarization resistance profiles using indirect polarization is of prime interest [424].

1143

4.3.3. Relation to corrosion rate

1144 Polarization resistance can be used to calculate the corrosion current I_{corr} in order to estimate the
 1145 corrosion rate of steel CR . According to RILEM recommendation [105], the corrosion current is
 1146 determined using the Stern-Geary relation (Eq. 16) [363]:

$$I_{\text{corr}} = \frac{B}{R_p} \quad (\text{Eq. 16})$$

1147 where B is the Stern-Geary constant (V). If B is generally assumed to be 0.026 V for active corrosion
 1148 and 0.052 V for passive corrosion of steel in concrete [425], these values do not reflect the complexity
 1149 and variation with time of the corrosion process [426,427]. Accurate values of B should be determined
 1150 empirically according to Eq. 17:

$$B = \frac{\beta_a \beta_c}{\ln(10) * (\beta_a + \beta_c)} \quad (\text{Eq. 17})$$

1151 where β_a and β_c are the anodic and cathodic Tafel constants (V), respectively. The Tafel constants can
 1152 be determined by applying a strong polarization to the electrode (OCP±150-250 mV) and recording the
 1153 current. The two coefficients are determined by plotting $\log(I)$ as a function of the overpotential η (E -
 1154 E_{eq}), according to the Butler-Volmer equation (Eq. 1). Unfortunately, the Tafel slopes are often not
 1155 determined on field and can be difficult to measure accurately, mainly because the anodic part of the
 1156 polarization curve is not always linear [168,428–431]. Moreover, the strong polarization during the
 1157 Tafel scan can cause irreversible changes to the steel rebar, which is an important drawback of this
 1158 technique [432]. Hence, the use of the recommended values of 0.026 and 0.052 V can still provide an
 1159 accurate estimate of the corrosion current, with generally an error of less than one order of magnitude
 1160 according to the experimental values of β_a and β_c reported in the literature [162,370,431,433].

1161 Considering uniform corrosion, Faraday's law is then often used for converting I_{corr} to CR (Eq. 18):

$$CR = \frac{I_{\text{corr}} M}{nF} \quad (\text{Eq. 18})$$

1162 where CR corresponds to the mass loss (g s^{-1}), I_{corr} is the corrosion current I_{corr} (A), M is the molar mass
 1163 of iron (g mol^{-1}), n is the number of electrons exchanged in the reaction ($n=2$) and F is the Faraday
 1164 constant. In terms of corrosion penetration rate (cm s^{-1}), the equation is (Eq. 19):

$$CR = \frac{I_{\text{corr}} M}{nA\rho_{\text{steel}}F} \quad (\text{Eq. 19})$$

1165 where A is the rebar surface (cm^2) and ρ_{steel} is the steel density (g cm^{-3}). For example, considering
 1166 uniform corrosion of black carbon steel, a current density (I_{corr}/A) of $1 \mu\text{A cm}^{-2}$ is equivalent to a
 1167 corrosion rate of $11.6 \mu\text{m year}^{-1}$ [105].

1168 Gravimetric weight-loss tests are often done according to the ASTM G1 standard to compare the
 1169 results obtained by this direct and destructive method to the results obtained indirectly from the
 1170 determination of the polarization resistance. It results that LPR, GP and EIS techniques can accurately
 1171 estimate the corrosion rate for actively corroding rebars in laboratory conditions, as the polarized area
 1172 is known [359,366,434]. As differences in R_p values can be observed depending on the choice of the
 1173 technique and its operating conditions, e.g. sweep rate, waiting time, polarization time or applied

1174 frequencies [105,378,435], it may be useful to carry out all methods to determine the most efficient
1175 one for each case, or to obtain an average value [436]. For field experiments, as the polarized area is
1176 generally not known, the accuracy of these techniques can be limited as already developed in section
1177 4.3.1. In the four-electrode configuration, Fahim *et al.* have shown that the corrosion rate can be
1178 accurately estimated for active corrosion and even for passive corrosion in the case of a highly resistive
1179 concrete [377,411], confirming the great interest of this configuration. Further studies are still required
1180 to determine the applicability of this technique to quantify the corrosion rate on RC structures.

1181 We must note that the Stern-Geary relationship (Eq. 16) was defined for uniform corrosion on the basis
1182 of the mixed-potential theory by Wagner and Traud, which is fundamentally not applicable for the
1183 corrosion of steel in RC structures where macrocell corrosion is expected [156,426,437,438]. For a
1184 similar reason, the use of Faraday's law for calculating the penetration rate is generally invalid,
1185 especially in the case of chloride-induced corrosion [439]. A new theoretical analysis has been
1186 proposed to calculate the corrosion rate of localized corrosion from GP measurements [380]. This
1187 approach can reduce the overestimation of the corrosion rate to a factor of maximum 2 instead a
1188 factor of 10 or more that can be obtained using the conventional Stern-Geary approach. Two elements
1189 that takes into account the different behaviour of the macrocell elements upon excitation are
1190 considered: the first is related to the fact only a fraction of the injected current flows through the
1191 anodic element and the second to the fact that this current is not constant over time during
1192 measurement. Both elements can be estimated empirically from the concrete resistivity, the cover
1193 depth and the steel surface area related to the concrete surface. As these parameters can be
1194 determined in RC structures, this approach appears feasible in engineering practice [380]. If this
1195 perspective has been proposed for the interpretation of GP measurements with the conventional
1196 three-electrode configuration, a similar approach should be done for the four-electrode configuration.

1197 *4.4. Limitation on the evaluation of corrosion rate and interest of combining NDT methods*

1198 The measurement of the polarization resistance only provides an instantaneous estimation of the
1199 corrosion rate, which is strongly dependent on the operating conditions. Hence, a single measurement
1200 cannot determine a representative annual corrosion rate if the daily and seasonal changes are not
1201 properly considered [439–441]. Considering environmental factors is essential for any accurate
1202 evaluation of the corrosion rate, in both laboratory and field studies. In real structures, the range of
1203 water content and temperature values will depend on the geographic location of the structures, and
1204 large variabilities are expected due to natural weathering through day-night and seasonal cycles, or
1205 natural wetting/drying cycles, resulting in gradients for both parameters [440,442].

1206 However, changes in environmental conditions may not be directly observed inside concrete. Though
1207 temperature changes are rapidly reflected, even at thicknesses over 30 mm, this is not the case for RH
1208 changes for which only the surface layers are generally affected by drying processes [443–445]. Hence,
1209 temperature appears to be the primary climatic factor affecting the corrosion rate under atmospheric
1210 conditions [443]. It is important to note that the number and frequency of drying events can affect this
1211 conclusion, as the water content can become low even in depth if no wetting event occur for a long
1212 period [446]. The presence of cracks can also influence the effect of drying, which gives a greater
1213 importance of RH on the corrosion rate during corrosion propagation stage [446]. Finally, it appears
1214 that RH and T interact with each other, so they cannot be considered separately [447].

1215 As both parameters can strongly vary, even over a single day, a measurement procedure must be
1216 defined for the accurate extrapolation of instantaneous measurements to annual corrosion rates and
1217 to incorporate the RH and T changes into service life models [448–450]. One solution is to carry out
1218 several measurements at specific times with very different conditions, at least four-times a year, to
1219 study the seasonal cycle for calculating an average value. A five-year study has shown that a power
1220 law is a good mathematical function to fit the experimental values of cumulative steel thickness loss
1221 over time for RC contaminated with chloride, exposed to both controlled and outdoor conditions [451].
1222 This mathematical function can then be used for extrapolating the results to estimate the service life.

1223 Under passive conditions, no strong influence of RH and T on the corrosion rate was reported
1224 [447,452]. It should thus be possible to differentiate passive and active corrosion simply by measuring
1225 the minimum and maximum corrosion rates. However, in the case of active corrosion, instantaneous
1226 corrosion rates are more affected by RH and T , with maximum values measured in moist and low
1227 resistive concrete. In addition, the corrosion rate can be orders of magnitude higher for corrosion
1228 induced by chloride (up to 1 mm year⁻¹) than by carbonation (up to 30 $\mu\text{m year}^{-1}$) in outdoor exposure
1229 [453]. Determination of the corrosion rate in extreme cases, i.e. low T and RH or high T and RH, can
1230 provide information on the expected minimum and maximum corrosion rates specific for each
1231 structure [454]. However, as the average corrosion rate can be much lower than the maximum value,
1232 this range may be too imprecise to obtain any meaningful information on the remaining service life.

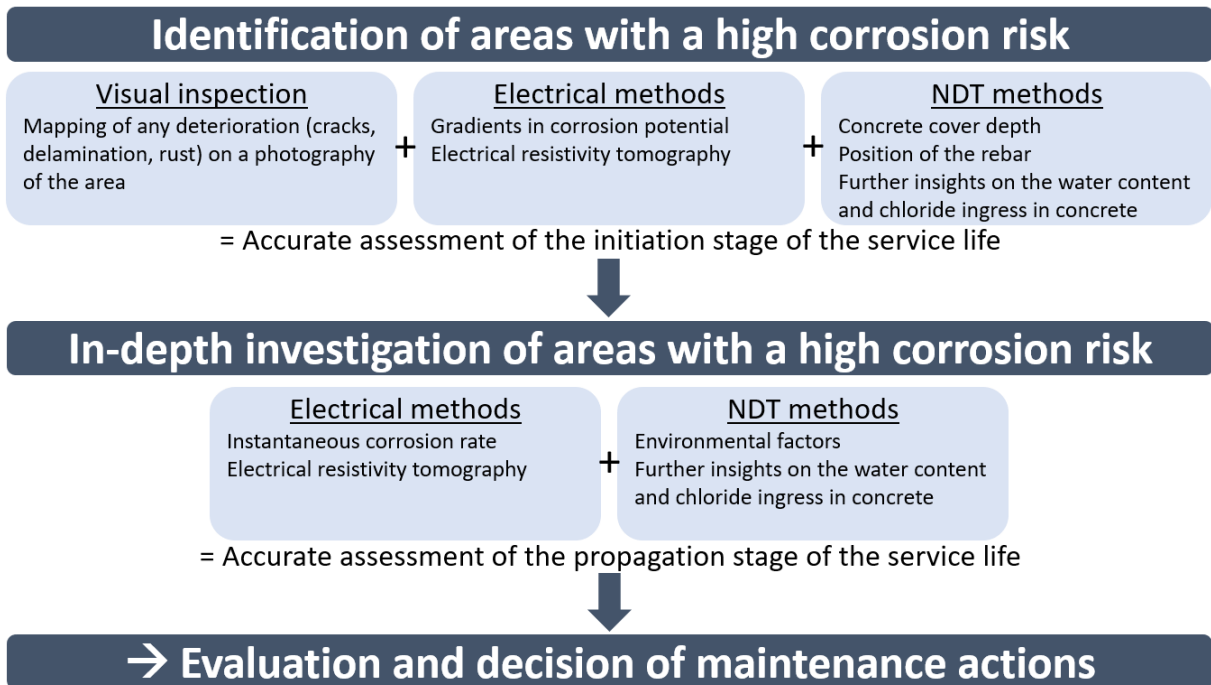
1233 Hence, it appears that determination of the corrosion rate based on measuring the polarization
1234 resistance should be complemented by other measurements. A multi-parameter approach combining
1235 electrical and other NDT methods should (i) reduce the errors resulting from measurements, and (ii)
1236 improve synergistically the estimation of service life of the reinforced concrete [5,455,456] (Fig. 19).
1237 First, a full surface inspection assesses the global state of the reinforced concrete. This includes a visual
1238 inspection of the concrete reporting any visible deterioration, e.g. surface cracks, delamination or rust
1239 [284,457]. The mapping of cracks, delamination and other defects in the concrete can be done with a
1240 crack-width ruler and acoustic-wave techniques, including the impulse-response method, impact-echo
1241 testing or ultrasonic techniques [17,458–460]. The results of the surface inspection can be provided
1242 on photography and defines the main defect points for further investigations.

1243 Electromagnetic, elastic wave, optical sensing and infrared thermography methods are widely used in
1244 civil engineering for inspecting hard surfaces such as concrete [15,461–464]. They are mainly used for
1245 determining concrete cover depth and locating rebars with an estimate of their diameter [465]. Recent
1246 works have shown that capacitive technique and ground-penetrating radar (GPR) can also be used for
1247 monitoring rebar corrosion [466] and for providing information on water content [465,467,468] and
1248 chloride ingress [469,470]. Comparing the results obtained with ERT measurements, which can also be
1249 used to evaluate the water gradient, chloride penetration or carbonation depth [355,356], is of great
1250 interest to improve the reliability of the service life. It is also possible to complement these
1251 measurements by using embeddable chemical or optical-fibre sensors for the monitoring of pH,
1252 chloride concentration or temperature at several depths [338,471,472]. This is of great interest for
1253 assessing the initiation stage of corrosion, but their installation on existing structures can be
1254 challenging. At the end of this inspection, critical areas with a high corrosion risk can be determined.

1255 On the weak spots, an in-depth investigation must assess the corrosion rate by determining the
1256 polarization resistance during the propagation stage of service life. The determination of the water
1257 and ionic content in concrete using ERT or embeddable chemical/optical-fibre sensors should allow to

1258 consider the environmental factors and estimate the electrochemically active surface of steel to
 1259 correctly convert the polarization resistance into corrosion rate. In addition to NDT measurement, core
 1260 sampling can be done at different critical locations to perform gravimetric loss tests. Though this is a
 1261 destructive method, further insights on the minimum and maximum corrosion rates and other
 1262 parameters of importance, e.g. concrete compressive strength, can be obtained under controlled
 1263 conditions in laboratory.

1264 Each technique provides specific information for crosschecking the results from other techniques. Data
 1265 integration methods used in the operating system will further improve the overall quality of diagnosis
 1266 [472], but the advantage and cost associated to each technique should be considered as well for
 1267 determining the optimal methodology for each specific case. In the future, automated data collection
 1268 by means of flying drones and climbing robots is expected to facilitate the inspection of RC structures
 1269 and reduce the global cost of diagnosis [11]. The possibility of using a robotic device equipped with
 1270 different NDT equipment is of prime interest to improve the evaluation of corrosion.



1271

1272 **Figure 19.** Procedure for the evaluation of RC structures by combining electrical and other NDT methods.

1273 **5. Conclusions and perspectives**

1274 We reviewed the current knowledge on corrosion mechanisms of carbon steel in concrete and the
1275 advances in electrical methods for non-destructive testing and evaluation of corrosion rates. One main
1276 challenge for understanding corrosion mechanisms is the heterogeneity of RC structures. Concerning
1277 cement-based materials, the knowledge of pore size distribution and pore interconnectivity is crucial
1278 as they affect the transport of aggressive agents and corrosion products through the material.
1279 Concerning steel rebar, the presence of local surface defects or inclusion substantially affects the
1280 electronic properties of the steel. The steel-concrete interface can then be very different even for
1281 replicate samples, resulting in a lack of data reproducibility. Consequently, the results obtained from
1282 different studies may be hardly comparable, especially where the description of materials and
1283 methods is incomplete. A systematic description of concrete and steel microstructures and of the
1284 operating conditions is required for the development of a database to improve our understanding of
1285 corrosion mechanisms.

1286 Most corrosion experiments are done in laboratory conditions considering uniform corrosion on small
1287 and artificial samples. As natural corrosion is a slow process, notably because of the potentially long
1288 initiation stage, accelerated tests are generally used for studying the corrosion mechanism induced by
1289 carbonation or by chloride. However, the properties of the steel-concrete interface may not be
1290 representative of natural corrosion. In addition, the corrosion process is affected by a size effect.
1291 Hence, extrapolating laboratory results performed with a single rebar to a large structure with
1292 interconnected rebars remains challenging, and special care must be taken regarding the design and
1293 preparation of the samples to obtain meaningful information for field application.

1294 Concerning corrosion mechanisms, the steel surface condition and local inhomogeneities at the steel-
1295 concrete interface appear to have an important effect on corrosion initiation. For actively corroding
1296 rebar, the water content and the pore size distribution around the rebar are crucial parameters when
1297 determining the electrochemically active surface for corrosion reaction. The corrosion rate increases
1298 during wetting exposure until the electrochemically active surface is water-filled, and then decreases
1299 during drying exposure. The presence and distribution of corrosion products are further parameters
1300 controlling the corrosion rate, as they can diffuse away in the concrete and control the anodic
1301 reversible potential, or they can act as depolarizing agents instead of oxygen. Hence, for
1302 atmospherically exposed RC structures, it is believed that the corrosion process is under activation
1303 control. Irrespective of the depassivation mechanism, macrocell corrosion may be the main process
1304 due to local variations in environmental exposure or the presence of interconnected rebars with
1305 different properties in engineered structures. It is then required to determine the accuracy of the
1306 proposed mechanism on non-uniform corrosion to gain further insights in the corrosion of steel in RC
1307 structures.

1308 Regarding electrical methods, several techniques exist for determining corrosion potential, concrete
1309 resistivity and polarization resistance, which are used to assess the corrosion rate of steel. Despite
1310 being widely used, the half-cell potential technique must be used only to locate areas with a high
1311 corrosion risk as it does not permit a quantitative diagnosis of corrosion rate. Likewise, concrete
1312 resistivity is not directly related to the corrosion rate of steel. However, it is a good indicator of
1313 concrete durability in terms of water content and ion diffusivity. The use of electrical resistivity
1314 tomography allows to consider the inherent heterogeneity of concrete and provides more insights on
1315 transport phenomena in the material. It should then be possible to better predict both the initiation

1316 and the propagation stages for the assessment of the service life. Also, it has been shown that concrete
1317 resistivity influences the distribution of current within the concrete when performing any electrical
1318 measurement, so it is a parameter of prime importance for the determination of the corrosion rate.

1319 The polarization resistance R_p remains the most important parameter during the corrosion
1320 propagation stage as it provides quantitative information on the corrosion rate. Conventional three-
1321 electrode configuration methods require a connection to the rebar to polarize it close to its natural
1322 steady-state. Good agreement with gravimetric loss for assessing the corrosion rate is well established
1323 for actively corroding rebar in laboratory. However, for passive rebar, the accurate determination of
1324 the corrosion rate can only be guaranteed when using low scan rates ($<2.5 \text{ mV min}^{-1}$) using LPR, a long
1325 measurement time ($>100 \text{ s}$) using GP, and low frequencies ($<10^{-3} \text{ Hz}$) using EIS. For an accurate
1326 conversion of R_p into corrosion rate, the effective polarized area of the rebar must be known but its
1327 determination appears very challenging with this conventional configuration. Even if it was developed
1328 to that issue, the use of a guard ring is not recommended as it often fails to confine the current, thus
1329 compromising the measurement. Recent studies indicate that a four-electrode configuration without
1330 any connection to the rebar is suitable for indirect polarization of the rebar. This technique ensures a
1331 self-confinement of the current, which could be helpful for determining more accurately the effective
1332 polarized area. If more studies are still required for non-uniform corrosion, especially to quantify the
1333 corrosion rate, recent advances in the development of the four-electrode configuration are promising
1334 for the assessment of non-uniform corrosion. Coupling experimental measurements with finite-
1335 element simulations appears essential to predict the remaining service life of RC structures.

1336 Some perspectives can be proposed:

1337 * More studies are still required to improve our understanding on corrosion mechanisms in both
1338 small-scale and large-scale structures. Alternatives for fabricating RC structures, e.g. 3D printing,
1339 may provide a solution for reducing the heterogeneity of the material; this can help to define an
1340 optimal formulation/design of concrete and to understand better corrosion mechanisms with
1341 samples of reproducible pore size distribution and steel-concrete interface conditions.

1342 * More fundamental studies are required to convert the polarization resistance into corrosion rate,
1343 as the Stern-Geary equation—defined for uniform corrosion—generally is invalid for natural
1344 corrosion in RC structures. Currently, even with an accurate measurement of the polarization
1345 resistance, errors in the corrosion rate are to be expected with this traditional approach.

1346 * More development on indirect polarization technique for measuring the polarization resistance is
1347 required for a complete non-destructive evaluation of corrosion on RC structures. It is required to
1348 develop monitoring device that can measure the distribution of concrete resistivity and
1349 polarization resistance in the material. The development of a single device capable of providing
1350 both parameters by electrical tomography is of great interest for the assessment of the service
1351 life of RC structures.

1352 * A standard procedure for assessing the service life of existing RC structures must be defined. The
1353 objective is to accurately estimate an annual corrosion rate based on instantaneous corrosion
1354 rates. Models that consider seasonal variations of T and RH with only a few measurements should
1355 be developed. For new structures, the use of various types of embedded sensors could be
1356 envisaged for automatic measurements of the environmental factors and for developing an
1357 Internet of Things (IoT) solution.

List of symbols and abbreviations used in the text

a	Electrode spacing (m)
AC	Alternating current
B	Stern-Geary constant
C_{crit}	Critical chloride content, chloride threshold value
C_{dl}	Double layer capacitance (F)
CE	Counter electrode
CPs	Corrosion products
CPE	Constant phase element
CSE	Copper-sulphate electrode
C-S-H	Calcium silicate hydrate
DC	Direct current
E	Potential (V)
E^0	Standard potential (V)
E_{corr}	Corrosion potential (V)
EEC	Electrical equivalent circuit
EIS	Electrochemical impedance spectroscopy
ERT	Electrical resistivity tomography
f	Frequency (Hz)
F	Faraday constant (C mol ⁻¹)
GP	Galvanostatic pulse
i	Current density (A m ⁻²)
I	Current (A)
i_0	Exchange current density (A m ⁻²)
ITZ	Interfacial transition zone
k	Geometric factor (m)
LPR	Linear polarization resistance
M	Molar mass (g mol ⁻¹)
n	Number of electrons
NDT	Non-destructive testing and evaluation
OCP	Open circuit potential (V)
OPC	Ordinary Portland cement
R	Gas constant (J mol ⁻¹ K ⁻¹)
R_{Ω}	Concrete resistance (Ω)
R_p	Polarization resistance (Ω)
RE	Reference electrode
RC	Reinforced concrete
RH	Relative humidity
SCE	Saturated-calomel electrode
SHE	Standard hydrogen electrode
t	Time (s)
T	Temperature (K)
ΔV	Potential difference (V)
w/c	Water-to-cement
WE	Working electrode

X-ray μ CT	X-ray micro-computed tomography
Z	Impedance (Ω)
α_a, α_c	Anodic and cathodic charge transfer coefficients, respectively
β_a, β_c	Anodic and cathodic Tafel constants, respectively
ρ	Concrete resistivity (Ω m)
ω	Angular frequency (rad)

1359 **Conflict of interest**

1360 The authors declare no conflict of interest regarding the contents of the paper.

1361 **Acknowledgments**

1362 This study was funded by IRIS Instruments and BRGM as part of the Iris Béton project. The rebar vector
1363 design was found on Vecteezy.com. Dr H.M. Kluijver edited the English version of the manuscript.

1364 **References**

- 1365 [1] H. Van Damme, Concrete material science: Past, present, and future innovations, *Cem. Concr.*
1366 *Res.* 112 (2018) 5–24. <https://doi.org/10.1016/j.cemconres.2018.05.002>.
- 1367 [2] P. Mehta, P.J.M. Monteiro, *Concrete: Microstructure, Properties, and Materials*, Third Edition,
1368 McGraw-Hill Companies, Inc., New York, NY, USA, 2006. <https://doi.org/10.1036/0071462899>.
- 1369 [3] F. Bart, C. Cau-di-Coumes, F. Frizon, S. Lorente, *Cement-Based Materials for Nuclear Waste*
1370 *Storage*, Springer New York, New York, NY, 2013. <https://doi.org/10.1007/978-1-4614-3445-0>.
- 1371 [4] V. L’Hostis, R. Gens, *Performance Assessment of Concrete Structures and Engineered Barriers*
1372 *for Nuclear Applications*, Springer Netherlands, Dordrecht, 2016. [https://doi.org/10.1007/978-](https://doi.org/10.1007/978-94-024-0904-8)
1373 [94-024-0904-8](https://doi.org/10.1007/978-94-024-0904-8).
- 1374 [5] J.P. Broomfield, *Corrosion of Steel in Concrete: Understanding, Investigation, and Repair*, E &
1375 FN Spon, 1997.
- 1376 [6] S. Ahmad, Reinforcement corrosion in concrete structures, its monitoring and service life
1377 prediction – A review, *Cem. Concr. Compos.* 25 (2003) 459–471.
1378 [https://doi.org/10.1016/S0958-9465\(02\)00086-0](https://doi.org/10.1016/S0958-9465(02)00086-0).
- 1379 [7] L. Bertolini, B. Elsener, P. Pedferri, R.B. Polder, *Corrosion of Steel in Concrete: Prevention,*
1380 *Diagnosis, Repair*, Wiley-VCH, 2013.
- 1381 [8] A. Poursaee, *Corrosion of Steel in Concrete Structures*, Elsevier, 2016.
1382 <https://doi.org/10.1016/C2014-0-01384-6>.
- 1383 [9] R. François, S. Laurens, F. Deby, *Corrosion and its Consequences for Reinforced Concrete*
1384 *Structures*, Elsevier, 2018. <https://doi.org/10.1016/C2016-0-01228-7>.
- 1385 [10] R.B. Polder, W.H.A. Peelen, W.M.G. Courage, Non-traditional assessment and maintenance
1386 methods for aging concrete structures - technical and non-technical issues, *Mater. Corros.* 63
1387 (2012) 1147–1153. <https://doi.org/10.1002/maco.201206725>.
- 1388 [11] U.M. Angst, Challenges and opportunities in corrosion of steel in concrete, *Mater. Struct.* 51
1389 (2018) 4. <https://doi.org/10.1617/s11527-017-1131-6>.
- 1390 [12] D.M. McCann, M.C. Forde, Review of NDT methods in the assessment of concrete and masonry
1391 structures, *NDT E Int.* 34 (2001) 71–84. [https://doi.org/10.1016/S0963-8695\(00\)00032-3](https://doi.org/10.1016/S0963-8695(00)00032-3).

- 1392 [13] H.-W. Song, V. Saraswathy, Corrosion monitoring of reinforced concrete structures - A review,
1393 Int. J. Electrochem. Sci. 2 (2007) 1–28.
- 1394 [14] S.K. Verma, S.S. Bhaduria, S. Akhtar, Review of nondestructive testing methods for condition
1395 monitoring of concrete structures, J. Constr. Eng. 2013 (2013) 1–11.
1396 <https://doi.org/10.1155/2013/834572>.
- 1397 [15] A. Zaki, H.K. Chai, D.G. Aggelis, N. Alver, Non-destructive evaluation for corrosion monitoring in
1398 concrete: A review and capability of acoustic emission technique, Sensors. 15 (2015) 19069–
1399 19101. <https://doi.org/10.3390/s150819069>.
- 1400 [16] A. Poursaeed, Corrosion measurement and evaluation techniques of steel in concrete structures,
1401 in: Corros. Steel Concr. Struct., Woodhead Publishing, 2016: pp. 169–191.
1402 <https://doi.org/10.1016/B978-1-78242-381-2.00009-2>.
- 1403 [17] S. Kashif Ur Rehman, Z. Ibrahim, S.A. Memon, M. Jameel, Nondestructive test methods for
1404 concrete bridges: A review, Constr. Build. Mater. 107 (2016) 58–86.
1405 <https://doi.org/10.1016/j.conbuildmat.2015.12.011>.
- 1406 [18] D. Luo, Y. Li, J. Li, K.-S. Lim, N.A.M. Nazal, H. Ahmad, D. Luo, Y. Li, J. Li, K.-S. Lim, N.A.M. Nazal,
1407 H. Ahmad, A recent progress of steel bar corrosion diagnostic techniques in RC structures,
1408 Sensors. 19 (2018) 34. <https://doi.org/10.3390/s19010034>.
- 1409 [19] S. Taheri, A review on five key sensors for monitoring of concrete structures, Constr. Build.
1410 Mater. 204 (2019) 492–509. <https://doi.org/10.1016/j.conbuildmat.2019.01.172>.
- 1411 [20] D. Breyse, Non destructive assessment of concrete structures: usual combinations of
1412 techniques, in: Non-Destructive Assess. Concr. Struct. Reliab. Limits Single Comb. Tech.,
1413 Springer Netherlands, Dordrecht, 2012: pp. 1–16. https://doi.org/10.1007/978-94-007-2736-6_1.
- 1415 [21] J.-P. Balayssac, V. Garnier, Non-Destructive Testing and Evaluation of Civil Engineering
1416 Structures, Elsevier, 2017.
- 1417 [22] H.F.W. Taylor, Cement Chemistry, 2nd Edition, Thomas Telford, London, 1997.
- 1418 [23] B. Lothenbach, K. Scrivener, R.D. Hooton, Supplementary cementitious materials, Cem. Concr.
1419 Res. 41 (2011) 1244–1256. <https://doi.org/10.1016/j.cemconres.2010.12.001>.
- 1420 [24] M.C.G. Juenger, R. Siddique, Recent advances in understanding the role of supplementary
1421 cementitious materials in concrete, Cem. Concr. Res. 78 (2015) 71–80.
1422 <https://doi.org/10.1016/j.cemconres.2015.03.018>.
- 1423 [25] R.M. Andrew, Global CO₂ emissions from cement production, Earth Syst. Sci. Data. 10 (2018)
1424 195–217. <https://doi.org/10.5194/essd-10-195-2018>.
- 1425 [26] J.W. Bullard, H.M. Jennings, R.A. Livingston, A. Nonat, G.W. Scherer, J.S. Schweitzer, K.L.
1426 Scrivener, J.J. Thomas, Mechanisms of cement hydration, Cem. Concr. Res. 41 (2011) 1208–
1427 1223. <https://doi.org/10.1016/j.cemconres.2010.09.011>.
- 1428 [27] D. Marchon, R.J. Flatt, Mechanisms of cement hydration, Sci. Technol. Concr. Admixtures.
1429 (2016) 129–145. <https://doi.org/10.1016/B978-0-08-100693-1.00008-4>.
- 1430 [28] S. Gaboreau, D. Prêt, V. Montouillout, P. Henocq, J.-C. Robinet, C. Tournassat, Quantitative
1431 mineralogical mapping of hydrated low pH concrete, Cem. Concr. Compos. 83 (2017) 360–373.
1432 <https://doi.org/10.1016/j.cemconcomp.2017.08.003>.
- 1433 [29] ASTM_C192, Standard practice for making and curing concrete test specimens in the

- 1434 laboratory, (n.d.). <https://www.astm.org/Standards/C192> (accessed September 12, 2018).
- 1435 [30] ASTM_C31, Standard practice for making and curing concrete test specimens in the field, 2019.
1436 <https://www.astm.org/Standards/C31.htm> (accessed September 12, 2018).
- 1437 [31] R.J.-M. Pellenq, H. Van Damme, Why does concrete set?: The nature of cohesion forces in
1438 hardened cement-based materials, *MRS Bull.* 29 (2004) 319–323.
1439 <https://doi.org/10.1557/mrs2004.97>.
- 1440 [32] R.J.-M. Pellenq, N. Lequeux, H. Van Damme, Engineering the bonding scheme in C–S–H: The
1441 ionic-covalent framework, *Cem. Concr. Res.* 38 (2008) 159–174.
1442 <https://doi.org/10.1016/j.cemconres.2007.09.026>.
- 1443 [33] H. Manzano, S. Moeini, F. Marinelli, A.C.T. van Duin, F.-J. Ulm, R.J.-M. Pellenq, Confined water
1444 dissociation in microporous defective silicates: Mechanism, dipole distribution, and impact on
1445 substrate properties, *J. Am. Chem. Soc.* 134 (2012) 2208–2215.
1446 <https://doi.org/10.1021/ja209152n>.
- 1447 [34] P.A. Bonnaud, Q. Ji, B. Coasne, R.J.-M. Pellenq, K.J. Van Vliet, Thermodynamics of water
1448 confined in porous calcium-silicate-hydrates, *Langmuir.* 28 (2012) 11422–11432.
1449 <https://doi.org/10.1021/la301738p>.
- 1450 [35] P.A. Bonnaud, Q. Ji, K.J. Van Vliet, Effects of elevated temperature on the structure and
1451 properties of calcium–silicate–hydrate gels: the role of confined water, *Soft Matter.* 9 (2013)
1452 6418. <https://doi.org/10.1039/c3sm50975c>.
- 1453 [36] P. Blanc, X. Bourbon, A. Lassin, E.C. Gaucher, Chemical model for cement-based materials:
1454 Temperature dependence of thermodynamic functions for nanocrystalline and crystalline C–S–
1455 H phases, *Cem. Concr. Res.* 40 (2010) 851–866.
1456 <https://doi.org/10.1016/j.cemconres.2009.12.004>.
- 1457 [37] P. Blanc, X. Bourbon, A. Lassin, E.C. Gaucher, Chemical model for cement-based materials:
1458 Thermodynamic data assessment for phases other than C–S–H, *Cem. Concr. Res.* 40 (2010)
1459 1360–1374. <https://doi.org/10.1016/j.cemconres.2010.04.003>.
- 1460 [38] C. Roosz, S. Gaboreau, S. Grangeon, D. Prêt, V. Montouillout, N. Maubec, S. Ory, P. Blanc, P.
1461 Vieillard, P. Henocq, Distribution of water in synthetic calcium silicate hydrates, *Langmuir.* 32
1462 (2016) 6794–6805. <https://doi.org/10.1021/acs.langmuir.6b00878>.
- 1463 [39] C. Roosz, P. Vieillard, P. Blanc, S. Gaboreau, H. Gailhanou, D. Braithwaite, V. Montouillout, R.
1464 Denoyel, P. Henocq, B. Madé, Thermodynamic properties of C-S-H, C-A-S-H and M-S-H phases:
1465 Results from direct measurements and predictive modelling, *Appl. Geochemistry.* 92 (2018)
1466 140–156. <https://doi.org/10.1016/j.apgeochem.2018.03.004>.
- 1467 [40] B. Lothenbach, M. Zajac, Application of thermodynamic modelling to hydrated cements, *Cem.*
1468 *Concr. Res.* 123 (2019) 105779. <https://doi.org/10.1016/j.cemconres.2019.105779>.
- 1469 [41] S. Gaboreau, S. Grangeon, F. Claret, D. Ihiawakrim, O. Ersen, V. Montouillout, N. Maubec, C.
1470 Roosz, P. Henocq, C. Carteret, Hydration properties and interlayer organization in synthetic C-
1471 S-H, *Langmuir.* 36 (2020) 9449–9464. <https://doi.org/10.1021/acs.langmuir.0c01335>.
- 1472 [42] B. Lothenbach, A. Nonat, Calcium silicate hydrates: Solid and liquid phase composition, *Cem.*
1473 *Concr. Res.* 78 (2015) 57–70. <https://doi.org/10.1016/j.cemconres.2015.03.019>.
- 1474 [43] C.S. Walker, S. Sutou, C. Oda, M. Mihara, A. Honda, Calcium silicate hydrate (C-S-H) gel solubility
1475 data and a discrete solid phase model at 25 °C based on two binary non-ideal solid solutions,
1476 *Cem. Concr. Res.* 79 (2016) 1–30. <https://doi.org/10.1016/j.cemconres.2015.07.006>.

- 1477 [44] G.M.N. Baston, A.P. Clacher, T.G. Heath, F.M.I. Hunter, V. Smith, S.W. Swanton, Calcium silicate
1478 hydrate (C-S-H) gel dissolution and pH buffering in a cementitious near field, *Mineral. Mag.* 76
1479 (2012) 3045–3053. <https://doi.org/10.1180/minmag.2012.076.8.20>.
- 1480 [45] H.W. Whittington, J. McCarter, M.C. Forde, The conduction of electricity through concrete,
1481 *Mag. Concr. Res.* 33 (1981) 48–60. <https://doi.org/10.1680/mac.1981.33.114.48>.
- 1482 [46] R.A. Patel, Q.T. Phung, S.C. Seetharam, J. Perko, D. Jacques, N. Maes, G. De Schutter, G. Ye, K.
1483 Van Breugel, Diffusivity of saturated ordinary Portland cement-based materials: A critical
1484 review of experimental and analytical modelling approaches, *Cem. Concr. Res.* 90 (2016) 52–
1485 72. <https://doi.org/10.1016/j.cemconres.2016.09.015>.
- 1486 [47] M. Parisatto, M.C. Dalconi, L. Valentini, G. Artioli, A. Rack, R. Tucoulou, G. Cruciani, G. Ferrari,
1487 Examining microstructural evolution of Portland cements by in-situ synchrotron micro-
1488 tomography, *J. Mater. Sci.* 50 (2015) 1805–1817. <https://doi.org/10.1007/s10853-014-8743-9>.
- 1489 [48] M. Moradian, Q. Hu, M. Aboustait, M.T. Ley, J.C. Hanan, X. Xiao, G.W. Scherer, Z. Zhang, Direct
1490 observation of void evolution during cement hydration, *Mater. Des.* 136 (2017) 137–149.
1491 <https://doi.org/10.1016/j.matdes.2017.09.056>.
- 1492 [49] Z. Zhang, G.W. Scherer, A. Bauer, Morphology of cementitious material during early hydration,
1493 *Cem. Concr. Res.* 107 (2018) 85–100. <https://doi.org/10.1016/j.cemconres.2018.02.004>.
- 1494 [50] A. Elsharief, M.D. Cohen, J. Olek, Influence of aggregate size, water cement ratio and age on
1495 the microstructure of the interfacial transition zone, *Cem. Concr. Res.* 33 (2003) 1837–1849.
1496 [https://doi.org/10.1016/S0008-8846\(03\)00205-9](https://doi.org/10.1016/S0008-8846(03)00205-9).
- 1497 [51] Z. Zhang, U. Angst, A discussion of the paper “Effect of design parameters on microstructure of
1498 steel-concrete interface in reinforced concrete,” *Cem. Concr. Res.* 128 (2020) 105949.
1499 <https://doi.org/10.1016/j.cemconres.2019.105949>.
- 1500 [52] A.B. Abell, K.L. Willis, D.A. Lange, Mercury intrusion porosimetry and image analysis of cement-
1501 based materials, *J. Colloid Interface Sci.* 211 (1999) 39–44.
1502 <https://doi.org/10.1006/jcis.1998.5986>.
- 1503 [53] S. Diamond, The microstructure of cement paste and concrete—a visual primer, *Cem. Concr.*
1504 *Compos.* 26 (2004) 919–933. <https://doi.org/10.1016/j.cemconcomp.2004.02.028>.
- 1505 [54] K.L. Scrivener, Backscattered electron imaging of cementitious microstructures: understanding
1506 and quantification, *Cem. Concr. Compos.* 26 (2004) 935–945.
1507 <https://doi.org/10.1016/j.cemconcomp.2004.02.029>.
- 1508 [55] H.S. Wong, M.K. Head, N.R. Buenfeld, Pore segmentation of cement-based materials from
1509 backscattered electron images, *Cem. Concr. Res.* 36 (2006) 1083–1090.
1510 <https://doi.org/10.1016/j.cemconres.2005.10.006>.
- 1511 [56] S.-Y. Chung, J.-S. Kim, D. Stephan, T.-S. Han, Overview of the use of micro-computed
1512 tomography (micro-CT) to investigate the relation between the material characteristics and
1513 properties of cement-based materials, *Constr. Build. Mater.* 229 (2019) 116843.
1514 <https://doi.org/10.1016/j.conbuildmat.2019.116843>.
- 1515 [57] S. Brisard, M. Serdar, P.J.M. Monteiro, Multiscale X-ray tomography of cementitious materials:
1516 A review, *Cem. Concr. Res.* 128 (2020) 105824.
1517 <https://doi.org/10.1016/j.cemconres.2019.105824>.
- 1518 [58] P. Leroy, A. Hördt, S. Gaboreau, E. Zimmermann, F. Claret, M. Bücker, H. Stebner, J.A. Huisman,
1519 Spectral induced polarization of low-pH cement and concrete, *Cem. Concr. Compos.* 104 (2019)

- 1520 103397. <https://doi.org/10.1016/j.cemconcomp.2019.103397>.
- 1521 [59] D. Clover, B. Kinsella, B. Pejic, R. De Marco, The influence of microstructure on the corrosion
1522 rate of various carbon steels, *J. Appl. Electrochem.* 35 (2005) 139–149.
1523 <https://doi.org/10.1007/s10800-004-6207-7>.
- 1524 [60] R.R. Hussain, J.K. Singh, A. Alhozaimy, A. Al-Negheimish, C. Bhattacharya, R.S. Pathania, D.D.N.
1525 Singh, Effect of reinforcing bar microstructure on passive film exposed to simulated concrete
1526 pore solution, *ACI Mater. J.* 115 (2018) 181–190. <https://doi.org/10.14359/51701237>.
- 1527 [61] P.K. Katiyar, P.K. Behera, S. Misra, K. Mondal, Comparative corrosion behavior of five different
1528 microstructures of rebar steels in simulated concrete pore solution with and without chloride
1529 addition, *J. Mater. Eng. Perform.* 28 (2019) 6275–6286. <https://doi.org/10.1007/s11665-019-04339-x>.
1530
- 1531 [62] H. Torbati-Sarraf, A. Poursae, The influence of phase distribution and microstructure of the
1532 carbon steel on its chloride threshold value in a simulated concrete pore solution, *Constr. Build.
1533 Mater.* 259 (2020) 119784. <https://doi.org/10.1016/j.conbuildmat.2020.119784>.
- 1534 [63] U.M. Angst, M.R. Geiker, A. Michel, C. Gehlen, H. Wong, O.B. Isgor, B. Elsener, C.M. Hansson,
1535 R. François, K. Hornbostel, R. Polder, M.C. Alonso, M. Sanchez, M.J. Correia, M. Criado, A.
1536 Sagüés, N. Buenfeld, The steel–concrete interface, *Mater. Struct.* 50 (2017) 143.
1537 <https://doi.org/10.1617/s11527-017-1010-1>.
- 1538 [64] P. Ghods, O.B. Isgor, G.A. McRae, J. Li, G.P. Gu, Microscopic investigation of mill scale and its
1539 proposed effect on the variability of chloride-induced depassivation of carbon steel rebar,
1540 *Corros. Sci.* 53 (2011) 946–954. <https://doi.org/10.1016/j.corsci.2010.11.025>.
- 1541 [65] L. Tang, J.M. Frederiksen, U.M. Angst, R. Polder, M.C. Alonso, B. Elsener, D. Hooton, J. Pacheco,
1542 Experiences from RILEM TC 235-CTC in recommending a test method for chloride threshold
1543 values in concrete, *RILEM Tech. Lett.* 3 (2018) 25–31.
1544 <https://doi.org/10.21809/rilemtechlett.2018.55>.
- 1545 [66] L. Ding, H. Torbati-Sarraf, A. Poursae, The influence of the sandblasting as a surface mechanical
1546 attrition treatment on the electrochemical behavior of carbon steel in different pH solutions,
1547 *Surf. Coatings Technol.* 352 (2018) 112–119. <https://doi.org/10.1016/j.surfcoat.2018.08.013>.
- 1548 [67] L.T. Mammoliti, L.C. Brown, C.M. Hansson, B.B. Hope, The influence of surface finish of
1549 reinforcing steel and pH of the test solution on the chloride threshold concentration for
1550 corrosion initiation in synthetic pore solutions, *Cem. Concr. Res.* 26 (1996) 545–550.
1551 [https://doi.org/10.1016/0008-8846\(96\)00018-X](https://doi.org/10.1016/0008-8846(96)00018-X).
- 1552 [68] H. Tamura, The role of rusts in corrosion and corrosion protection of iron and steel, *Corros. Sci.*
1553 50 (2008) 1872–1883. <https://doi.org/10.1016/j.corsci.2008.03.008>.
- 1554 [69] J. Ming, J. Shi, W. Sun, Effect of mill scale on the long-term corrosion resistance of a low-alloy
1555 reinforcing steel in concrete subjected to chloride solution, *Constr. Build. Mater.* 163 (2018)
1556 508–517. <https://doi.org/10.1016/j.conbuildmat.2017.12.125>.
- 1557 [70] A.J. Al-Tayyib, M.S. Khan, I.M. Allam, A.I. Al-Mana, Corrosion behavior of pre-rusted rebars after
1558 placement in concrete, *Cem. Concr. Res.* 20 (1990) 955–960. [https://doi.org/10.1016/0008-8846\(90\)90059-7](https://doi.org/10.1016/0008-8846(90)90059-7).
1559
- 1560 [71] C. Hansson, B. Sofensen, The threshold concentration of chloride in concrete for the initiation
1561 of reinforcement corrosion, in: *Corros. Rates Steel Concr.*, ASTM International, 100 Barr Harbor
1562 Drive, PO Box C700, West Conshohocken, PA 19428-2959, 1990: pp. 3–14.
1563 <https://doi.org/10.1520/STP25011S>.

- 1564 [72] P. Novak, R. Mala, L. Joska, Influence of pre-rusting on steel corrosion in concrete, *Cem. Concr. Res.* 31 (2001) 589–593. [https://doi.org/10.1016/S0008-8846\(01\)00459-8](https://doi.org/10.1016/S0008-8846(01)00459-8).
1565
- 1566 [73] E. Mahallati, M. Saremi, An assessment on the mill scale effects on the electrochemical characteristics of steel bars in concrete under DC-polarization, *Cem. Concr. Res.* 36 (2006) 1324–1329. <https://doi.org/10.1016/j.cemconres.2006.03.015>.
1567
1568
- 1569 [74] T.U. Mohammed, H. Hamada, Corrosion of steel bars in concrete with various steel surface conditions, *ACI Mater. J.* 103 (2006) 233–242. <https://doi.org/10.14359/16606>.
1570
- 1571 [75] D. Boubitsas, L. Tang, The influence of reinforcement steel surface condition on initiation of chloride induced corrosion, *Mater. Struct.* 48 (2015) 2641–2658. <https://doi.org/10.1617/s11527-014-0343-2>.
1572
1573
- 1574 [76] J.A. González, E. Ramírez, A. Bautista, S. Feliu, The behaviour of pre-rusted steel in concrete, *Cem. Concr. Res.* 26 (1996) 501–511. [https://doi.org/10.1016/S0008-8846\(96\)85037-X](https://doi.org/10.1016/S0008-8846(96)85037-X).
1575
- 1576 [77] C. Chalhoub, R. François, M. Carcasses, Critical chloride threshold values as a function of cement type and steel surface condition, *Cem. Concr. Res.* 134 (2020) 106086. <https://doi.org/10.1016/j.cemconres.2020.106086>.
1577
1578
- 1579 [78] M.J. Martinez-Echevarria, M. Lopez-Alonso, D. Cantero Romero, J. Rodríguez Montero, Influence of the previous state of corrosion of rebars in predicting the service life of reinforced concrete structures, *Constr. Build. Mater.* 188 (2018) 915–923. <https://doi.org/10.1016/j.conbuildmat.2018.08.173>.
1580
1581
1582
- 1583 [79] L. Michel, U. Angst, Towards understanding corrosion initiation in concrete – Influence of local electrochemical properties of reinforcing steel, *MATEC Web Conf.* 199 (2018) 04001. <https://doi.org/10.1051/mateconf/201819904001>.
1584
1585
- 1586 [80] U.M. Angst, M.R. Geiker, M.C. Alonso, R. Polder, O.B. Isgor, B. Elsener, H. Wong, A. Michel, K. Hornbostel, C. Gehlen, R. François, M. Sanchez, M. Criado, H. Sørensen, C. Hansson, R. Pillai, S. Mundra, J. Gulikers, M. Raupach, J. Pacheco, A. Sagüés, The effect of the steel–concrete interface on chloride-induced corrosion initiation in concrete: a critical review by RILEM TC 262-SCI, *Mater. Struct.* 52 (2019) 88. <https://doi.org/10.1617/s11527-019-1387-0>.
1587
1588
1589
1590
- 1591 [81] X.R. Nóvoa, Electrochemical aspects of the steel-concrete system. A review, *J. Solid State Electrochem.* 20 (2016) 2113–2125. <https://doi.org/10.1007/s10008-016-3238-z>.
1592
- 1593 [82] S. Joiret, M. Keddad, X.R. Nóvoa, M.C. Pérez, C. Rangel, H. Takenouti, Use of EIS, ring-disk electrode, EQCM and Raman spectroscopy to study the film of oxides formed on iron in 1 M NaOH, *Cem. Concr. Compos.* 24 (2002) 7–15. [https://doi.org/10.1016/S0958-9465\(01\)00022-1](https://doi.org/10.1016/S0958-9465(01)00022-1).
1594
1595
- 1596 [83] A. Poursaee, C.M. Hansson, Reinforcing steel passivation in mortar and pore solution, *Cem. Concr. Res.* 37 (2007) 1127–1133. <https://doi.org/10.1016/j.cemconres.2007.04.005>.
1597
- 1598 [84] S.M. Abd El Haleem, E.E. Abd El Aal, S. Abd El Wanees, A. Diab, Environmental factors affecting the corrosion behaviour of reinforcing steel: I. The early stage of passive film formation in Ca(OH)₂ solutions, *Corros. Sci.* 52 (2010) 3875–3882. <https://doi.org/10.1016/j.corsci.2010.07.035>.
1599
1600
1601
- 1602 [85] H. DorMohammadi, Q. Pang, P. Murkute, L. Arnadottir, O. Burkan Isgor, Investigation of iron passivity in highly alkaline media using reactive-force field molecular dynamics, *Corros. Sci.* (2019). <https://doi.org/10.1016/j.corsci.2019.05.016>.
1603
1604
- 1605 [86] E. Volpi, A. Olietti, M. Stefanoni, S.P. Trasatti, Electrochemical characterization of mild steel in alkaline solutions simulating concrete environment, *J. Electroanal. Chem.* 736 (2015) 38–46.
1606

- 1607 <https://doi.org/10.1016/j.jelechem.2014.10.023>.
- 1608 [87] B. Elsener, A. Rossi, Passivation of steel and stainless steel in alkaline media simulating concrete,
1609 in: *Encycl. Interfacial Chem.*, Elsevier, 2018: pp. 365–375. [https://doi.org/10.1016/B978-0-12-](https://doi.org/10.1016/B978-0-12-409547-2.13772-2)
1610 [409547-2.13772-2](https://doi.org/10.1016/B978-0-12-409547-2.13772-2).
- 1611 [88] C. Andrade, P. Merino, X.R. Nóvoa, M.C. Pérez, L. Soler, Passivation of reinforcing steel in
1612 concrete, *Mater. Sci. Forum.* 192–194 (1995) 891–898.
1613 <https://doi.org/10.4028/www.scientific.net/MSF.192-194.891>.
- 1614 [89] X.R. Nóvoa, M.C. Pérez, On the role of iron oxides in the electrochemical behaviour of steel
1615 embedded in concrete, *Corros. Rev.* 23 (2005) 195–216.
1616 <https://doi.org/10.1515/correv.2005.23.2-3.195>.
- 1617 [90] M. Sánchez, J. Gregori, C. Alonso, J.J. García-Jareño, H. Takenouti, F. Vicente, Electrochemical
1618 impedance spectroscopy for studying passive layers on steel rebars immersed in alkaline
1619 solutions simulating concrete pores, *Electrochim. Acta.* 52 (2007) 7634–7641.
1620 <https://doi.org/10.1016/j.electacta.2007.02.012>.
- 1621 [91] J. Williamson, O.B. Isgor, The effect of simulated concrete pore solution composition and
1622 chlorides on the electronic properties of passive films on carbon steel rebar, *Corros. Sci.* 106
1623 (2016) 82–95. <https://doi.org/10.1016/j.corsci.2016.01.027>.
- 1624 [92] A. Poursaei, Corrosion of steel in concrete structures, in: *Corros. Steel Concr. Struct.*,
1625 Woodhead Publishing, 2016: pp. 19–33. [https://doi.org/10.1016/B978-1-78242-381-2.00002-](https://doi.org/10.1016/B978-1-78242-381-2.00002-X)
1626 [X](https://doi.org/10.1016/B978-1-78242-381-2.00002-X).
- 1627 [93] H.B. Gunay, O.B. Isgor, P. Ghods, Kinetics of passivation and chloride-induced depassivation of
1628 iron in simulated concrete pore solutions using electrochemical quartz crystal nanobalance,
1629 *Corrosion.* 71 (2015) 615–627. <https://doi.org/10.5006/1346>.
- 1630 [94] M.F. Montemor, A.M.P. Simões, M.G.S. Ferreira, Analytical characterization of the passive film
1631 formed on steel in solutions simulating the concrete interstitial electrolyte, *Corrosion.* 54 (1998)
1632 347–353. <https://doi.org/10.5006/1.3284861>.
- 1633 [95] P. Ghods, O.B. Isgor, G. McRae, T. Miller, The effect of concrete pore solution composition on
1634 the quality of passive oxide films on black steel reinforcement, *Cem. Concr. Compos.* 31 (2009)
1635 2–11. <https://doi.org/10.1016/j.cemconcomp.2008.10.003>.
- 1636 [96] A.T. Horne, I.G. Richardson, R.M.D. Brydson, Quantitative analysis of the microstructure of
1637 interfaces in steel reinforced concrete, *Cem. Concr. Res.* 37 (2007) 1613–1623.
1638 <https://doi.org/10.1016/j.cemconres.2007.08.026>.
- 1639 [97] A. Kenny, A. Katz, Statistical relationship between mix properties and the interfacial transition
1640 zone around embedded rebar, *Cem. Concr. Compos.* 60 (2015) 82–91.
1641 <https://doi.org/10.1016/j.cemconcomp.2015.04.002>.
- 1642 [98] Y. Cai, W. Zhang, L. Yu, M. Chen, C. Yang, R. François, K. Yang, Characteristics of the steel-
1643 concrete interface and their effect on the corrosion of steel bars in concrete, *Constr. Build.*
1644 *Mater.* 253 (2020) 119162. <https://doi.org/10.1016/j.conbuildmat.2020.119162>.
- 1645 [99] T.A. Soylev, R. François, Quality of steel–concrete interface and corrosion of reinforcing steel,
1646 *Cem. Concr. Res.* 33 (2003) 1407–1415. [https://doi.org/10.1016/S0008-8846\(03\)00087-5](https://doi.org/10.1016/S0008-8846(03)00087-5).
- 1647 [100] G.K. Glass, R. Yang, T. Dickhaus, N.R. Buenfeld, Backscattered electron imaging of the steel–
1648 concrete interface, *Corros. Sci.* 43 (2001) 605–610. [https://doi.org/10.1016/S0010-](https://doi.org/10.1016/S0010-938X(00)00146-3)
1649 [938X\(00\)00146-3](https://doi.org/10.1016/S0010-938X(00)00146-3).

- 1650 [101] F. Chen, C.-Q. Li, H. Baji, B. Ma, Quantification of steel-concrete interface in reinforced concrete
 1651 using backscattered electron imaging technique, *Constr. Build. Mater.* 179 (2018) 420–429.
 1652 <https://doi.org/10.1016/j.conbuildmat.2018.05.246>.
- 1653 [102] S.K. Goudar, B.B. Das, S.B. Arya, K.N. Shivaprasad, Influence of sample preparation techniques
 1654 on microstructure and nano-mechanical properties of steel-concrete interface, *Constr. Build.*
 1655 *Mater.* 256 (2020) 119242. <https://doi.org/10.1016/j.conbuildmat.2020.119242>.
- 1656 [103] Z. Zhang, M. Shakoorioskooie, M. Griffa, P. Lura, U. Angst, A laboratory investigation of cutting
 1657 damage to the steel-concrete interface, *Cem. Concr. Res.* 138 (2020) 106229.
 1658 <https://doi.org/10.1016/j.cemconres.2020.106229>.
- 1659 [104] K. Tuutti, *Corrosion of Steel in Concrete*, Swedish Cement and Concrete Research Institute,
 1660 Stockholm, 1982.
- 1661 [105] C. Andrade, C. Alonso, J. Gulikers, R. Polder, R. Cigna, Ø. Vennesland, M. Salta, A. Raharinaivo,
 1662 B. Elsener, Test methods for on-site corrosion rate measurement of steel reinforcement in
 1663 concrete by means of the polarization resistance method, *Mater. Struct.* 37 (2004) 623–642.
 1664 <https://doi.org/10.1007/BF02483292>.
- 1665 [106] C. Qing Li, Reliability based service life prediction of corrosion affected concrete structures, *J.*
 1666 *Struct. Eng.* 130 (2004) 1570–1577. [https://doi.org/10.1061/\(ASCE\)0733-](https://doi.org/10.1061/(ASCE)0733-9445(2004)130:10(1570))
 1667 [9445\(2004\)130:10\(1570\)](https://doi.org/10.1061/(ASCE)0733-9445(2004)130:10(1570)).
- 1668 [107] M. Raupach, Models for the propagation phase of reinforcement corrosion – an overview,
 1669 *Mater. Corros.* 57 (2006) 605–613. <https://doi.org/10.1002/maco.200603991>.
- 1670 [108] M.B. Otieno, H.D. Beushausen, M.G. Alexander, Modelling corrosion propagation in reinforced
 1671 concrete structures – A critical review, *Cem. Concr. Compos.* 33 (2011) 240–245.
 1672 <https://doi.org/10.1016/j.cemconcomp.2010.11.002>.
- 1673 [109] D. Chen, S. Mahadevan, Chloride-induced reinforcement corrosion and concrete cracking
 1674 simulation, *Cem. Concr. Compos.* 30 (2008) 227–238.
 1675 <https://doi.org/10.1016/j.cemconcomp.2006.10.007>.
- 1676 [110] F. Chen, H. Baji, C.-Q. Li, A comparative study on factors affecting time to cover cracking as a
 1677 service life indicator, *Constr. Build. Mater.* 163 (2018) 681–694.
 1678 <https://doi.org/10.1016/j.conbuildmat.2017.12.120>.
- 1679 [111] M. Alexander, H. Beushausen, Durability, service life prediction, and modelling for reinforced
 1680 concrete structures – review and critique, *Cem. Concr. Res.* 122 (2019) 17–29.
 1681 <https://doi.org/10.1016/j.cemconres.2019.04.018>.
- 1682 [112] O.B. Isgor, A.G. Razaqpur, Modelling steel corrosion in concrete structures, *Mater. Struct.* 39
 1683 (2006) 291–302. <https://doi.org/10.1007/s11527-005-9022-7>.
- 1684 [113] Z.M. Mir, D. Höche, C. Gomes, R. Sampaio, A.C. Bastos, P. Maincon, M.G.S. Ferreira, M.L.
 1685 Zheludkevich, Enhanced predictive modelling of steel corrosion in concrete in submerged zone
 1686 based on a dynamic activation approach, *Int. J. Concr. Struct. Mater.* 13 (2019) 11.
 1687 <https://doi.org/10.1186/s40069-018-0321-0>.
- 1688 [114] O.A. Kayyali, M.N. Haque, Effect of carbonation on the chloride concentration in pore solution
 1689 of mortars with and without flyash, *Cem. Concr. Res.* 18 (1988) 636–648.
 1690 [https://doi.org/10.1016/0008-8846\(88\)90056-7](https://doi.org/10.1016/0008-8846(88)90056-7).
- 1691 [115] X. Zhu, G. Zi, Z. Cao, X. Cheng, Combined effect of carbonation and chloride ingress in concrete,
 1692 *Constr. Build. Mater.* 110 (2016) 369–380. <https://doi.org/10.1016/j.conbuildmat.2016.02.034>.

- 1693 [116] J. Geng, D. Easterbrook, Q.-F. Liu, L.-Y. Li, Effect of carbonation on release of bound chlorides in
1694 chloride-contaminated concrete, *Mag. Concr. Res.* 68 (2016) 353–363.
1695 <https://doi.org/10.1680/jmacr.15.00234>.
- 1696 [117] J.A. Gonzalez, J.S. Algaba, C. Andrade, Corrosion of reinforcing bars in carbonated concrete, *Br.*
1697 *Corros. J.* 15 (1980) 135–139. <https://doi.org/10.1179/bcj.1980.15.3.135>.
- 1698 [118] C. Alonso, C. Andrade, Corrosion of steel reinforcement in carbonated mortar containing
1699 chlorides, *Adv. Cem. Res.* 1 (1988) 155–163. <https://doi.org/10.1680/1988.1.3.155>.
- 1700 [119] D.A. Hausmann, Steel corrosion in concrete. How does it occur?, *J. Mater. Prot.* 6 (1967) 19–23.
- 1701 [120] M. Stratmann, J. Müller, The mechanism of the oxygen reduction on rust-covered metal
1702 substrates, *Corros. Sci.* 36 (1994) 327–359. [https://doi.org/10.1016/0010-938X\(94\)90161-9](https://doi.org/10.1016/0010-938X(94)90161-9).
- 1703 [121] C.M. Hansson, Comments on electrochemical measurements of the rate of corrosion of steel in
1704 concrete, *Cem. Concr. Res.* 14 (1984) 574–584. [https://doi.org/10.1016/0008-8846\(84\)90135-](https://doi.org/10.1016/0008-8846(84)90135-2)
1705 [2](https://doi.org/10.1016/0008-8846(84)90135-2).
- 1706 [122] M. Pourbaix, Thermodynamics and corrosion, *Corros. Sci.* 30 (1990) 963–988.
1707 [https://doi.org/10.1016/0010-938X\(90\)90205-J](https://doi.org/10.1016/0010-938X(90)90205-J).
- 1708 [123] R. François, S. Laurens, F. Deby, Steel Corrosion in Reinforced Concrete, in: *Corros. Its*
1709 *Consequences Reinf. Concr. Struct.*, Elsevier, 2018: pp. 1–41. [https://doi.org/10.1016/B978-1-](https://doi.org/10.1016/B978-1-78548-234-2.50001-9)
1710 [78548-234-2.50001-9](https://doi.org/10.1016/B978-1-78548-234-2.50001-9).
- 1711 [124] M. Stefanoni, U.M. Angst, B. Elsener, Electrochemistry and capillary condensation theory reveal
1712 the mechanism of corrosion in dense porous media, *Sci. Rep.* 8 (2018) 7407.
1713 <https://doi.org/10.1038/s41598-018-25794-x>.
- 1714 [125] M. Stefanoni, U.M. Angst, B. Elsener, Kinetics of electrochemical dissolution of metals in porous
1715 media, *Nat. Mater.* 18 (2019) 942–947. <https://doi.org/10.1038/s41563-019-0439-8>.
- 1716 [126] M. Pour-Ghaz, O. Burkan Isgor, P. Ghods, The effect of temperature on the corrosion of steel in
1717 concrete. Part 1: Simulated polarization resistance tests and model development, *Corros. Sci.*
1718 51 (2009) 415–425. <https://doi.org/10.1016/j.corsci.2008.10.034>.
- 1719 [127] M. Pour-Ghaz, O. Burkan Isgor, P. Ghods, The effect of temperature on the corrosion of steel in
1720 concrete. Part 2: Model verification and parametric study, *Corros. Sci.* 51 (2009) 426–433.
1721 <https://doi.org/10.1016/j.corsci.2008.10.036>.
- 1722 [128] E. Rossi, R. Polder, O. Copuroglu, T. Nijland, B. Šavija, The influence of defects at the
1723 steel/concrete interface for chloride-induced pitting corrosion of naturally-deteriorated 20-
1724 years-old specimens studied through X-ray Computed Tomography, *Constr. Build. Mater.* 235
1725 (2020) 117474. <https://doi.org/10.1016/j.conbuildmat.2019.117474>.
- 1726 [129] B. Huet, V. L’Hostis, G. Santarini, D. Feron, H. Idrissi, Steel corrosion in concrete: Determinist
1727 modeling of cathodic reaction as a function of water saturation degree, *Corros. Sci.* 49 (2007)
1728 1918–1932. <https://doi.org/10.1016/j.corsci.2006.10.005>.
- 1729 [130] C. Cao, M.M.S. Cheung, B.Y.B. Chan, Modelling of interaction between corrosion-induced
1730 concrete cover crack and steel corrosion rate, *Corros. Sci.* 69 (2013) 97–109.
1731 <https://doi.org/10.1016/j.corsci.2012.11.028>.
- 1732 [131] Y. Zhao, W. Jin, Steel Corrosion in Concrete, in: *Steel Corros. Concr. Crack.*, Butterworth-
1733 Heinemann, 2016: pp. 19–29. <https://doi.org/10.1016/B978-0-12-809197-5.00002-5>.
- 1734 [132] M. Stefanoni, Z. Zhang, U. Angst, B. Elsener, The kinetic competition between transport and

- 1735 oxidation of ferrous ions governs precipitation of corrosion products in carbonated concrete,
1736 RILEM Tech. Lett. 3 (2018) 8–16. <https://doi.org/10.21809/rilemtechlett.2018.57>.
- 1737 [133] P. Blanc, A. Lassin, P. Piantone, M. Azaroual, N. Jacquemet, A. Fabbri, E.C. Gaucher,
1738 Thermodem: A geochemical database focused on low temperature water/rock interactions
1739 and waste materials, *Appl. Geochemistry*. 27 (2012) 2107–2116.
1740 <https://doi.org/10.1016/j.apgeochem.2012.06.002>.
- 1741 [134] B. Šavija, M. Luković, Carbonation of cement paste: Understanding, challenges, and
1742 opportunities, *Constr. Build. Mater.* 117 (2016) 285–301.
1743 <https://doi.org/10.1016/j.conbuildmat.2016.04.138>.
- 1744 [135] V.G. Papadakis, C.G. Vayenas, M.N. Fardis, Fundamental modeling and experimental
1745 investigation of concrete carbonation, *ACI Mater. J.* 88 (1991) 363–373.
1746 <https://doi.org/10.14359/1863>.
- 1747 [136] V.G. Papadakis, C.G. Vayenas, M.N. Fardis, Physical and chemical characteristics affecting the
1748 durability of concrete, *ACI Mater. J.* 88 (1991) 186–196. <https://doi.org/10.14359/1993>.
- 1749 [137] Y.F. Houst, F.H. Wittmann, Influence of porosity and water content on the diffusivity of CO₂ and
1750 O₂ through hydrated cement paste, *Cem. Concr. Res.* 24 (1994) 1165–1176.
1751 [https://doi.org/10.1016/0008-8846\(94\)90040-X](https://doi.org/10.1016/0008-8846(94)90040-X).
- 1752 [138] P. Castro, M.A. Sanjuán, J. Genescá, Carbonation of concretes in the Mexican Gulf, *Build.*
1753 *Environ.* 35 (2000) 145–149. [https://doi.org/10.1016/S0360-1323\(99\)00009-8](https://doi.org/10.1016/S0360-1323(99)00009-8).
- 1754 [139] J.H.M. Visser, Influence of the carbon dioxide concentration on the resistance to carbonation
1755 of concrete, *Constr. Build. Mater.* 67 (2014) 8–13.
1756 <https://doi.org/10.1016/j.conbuildmat.2013.11.005>.
- 1757 [140] A. Morandea, M. Thiéry, P. Dangla, Investigation of the carbonation mechanism of CH and C-
1758 S-H in terms of kinetics, microstructure changes and moisture properties, *Cem. Concr. Res.* 56
1759 (2014) 153–170. <https://doi.org/10.1016/j.cemconres.2013.11.015>.
- 1760 [141] I. Galan, C. Andrade, M. Castellote, Natural and accelerated CO₂ binding kinetics in cement
1761 paste at different relative humidities, *Cem. Concr. Res.* 49 (2013) 21–28.
1762 <https://doi.org/10.1016/j.cemconres.2013.03.009>.
- 1763 [142] Q. Huy Vu, G. Pham, A. Chonier, E. Brouard, S. Rathnarajan, R. Pillai, R. Gettu, M. Santhanam, F.
1764 Aguayo, K.J. Folliard, M.D. Thomas, T. Moffat, C. Shi, A. Sarnot, Impact of different climates on
1765 the resistance of concrete to natural carbonation, *Constr. Build. Mater.* 216 (2019) 450–467.
1766 <https://doi.org/10.1016/j.conbuildmat.2019.04.263>.
- 1767 [143] S.K. Roy, P.K. Beng, D.O. Northwood, The carbonation of concrete structures in the tropical
1768 environment of singapore and a comparison with published data for temperate climates, *Mag.*
1769 *Concr. Res.* 48 (1996) 293–300. <https://doi.org/10.1680/mac.1996.48.177.293>.
- 1770 [144] M.N. Haque, H. Al-Khaiat, Carbonation of concrete structures in hot dry coastal regions, *Cem.*
1771 *Concr. Compos.* 19 (1997) 123–129. [https://doi.org/10.1016/s0958-9465\(96\)00047-9](https://doi.org/10.1016/s0958-9465(96)00047-9).
- 1772 [145] A. Leemann, F. Moro, Carbonation of concrete: the role of CO₂ concentration, relative humidity
1773 and CO₂ buffer capacity, *Mater. Struct.* 50 (2017) 30. <https://doi.org/10.1617/s11527-016-0917-2>.
- 1774
- 1775 [146] E. Drouet, S. Poyet, P. Le Bescop, J.-M. Torrenti, X. Bourbon, Carbonation of hardened cement
1776 pastes: Influence of temperature, *Cem. Concr. Res.* 115 (2019) 445–459.
1777 <https://doi.org/10.1016/j.cemconres.2018.09.019>.

- 1778 [147] A. V. Saetta, B.A. Schrefler, R. V. Vitaliani, The carbonation of concrete and the mechanism of
1779 moisture, heat and carbon dioxide flow through porous materials, *Cem. Concr. Res.* 23 (1993)
1780 761–772. [https://doi.org/10.1016/0008-8846\(93\)90030-D](https://doi.org/10.1016/0008-8846(93)90030-D).
- 1781 [148] A. V. Saetta, R. V. Vitaliani, Experimental investigation and numerical modeling of carbonation
1782 process in reinforced concrete structures Part I: Theoretical formulation, *Cem. Concr. Res.* 34
1783 (2004) 571–579. <https://doi.org/10.1016/j.cemconres.2003.09.009>.
- 1784 [149] O.B. Isgor, A.G.G. Razaqpur, Finite element modeling of coupled heat transfer, moisture
1785 transport and carbonation processes in concrete structures, *Cem. Concr. Compos.* 26 (2004)
1786 57–73. [https://doi.org/10.1016/S0958-9465\(02\)00125-7](https://doi.org/10.1016/S0958-9465(02)00125-7).
- 1787 [150] V.G. Papadakis, C.G. Vayenas, M.N. Fardis, A reaction engineering approach to the problem of
1788 concrete carbonation, *AIChE J.* 35 (1989) 1639–1650. <https://doi.org/10.1002/aic.690351008>.
- 1789 [151] B. Johannesson, P. Utgenannt, Microstructural changes caused by carbonation of cement
1790 mortar, *Cem. Concr. Res.* 31 (2001) 925–931. [https://doi.org/10.1016/S0008-8846\(01\)00498-](https://doi.org/10.1016/S0008-8846(01)00498-7)
1791 7.
- 1792 [152] W. Ashraf, Carbonation of cement-based materials: Challenges and opportunities, *Constr.*
1793 *Build. Mater.* 120 (2016) 558–570. <https://doi.org/10.1016/j.conbuildmat.2016.05.080>.
- 1794 [153] S.E. Pihlajavaara, Some results of the effect of carbonation on the porosity and pore size
1795 distribution of cement paste, *Matériaux Constr.* 1 (1968) 521–527.
1796 <https://doi.org/10.1007/BF02473640>.
- 1797 [154] M. Auroy, S. Poyet, P. Le Bescop, J.-M. Torrenti, T. Charpentier, M. Moskura, X. Bourbon, Impact
1798 of carbonation on unsaturated water transport properties of cement-based materials, *Cem.*
1799 *Concr. Res.* 74 (2015) 44–58. <https://doi.org/10.1016/j.cemconres.2015.04.002>.
- 1800 [155] V.T. Ngala, C.L. Page, Effects of carbonation on pore structure and diffusional properties of
1801 hydrated cement pastes, *Cem. Concr. Res.* 27 (1997) 995–1007.
1802 [https://doi.org/10.1016/S0008-8846\(97\)00102-6](https://doi.org/10.1016/S0008-8846(97)00102-6).
- 1803 [156] S. Laurens, F. Deby, *Electrochemical Methods*, in: *Non-Destructive Test. Eval. Civ. Eng. Struct.*,
1804 Elsevier, 2018: pp. 173–197. <https://doi.org/10.1016/B978-1-78548-229-8.50005-4>.
- 1805 [157] M. Castellote, L. Fernandez, C. Andrade, C. Alonso, Chemical changes and phase analysis of OPC
1806 pastes carbonated at different CO₂ concentrations, *Mater. Struct.* 42 (2009) 515–525.
1807 <https://doi.org/10.1617/s11527-008-9399-1>.
- 1808 [158] M. Auroy, S. Poyet, P. Le Bescop, J.-M. Torrenti, T. Charpentier, M. Moskura, X. Bourbon,
1809 Comparison between natural and accelerated carbonation (3% CO₂): Impact on mineralogy,
1810 microstructure, water retention and cracking, *Cem. Concr. Res.* 109 (2018) 64–80.
1811 <https://doi.org/10.1016/j.cemconres.2018.04.012>.
- 1812 [159] B. Huet, V. L’Hostis, F. Miserque, H. Idrissi, Electrochemical behavior of mild steel in concrete:
1813 Influence of pH and carbonate content of concrete pore solution, *Electrochim. Acta.* 51 (2005)
1814 172–180. <https://doi.org/10.1016/j.electacta.2005.04.014>.
- 1815 [160] V. Marcos-Meson, A. Michel, A. Solgaard, G. Fischer, C. Edvardsen, T.L. Skovhus, Corrosion
1816 resistance of steel fibre reinforced concrete - A literature review, *Cem. Concr. Res.* 103 (2018)
1817 1–20. <https://doi.org/10.1016/j.cemconres.2017.05.016>.
- 1818 [161] M. Thiery, Modelling of atmospheric carbonation of cement based materials considering the
1819 kinetic effects and modifications of the microstructure and the hydric state, *Ecole des Ponts*
1820 ParisTech, 2005.

- 1821 [162] M.G. Sohail, S. Laurens, F. Deby, J.P. Balayssac, Significance of macrocell corrosion of reinforcing
1822 steel in partially carbonated concrete: numerical and experimental investigation, *Mater. Struct.*
1823 48 (2015) 217–233. <https://doi.org/10.1617/s11527-013-0178-2>.
- 1824 [163] A.B. Revert, K. De Weerd, K. Hornbostel, M.R. Geiker, Carbonation-induced corrosion:
1825 Investigation of the corrosion onset, *Constr. Build. Mater.* 162 (2018) 847–856.
1826 <https://doi.org/10.1016/j.conbuildmat.2017.12.066>.
- 1827 [164] L.J. Parrott, D.C. Kiloh, Carbonation in a 36 year old, in-situ concrete, *Cem. Concr. Res.* 19 (1989)
1828 649–656. [https://doi.org/10.1016/0008-8846\(89\)90017-3](https://doi.org/10.1016/0008-8846(89)90017-3).
- 1829 [165] R.M. Ghantous, R. François, S. Poyet, V. L’Hostis, F. Bernachy-Barbe, D. Meinel, L. Portier, N.-C.
1830 Tran, Relation between crack opening and extent of the damage induced at the steel/mortar
1831 interface, *Constr. Build. Mater.* 193 (2018) 97–104.
1832 <https://doi.org/10.1016/j.conbuildmat.2018.10.176>.
- 1833 [166] A. Nasser, A. Clément, S. Laurens, A. Castel, Influence of steel–concrete interface condition on
1834 galvanic corrosion currents in carbonated concrete, *Corros. Sci.* 52 (2010) 2878–2890.
1835 <https://doi.org/10.1016/j.corsci.2010.04.037>.
- 1836 [167] C.M. Hansson, A. Poursae, A. Laurent, Macrocell and microcell corrosion of steel in ordinary
1837 Portland cement and high performance concretes, *Cem. Concr. Res.* 36 (2006) 2098–2102.
1838 <https://doi.org/10.1016/j.cemconres.2006.07.005>.
- 1839 [168] A. Poursae, C.M. Hansson, Potential pitfalls in assessing chloride-induced corrosion of steel in
1840 concrete, *Cem. Concr. Res.* 39 (2009) 391–400.
1841 <https://doi.org/10.1016/j.cemconres.2009.01.015>.
- 1842 [169] A.B. Revert, K. Hornbostel, K. De Weerd, M.R. Geiker, Macrocell corrosion in carbonated
1843 Portland and Portland-fly ash concrete - Contribution and mechanism, *Cem. Concr. Res.* 116
1844 (2019) 273–283. <https://doi.org/10.1016/j.cemconres.2018.12.005>.
- 1845 [170] M. Stefanoni, U. Angst, B. Elsener, Corrosion rate of carbon steel in carbonated concrete – A
1846 critical review, *Cem. Concr. Res.* 103 (2018) 35–48.
1847 <https://doi.org/10.1016/j.cemconres.2017.10.007>.
- 1848 [171] P. Dangla, W. Dridi, Rebar corrosion in carbonated concrete exposed to variable humidity
1849 conditions. Interpretation of Tuutti’s curve, *Corros. Sci.* 51 (2009) 1747–1756.
1850 <https://doi.org/10.1016/j.corsci.2009.04.029>.
- 1851 [172] M. Stefanoni, U. Angst, B. Elsener, The mechanism controlling corrosion of steel in carbonated
1852 cementitious materials in wetting and drying exposure, *Cem. Concr. Compos.* 113 (2020)
1853 103717. <https://doi.org/10.1016/j.cemconcomp.2020.103717>.
- 1854 [173] M.U. Khan, S. Ahmad, H.J. Al-Gahtani, Chloride-induced corrosion of steel in concrete: An
1855 overview on chloride diffusion and prediction of corrosion initiation time, *Int. J. Corros.* 2017
1856 (2017) 1–9. <https://doi.org/10.1155/2017/5819202>.
- 1857 [174] M.. Pech-Canul, P. Castro, Corrosion measurements of steel reinforcement in concrete exposed
1858 to a tropical marine atmosphere, *Cem. Concr. Res.* 32 (2002) 491–498.
1859 [https://doi.org/10.1016/S0008-8846\(01\)00713-X](https://doi.org/10.1016/S0008-8846(01)00713-X).
- 1860 [175] M. Balonis, B. Lothenbach, G. Le Saout, F.P. Glasser, Impact of chloride on the mineralogy of
1861 hydrated Portland cement systems, *Cem. Concr. Res.* 40 (2010) 1009–1022.
1862 <https://doi.org/10.1016/j.cemconres.2010.03.002>.
- 1863 [176] B. Guo, Y. Hong, G. Qiao, J. Ou, Z. Li, Thermodynamic modeling of the essential physicochemical

- 1864 interactions between the pore solution and the cement hydrates in chloride-contaminated
 1865 cement-based materials, *J. Colloid Interface Sci.* 531 (2018) 56–63.
 1866 <https://doi.org/10.1016/j.jcis.2018.07.005>.
- 1867 [177] Y. Guo, T. Zhang, W. Tian, J. Wei, Q. Yu, Physically and chemically bound chlorides in hydrated
 1868 cement pastes: a comparison study of the effects of silica fume and metakaolin, *J. Mater. Sci.*
 1869 54 (2019) 2152–2169. <https://doi.org/10.1007/s10853-018-2953-5>.
- 1870 [178] P.T. Nguyen, O. Amiri, Study of the chloride transport in unsaturated concrete: Highlighting of
 1871 electrical double layer, temperature and hysteresis effects, *Constr. Build. Mater.* 122 (2016)
 1872 284–293. <https://doi.org/10.1016/j.conbuildmat.2016.05.154>.
- 1873 [179] Y. Zhang, M. Zhang, G. Ye, Influence of moisture condition on chloride diffusion in partially
 1874 saturated ordinary Portland cement mortar, *Mater. Struct.* 51 (2018) 36.
 1875 <https://doi.org/10.1617/s11527-018-1162-7>.
- 1876 [180] S. Caré, Influence of aggregates on chloride diffusion coefficient into mortar, *Cem. Concr. Res.*
 1877 33 (2003) 1021–1028. [https://doi.org/10.1016/S0008-8846\(03\)00009-7](https://doi.org/10.1016/S0008-8846(03)00009-7).
- 1878 [181] P.P. Win, M. Watanabe, A. Machida, Penetration profile of chloride ion in cracked reinforced
 1879 concrete, *Cem. Concr. Res.* 34 (2004) 1073–1079.
 1880 <https://doi.org/10.1016/j.cemconres.2003.11.020>.
- 1881 [182] A. Poursaeed, C.M. Hansson, The influence of longitudinal cracks on the corrosion protection
 1882 afforded reinforcing steel in high performance concrete, *Cem. Concr. Res.* 38 (2008) 1098–
 1883 1105. <https://doi.org/10.1016/j.cemconres.2008.03.018>.
- 1884 [183] J. Shi, J. Ming, Influence of defects at the steel-mortar interface on the corrosion behavior of
 1885 steel, *Constr. Build. Mater.* 136 (2017) 118–125.
 1886 <https://doi.org/10.1016/j.conbuildmat.2017.01.007>.
- 1887 [184] F.U.A. Shaikh, Effect of cracking on corrosion of steel in concrete, *Int. J. Concr. Struct. Mater.*
 1888 12 (2018) 3. <https://doi.org/10.1186/s40069-018-0234-y>.
- 1889 [185] E. Samson, J. Marchand, Modeling the transport of ions in unsaturated cement-based materials,
 1890 *Comput. Struct.* 85 (2007) 1740–1756. <https://doi.org/10.1016/j.compstruc.2007.04.008>.
- 1891 [186] V.Q. Tran, A. Soive, V. Baroghel-Bouny, Modélisation of chloride reactive transport in concrete
 1892 including thermodynamic equilibrium, kinetic control and surface complexation, *Cem. Concr.*
 1893 *Res.* 110 (2018) 70–85. <https://doi.org/10.1016/j.cemconres.2018.05.007>.
- 1894 [187] U.M. Angst, Predicting the time to corrosion initiation in reinforced concrete structures
 1895 exposed to chlorides, *Cem. Concr. Res.* 115 (2019) 559–567.
 1896 <https://doi.org/10.1016/j.cemconres.2018.08.007>.
- 1897 [188] A. Covelo, B. Díaz, L. Freire, X.R. Nóvoa, M.C. Pérez, Microstructural changes in a cementitious
 1898 membrane due to the application of a DC electric field, *J. Environ. Sci. Heal. Part A.* 43 (2008)
 1899 985–993. <https://doi.org/10.1080/10934520801974632>.
- 1900 [189] M.A. Heine, D.S. Keir, M.J. Pryor, The specific effects of chloride and sulfate ions on oxide
 1901 covered aluminum, *J. Electrochem. Soc.* 112 (1965) 24–32. <https://doi.org/10.1149/1.2423459>.
- 1902 [190] D.D. Macdonald, The point defect model for the passive state, *J. Electrochem. Soc.* 139 (1992)
 1903 3434. <https://doi.org/10.1149/1.2069096>.
- 1904 [191] P. Marcus, V. Maurice, H.-H. Strehblow, Localized corrosion (pitting): A model of passivity
 1905 breakdown including the role of the oxide layer nanostructure, *Corros. Sci.* 50 (2008) 2698–
 1906 2704. <https://doi.org/10.1016/j.corsci.2008.06.047>.

- 1907 [192] P. Ghods, O. Burkan Isgor, F. Bensebaa, D. Kingston, Angle-resolved XPS study of carbon steel
1908 passivity and chloride-induced depassivation in simulated concrete pore solution, *Corros. Sci.*
1909 (2012). <https://doi.org/10.1016/j.corsci.2012.01.019>.
- 1910 [193] P. Ghods, O. Burkan Isgor, G.J.C. Carpenter, J. Li, G.A. McRae, G.P. Gu, Nano-scale study of
1911 passive films and chloride-induced depassivation of carbon steel rebar in simulated concrete
1912 pore solutions using FIB/TEM, *Cem. Concr. Res.* 47 (2013) 55–68.
1913 <https://doi.org/10.1016/j.cemconres.2013.01.009>.
- 1914 [194] H.B. Gunay, P. Ghods, O. Burkan Isgor, G.J.C. Carpenter, X. Wu, Characterization of atomic
1915 structure of oxide films on carbon steel in simulated concrete pore solutions using EELS, *Appl.*
1916 *Surf. Sci.* 274 (2013) 195–202. <https://doi.org/10.1016/j.apsusc.2013.03.014>.
- 1917 [195] J. Xu, L. Jiang, Investigation on chloride threshold level for corrosion of reinforcing steel in the
1918 saturated Ca(OH)₂ solution simulating the electrolytic environments of concrete, in: *Adv. Civ.*
1919 *Eng. Mater. 50-Year Teach. Res. Anniv. Prof. Sun Wei, Nanjing, China, 2008*: pp. 111–119.
- 1920 [196] Q. Pang, H. DorMohammadi, O. Burkan Isgor, L. Árnadóttir, The effect of surface vacancies on
1921 the interactions of Cl with the α -Fe₂O₃ (0001) surface and the role of Cl in depassivation,
1922 *Corros. Sci.* (2019). <https://doi.org/10.1016/j.corsci.2019.03.052>.
- 1923 [197] H. DorMohammadi, Q. Pang, P. Murkute, L. Árnadóttir, O.B. Isgor, Investigation of chloride-
1924 induced depassivation of iron in alkaline media by reactive force field molecular dynamics, *Npj*
1925 *Mater. Degrad.* 3 (2019) 19. <https://doi.org/10.1038/s41529-019-0081-6>.
- 1926 [198] G.K. Glass, N.R. Buenfeld, The presentation of the chloride threshold level for corrosion of steel
1927 in concrete, *Corros. Sci.* 39 (1997) 1001–1013. [https://doi.org/10.1016/S0010-938X\(97\)00009-](https://doi.org/10.1016/S0010-938X(97)00009-7)
1928 [7](https://doi.org/10.1016/S0010-938X(97)00009-7).
- 1929 [199] U. Angst, B. Elsener, C.K. Larsen, Ø. Vennesland, Critical chloride content in reinforced concrete
1930 - A review, *Cem. Concr. Res.* 39 (2009) 1122–1138.
1931 <https://doi.org/10.1016/j.cemconres.2009.08.006>.
- 1932 [200] B. Martín-Pérez, H. Zibara, R.D. Hooton, M.D.A. Thomas, A study of the effect of chloride
1933 binding on service life predictions, *Cem. Concr. Res.* 30 (2000) 1215–1223.
1934 [https://doi.org/10.1016/S0008-8846\(00\)00339-2](https://doi.org/10.1016/S0008-8846(00)00339-2).
- 1935 [201] M. Saillio, V. Baroghel-Bouny, F. Barberon, Chloride binding in sound and carbonated
1936 cementitious materials with various types of binder, *Constr. Build. Mater.* 68 (2014) 82–91.
1937 <https://doi.org/10.1016/j.conbuildmat.2014.05.049>.
- 1938 [202] C. Alonso, C. Andrade, M. Castellote, P. Castro, Chloride threshold values to depassivate
1939 reinforcing bars embedded in a standardized OPC mortar, *Cem. Concr. Res.* 30 (2000) 1047–
1940 1055. [https://doi.org/10.1016/S0008-8846\(00\)00265-9](https://doi.org/10.1016/S0008-8846(00)00265-9).
- 1941 [203] U.M. Angst, B. Elsener, C.K. Larsen, Ø. Vennesland, Chloride induced reinforcement corrosion:
1942 Electrochemical monitoring of initiation stage and chloride threshold values, *Corros. Sci.* 53
1943 (2011) 1451–1464. <https://doi.org/10.1016/j.corsci.2011.01.025>.
- 1944 [204] N. Silva, Chloride Induced Corrosion of Reinforcement Steel in Concrete, Chalmers University
1945 of Technology, 2013.
- 1946 [205] R.B. Figueira, A. Sadovski, A.P. Melo, E. V. Pereira, Chloride threshold value to initiate
1947 reinforcement corrosion in simulated concrete pore solutions: The influence of surface finishing
1948 and pH, *Constr. Build. Mater.* 141 (2017) 183–200.
1949 <https://doi.org/10.1016/j.conbuildmat.2017.03.004>.

- 1950 [206] K.Y. Ann, H.-W. Song, Chloride threshold level for corrosion of steel in concrete, *Corros. Sci.* 49
1951 (2007) 4113–4133. <https://doi.org/10.1016/j.corsci.2007.05.007>.
- 1952 [207] Y. Cao, C. Gehlen, U. Angst, L. Wang, Z. Wang, Y. Yao, Critical chloride content in reinforced
1953 concrete — An updated review considering Chinese experience, *Cem. Concr. Res.* 117 (2019)
1954 58–68. <https://doi.org/10.1016/j.cemconres.2018.11.020>.
- 1955 [208] A. Kenny, A. Katz, Steel-concrete interface influence on chloride threshold for corrosion –
1956 Empirical reinforcement to theory, *Constr. Build. Mater.* 244 (2020) 118376.
1957 <https://doi.org/10.1016/j.conbuildmat.2020.118376>.
- 1958 [209] U.M. Angst, B. Elsener, Chloride threshold values in concrete - A look back and ahead, *Spec.*
1959 *Publ.* 308 (2016) 1–12.
- 1960 [210] C.L. Page, Initiation of chloride-induced corrosion of steel in concrete: role of the interfacial
1961 zone, *Mater. Corros.* 60 (2009) 586–592. <https://doi.org/10.1002/maco.200905278>.
- 1962 [211] U.M. Angst, B. Elsener, The size effect in corrosion greatly influences the predicted life span of
1963 concrete infrastructures, *Sci. Adv.* 3 (2017) e1700751. <https://doi.org/10.1126/sciadv.1700751>.
- 1964 [212] J.A. Gonzalez, A. Molina, E. Otero, W. López, On the mechanism of steel corrosion in concrete:
1965 the role of oxygen diffusion, *Mag. Concr. Res.* 42 (1990) 23–27.
1966 <https://doi.org/10.1680/macr.1990.42.150.23>.
- 1967 [213] J.A. González, E. Otero, S. Feliu, W. López, Initial steps of corrosion in the steel/Ca(OH)₂ + Cl-
1968 system: The role of heterogeneities on the steel surface and oxygen supply, *Cem. Concr. Res.*
1969 23 (1993) 33–40. [https://doi.org/10.1016/0008-8846\(93\)90132-S](https://doi.org/10.1016/0008-8846(93)90132-S).
- 1970 [214] T.D. Marcotte, Characterization of chloride-induced corrosion products that form in steel-
1971 reinforced cementitious materials, University of Waterloo, 2001.
- 1972 [215] K.K. Sagoe-Crentsil, F.P. Glasser, “Green rust”, iron solubility and the role of chloride in the
1973 corrosion of steel at high pH, *Cem. Concr. Res.* 23 (1993) 785–791.
1974 [https://doi.org/10.1016/0008-8846\(93\)90032-5](https://doi.org/10.1016/0008-8846(93)90032-5).
- 1975 [216] U. Angst, B. Elsener, C.K. Larsen, Ø. Vennesland, Chloride induced reinforcement corrosion:
1976 Rate limiting step of early pitting corrosion, *Electrochim. Acta.* 56 (2011) 5877–5889.
1977 <https://doi.org/10.1016/j.electacta.2011.04.124>.
- 1978 [217] M. Pourbaix, Applications of electrochemistry in corrosion science and in practice, *Corros. Sci.*
1979 14 (1974) 25–82. [https://doi.org/10.1016/S0010-938X\(74\)80006-5](https://doi.org/10.1016/S0010-938X(74)80006-5).
- 1980 [218] U. Angst, B. Elsener, A. Jamali, B. Adey, Concrete cover cracking owing to reinforcement
1981 corrosion - theoretical considerations and practical experience, *Mater. Corros.* 63 (2012) 1069–
1982 1077. <https://doi.org/10.1002/maco.201206669>.
- 1983 [219] J. Warkus, M. Raupach, Modelling of reinforcement corrosion - geometrical effects on
1984 macrocell corrosion, *Mater. Corros.* 61 (2009) 494–504.
1985 <https://doi.org/10.1002/maco.200905437>.
- 1986 [220] J.A. González, C. Andrade, C. Alonso, S. Feliu, Comparison of rates of general corrosion and
1987 maximum pitting penetration on concrete embedded steel reinforcement, *Cem. Concr. Res.* 25
1988 (1995) 257–264. [https://doi.org/10.1016/0008-8846\(95\)00006-2](https://doi.org/10.1016/0008-8846(95)00006-2).
- 1989 [221] L. Yu, R. François, V.H. Dang, V. L’Hostis, R. Gagné, Distribution of corrosion and pitting factor
1990 of steel in corroded RC beams, *Constr. Build. Mater.* 95 (2015) 384–392.
1991 <https://doi.org/10.1016/j.conbuildmat.2015.07.119>.

- 1992 [222] R. François, S. Laurens, F. Deby, Which parameter to quantify corrosion intensity?, in: Corros.
 1993 Its Consequences Reinf. Concr. Struct., Elsevier, 2018: pp. 63–76.
 1994 <https://doi.org/10.1016/B978-1-78548-234-2.50003-2>.
- 1995 [223] C. Arya, P.R.. Vassie, Influence of cathode-to-anode area ratio and separation distance on
 1996 galvanic corrosion currents of steel in concrete containing chlorides, Cem. Concr. Res. 25 (1995)
 1997 989–998. [https://doi.org/10.1016/0008-8846\(95\)00094-S](https://doi.org/10.1016/0008-8846(95)00094-S).
- 1998 [224] C. Chalhoub, R. François, M. Carcasses, Effect of cathode–anode distance and electrical
 1999 resistivity on macrocell corrosion currents and cathodic response in cases of chloride induced
 2000 corrosion in reinforced concrete structures, Constr. Build. Mater. 245 (2020) 118337.
 2001 <https://doi.org/10.1016/j.conbuildmat.2020.118337>.
- 2002 [225] L. Bourreau, L. Gaillet, V. Bouteiller, F. Schoefs, B. Thauvin, J. Schneider, S. Naar, Spatial
 2003 identification of exposure zones of concrete structures exposed to a marine environment with
 2004 respect to reinforcement corrosion, Struct. Infrastruct. Eng. 16 (2020) 346–354.
 2005 <https://doi.org/10.1080/15732479.2019.1655072>.
- 2006 [226] S.J. Jaffer, C.M. Hansson, Chloride-induced corrosion products of steel in cracked-concrete
 2007 subjected to different loading conditions, Cem. Concr. Res. 39 (2009) 116–125.
 2008 <https://doi.org/10.1016/j.cemconres.2008.11.001>.
- 2009 [227] R.M. Cornell, U. Schwertmann, The Iron Oxides: Structure, Properties, Reactions, Occurrences,
 2010 and Uses, Wiley-VCH, 2003.
- 2011 [228] J.A. González, J.M. Miranda, E. Otero, S. Feliu, Effect of electrochemically reactive rust layers
 2012 on the corrosion of steel in a Ca(OH)₂ solution, Corros. Sci. 49 (2007) 436–448.
 2013 <https://doi.org/10.1016/j.corsci.2006.04.014>.
- 2014 [229] M. Stefanoni, U. Angst, B. Elsener, Local electrochemistry of reinforcement steel – Distribution
 2015 of open circuit and pitting potentials on steels with different surface condition, Corros. Sci. 98
 2016 (2015) 610–618. <https://doi.org/10.1016/j.corsci.2015.06.004>.
- 2017 [230] Y. Ji, M. Wu, Z. Tan, F. Gao, F. Liu, Process control of reinforcement corrosion in concrete. Part
 2018 2: Time-dependent dominating factors under different environmental conditions, Constr. Build.
 2019 Mater. 73 (2014) 214–221. <https://doi.org/10.1016/j.conbuildmat.2014.09.103>.
- 2020 [231] Y. Ji, G. Zhan, Z. Tan, Y. Hu, F. Gao, Process control of reinforcement corrosion in concrete. Part
 2021 1: Effect of corrosion products, Constr. Build. Mater. 79 (2015) 214–222.
 2022 <https://doi.org/10.1016/j.conbuildmat.2014.12.083>.
- 2023 [232] E. Burger, J. Monnier, P. Berger, D. Neff, V. L’Hostis, S. Perrin, P. Dillmann, The long-term
 2024 corrosion of mild steel in depassivated concrete: Localizing the oxygen reduction sites in
 2025 corrosion products by isotopic tracer method, J. Mater. Res. 26 (2011) 3107–3115.
 2026 <https://doi.org/10.1557/jmr.2011.391>.
- 2027 [233] I. Azoulay, C. Rémazeilles, P. Refait, Corrosion of steel in carbonated media: The oxidation
 2028 processes of chukanovite (Fe₂(OH)₂CO₃), Corros. Sci. 85 (2014) 101–108.
 2029 <https://doi.org/10.1016/j.corsci.2014.04.004>.
- 2030 [234] A. Köliö, M. Honkanen, J. Lahdensivu, M. Vippola, M. Pentti, Corrosion products of carbonation
 2031 induced corrosion in existing reinforced concrete facades, Cem. Concr. Res. 78 (2015) 200–207.
 2032 <https://doi.org/10.1016/j.cemconres.2015.07.009>.
- 2033 [235] J. Hadi, P. Wersin, V. Serneels, J.-M. Greneche, Eighteen years of steel–bentonite interaction in
 2034 the FEBEX in situ test at the Grimsel Test Site in Switzerland, Clays Clay Miner. 67 (2019) 111–
 2035 131. <https://doi.org/10.1007/s42860-019-00012-5>.

- 2036 [236] K.K. Sagoe-Crentsil, F.P. Glasser, Constitution of green rust and its significance to the corrosion
2037 of steel in Portland cement, *Corrosion*. 49 (1993) 457–463. <https://doi.org/10.5006/1.3316072>.
- 2038 [237] K. Suda, S. Misra, K. Motohashi, Corrosion products of reinforcing bars embedded in concrete,
2039 *Corros. Sci.* 35 (1993) 1543–1549. [https://doi.org/10.1016/0010-938X\(93\)90382-Q](https://doi.org/10.1016/0010-938X(93)90382-Q).
- 2040 [238] V. L’Hostis, E. Amblard, W. Guillot, C. Paris, L. Bellot-Gurlet, Characterisation of the steel
2041 concrete interface submitted to chloride-induced-corrosion, *Mater. Corros.* 64 (2013) 185–194.
2042 <https://doi.org/10.1002/maco.201106488>.
- 2043 [239] J. Shi, J. Ming, Y. Zhang, J. Jiang, Corrosion products and corrosion-induced cracks of low-alloy
2044 steel and low-carbon steel in concrete, *Cem. Concr. Compos.* 88 (2018) 121–129.
2045 <https://doi.org/10.1016/j.cemconcomp.2018.02.002>.
- 2046 [240] P. Refait, J.-M.R. Génin, The mechanisms of oxidation of ferrous hydroxychloride $\beta\text{-Fe}_2(\text{OH})_3\text{Cl}$
2047 in aqueous solution: The formation of akaganeite vs goethite, *Corros. Sci.* 39 (1997) 539–553.
2048 [https://doi.org/10.1016/S0010-938X\(97\)86102-1](https://doi.org/10.1016/S0010-938X(97)86102-1).
- 2049 [241] C. Rémazeilles, P. Refait, On the formation of $\beta\text{-FeOOH}$ (Akaganéite) in chloride-containing
2050 environments, *Corros. Sci.* 49 (2007) 844–857. <https://doi.org/10.1016/j.corsci.2006.06.003>.
- 2051 [242] Y. Zhao, Y. Wu, W. Jin, Distribution of millscale on corroded steel bars and penetration of steel
2052 corrosion products in concrete, *Corros. Sci.* 66 (2013) 160–168.
2053 <https://doi.org/10.1016/j.corsci.2012.09.014>.
- 2054 [243] K.K. Aligizaki, M.R. de Rooij, D.D. Macdonald, Analysis of iron oxides accumulating at the
2055 interface between aggregates and cement paste, *Cem. Concr. Res.* 30 (2000) 1941–1945.
2056 [https://doi.org/10.1016/S0008-8846\(00\)00392-6](https://doi.org/10.1016/S0008-8846(00)00392-6).
- 2057 [244] H.S. Wong, Y.X. Zhao, A.R. Karimi, N.R. Buenfeld, W.L. Jin, On the penetration of corrosion
2058 products from reinforcing steel into concrete due to chloride-induced corrosion, *Corros. Sci.* 52
2059 (2010) 2469–2480. <https://doi.org/10.1016/j.corsci.2010.03.025>.
- 2060 [245] T.D. Marcotte, C.M. Hansson, Corrosion products that form on steel within cement paste,
2061 *Mater. Struct.* 40 (2007) 325–340. <https://doi.org/10.1617/s11527-006-9170-4>.
- 2062 [246] Y. Zhao, H. Ren, H. Dai, W. Jin, Composition and expansion coefficient of rust based on X-ray
2063 diffraction and thermal analysis, *Corros. Sci.* 53 (2011) 1646–1658.
2064 <https://doi.org/10.1016/j.corsci.2011.01.007>.
- 2065 [247] G. Fang, W. Ding, Y. Liu, J. Zhang, F. Xing, B. Dong, Identification of corrosion products and 3D
2066 distribution in reinforced concrete using X-ray micro computed tomography, *Constr. Build.*
2067 *Mater.* 207 (2019) 304–315. <https://doi.org/10.1016/j.conbuildmat.2019.02.133>.
- 2068 [248] C. Lu, W. Jin, R. Liu, Reinforcement corrosion-induced cover cracking and its time prediction for
2069 reinforced concrete structures, *Corros. Sci.* 53 (2011) 1337–1347.
2070 <https://doi.org/10.1016/j.corsci.2010.12.026>.
- 2071 [249] B. Sanz, J. Planas, J.M. Sancho, A closer look to the mechanical behavior of the oxide layer in
2072 concrete reinforcement corrosion, *Int. J. Solids Struct.* 62 (2015) 256–268.
2073 <https://doi.org/10.1016/j.ijsolstr.2015.02.040>.
- 2074 [250] Y. Liu, R.E. Weyers, Modeling the time-to-corrosion cracking in chloride contaminated
2075 reinforced concrete structures, *ACI Mater. J.* 95 (1998) 675–680. <https://doi.org/10.14359/410>.
- 2076 [251] A. Poursaee, Temperature dependence of the formation of the passivation layer on carbon steel
2077 in high alkaline environment of concrete pore solution, *Electrochem. Commun.* 73 (2016) 24–
2078 28. <https://doi.org/10.1016/j.elecom.2016.10.003>.

- 2079 [252] B. Díaz, B. Guitián, X.R. Nóvoa, M.C. Pérez, The effect of long-term atmospheric aging and
2080 temperature on the electrochemical behaviour of steel rebars in mortar, *Corros. Sci.* 140 (2018)
2081 143–150. <https://doi.org/10.1016/j.corsci.2018.06.007>.
- 2082 [253] J.M. Deus, L. Freire, M.F. Montemor, X.R. Nóvoa, The corrosion potential of stainless steel
2083 rebars in concrete: Temperature effect, *Corros. Sci.* 65 (2012) 556–560.
2084 <https://doi.org/10.1016/j.corsci.2012.09.001>.
- 2085 [254] A. Česen, T. Kosec, A. Legat, Characterization of steel corrosion in mortar by various
2086 electrochemical and physical techniques, *Corros. Sci.* 75 (2013) 47–57.
2087 <https://doi.org/10.1016/j.corsci.2013.05.015>.
- 2088 [255] B. Šavija, M. Luković, S.A.S. Hosseini, J. Pacheco, E. Schlangen, Corrosion induced cover cracking
2089 studied by X-ray computed tomography, nanoindentation, and energy dispersive X-ray
2090 spectrometry (EDS), *Mater. Struct.* 48 (2015) 2043–2062. <https://doi.org/10.1617/s11527-014-0292-9>.
- 2092 [256] B. Dong, G. Fang, Y. Liu, P. Dong, J. Zhang, F. Xing, S. Hong, Monitoring reinforcement corrosion
2093 and corrosion-induced cracking by X-ray microcomputed tomography method, *Cem. Concr.*
2094 *Res.* 100 (2017) 311–321. <https://doi.org/10.1016/j.cemconres.2017.07.009>.
- 2095 [257] G. Fang, Y. Liu, S. Qin, W. Ding, J. Zhang, S. Hong, F. Xing, B. Dong, Visualized tracing of crack
2096 self-healing features in cement/microcapsule system with X-ray microcomputed tomography,
2097 *Constr. Build. Mater.* 179 (2018) 336–347. <https://doi.org/10.1016/j.conbuildmat.2018.05.193>.
- 2098 [258] B. Dong, G. Shi, P. Dong, W. Ding, X. Teng, S. Qin, Y. Liu, F. Xing, S. Hong, Visualized tracing of
2099 rebar corrosion evolution in concrete with X-ray micro-computed tomography method, *Cem.*
2100 *Concr. Compos.* 92 (2018) 102–109. <https://doi.org/10.1016/j.cemconcomp.2018.06.003>.
- 2101 [259] W.-J. Chitty, P. Dillmann, V. L’Hostis, C. Lombard, Long-term corrosion resistance of metallic
2102 reinforcements in concrete—a study of corrosion mechanisms based on archaeological
2103 artefacts, *Corros. Sci.* 47 (2005) 1555–1581. <https://doi.org/10.1016/j.corsci.2004.07.032>.
- 2104 [260] V. L’Hostis, D. Neff, L. Bellot-Gurlet, P. Dillmann, Characterization of long-term corrosion of
2105 rebars embedded in concretes sampled on French historical buildings aged from 50 to 80 years,
2106 *Mater. Corros.* 60 (2009) 93–98. <https://doi.org/10.1002/maco.200805019>.
- 2107 [261] Y. Zhao, H. Ding, W. Jin, Development of the corrosion-filled paste and corrosion layer at the
2108 steel/concrete interface, *Corros. Sci.* 87 (2014) 199–210.
2109 <https://doi.org/10.1016/j.corsci.2014.06.032>.
- 2110 [262] Y. Zhao, X. Zhang, W. Jin, Influence of environment on the development of corrosion product-
2111 filled paste and a corrosion layer at the steel/concrete interface, *Corros. Sci.* 124 (2017) 1–9.
2112 <https://doi.org/10.1016/j.corsci.2017.03.026>.
- 2113 [263] Y. Zhao, B. Hu, J. Yu, W. Jin, Non-uniform distribution of rust layer around steel bar in concrete,
2114 *Corros. Sci.* 53 (2011) 4300–4308. <https://doi.org/10.1016/j.corsci.2011.08.045>.
- 2115 [264] C. Cao, M.M.S. Cheung, Non-uniform rust expansion for chloride-induced pitting corrosion in
2116 RC structures, *Constr. Build. Mater.* (2014).
2117 <https://doi.org/10.1016/j.conbuildmat.2013.10.042>.
- 2118 [265] Y. Zhao, J. Dong, Y. Wu, W. Jin, Corrosion-induced concrete cracking model considering
2119 corrosion product-filled paste at the concrete/steel interface, *Constr. Build. Mater.* 116 (2016)
2120 273–280. <https://doi.org/10.1016/j.conbuildmat.2016.04.097>.
- 2121 [266] X. Xi, S. Yang, C.-Q. Li, A non-uniform corrosion model and meso-scale fracture modelling of

- 2122 concrete, Cem. Concr. Res. 108 (2018) 87–102.
2123 <https://doi.org/10.1016/j.cemconres.2018.03.009>.
- 2124 [267] A. Jamali, U. Angst, B. Adey, B. Elsener, Modeling of corrosion-induced concrete cover cracking:
2125 A critical analysis, Constr. Build. Mater. 42 (2013) 225–237.
2126 <https://doi.org/10.1016/j.conbuildmat.2013.01.019>.
- 2127 [268] C. Andrade, I. Martínez, Techniques for measuring the corrosion rate (polarization resistance)
2128 and the corrosion potential of reinforced concrete structures, Non-Destructive Eval. Reinf.
2129 Concr. Struct. (2010) 284–316. <https://doi.org/10.1533/9781845699604.2.284>.
- 2130 [269] R. Francois, G. Arliguie, D. Bardy, Electrode potential measurements of concrete reinforcement
2131 for corrosion evaluation, Cem. Concr. Res. 24 (1994) 401–412. [https://doi.org/10.1016/0008-8846\(94\)90127-9](https://doi.org/10.1016/0008-8846(94)90127-9).
2132
- 2133 [270] K. Reichling, M. Raupach, Method to determine electrochemical potential gradients without
2134 reinforcement connection in concrete structures, Cem. Concr. Compos. 47 (2014) 3–8.
2135 <https://doi.org/10.1016/j.cemconcomp.2013.12.007>.
- 2136 [271] S. Garcia, F. Deby, Numerical and experimental development of gradient potential
2137 measurement for corrosion detection of reinforced concrete slab, in: Serv. Life Durab. Reinf.
2138 Concr. Struct., Cefracor, 2019: pp. 71–86. https://doi.org/10.1007/978-3-319-90236-4_6.
- 2139 [272] M. Pour-Ghaz, O.B. Isgor, P. Ghods, Quantitative interpretation of half-cell potential
2140 measurements in concrete structures, J. Mater. Civ. Eng. 21 (2009) 467–475.
2141 [https://doi.org/10.1061/\(ASCE\)0899-1561\(2009\)21:9\(467\)](https://doi.org/10.1061/(ASCE)0899-1561(2009)21:9(467)).
- 2142 [273] S.K. Verma, S.S. Bhadauria, S. Akhtar, Monitoring corrosion of steel bars in reinforced concrete
2143 structures, Sci. World J. 2014 (2014) 957904. <https://doi.org/10.1155/2014/957904>.
- 2144 [274] U. Angst, Ø. Vennesland, R. Myrdal, Diffusion potentials as source of error in electrochemical
2145 measurements in concrete, Mater. Struct. 42 (2009) 365–375. <https://doi.org/10.1617/s11527-008-9387-5>.
2146
- 2147 [275] P. Castro, A.A. Sagüés, E.I. Moreno, L. Maldonado, J. Genescá, Characterization of activated
2148 titanium solid reference electrodes for corrosion testing of steel in concrete, Corrosion. 52
2149 (1996) 609–617. <https://doi.org/10.5006/1.3292151>.
- 2150 [276] G.S. Duffó, S.B. Farina, Development of an embeddable sensor to monitor the corrosion process
2151 of new and existing reinforced concrete structures, Constr. Build. Mater. 23 (2009) 2746–2751.
2152 <https://doi.org/10.1016/j.conbuildmat.2009.04.001>.
- 2153 [277] S.P. Karthick, S. Muralidharan, V. Saraswathy, K. Thangavel, Long-term relative performance of
2154 embedded sensor and surface mounted electrode for corrosion monitoring of steel in concrete
2155 structures, Sensors Actuators B Chem. 192 (2014) 303–309.
2156 <https://doi.org/10.1016/j.snb.2013.10.123>.
- 2157 [278] M. Jin, Y. Jiang, L. Jiang, H. Chu, F. Zhi, S. Gao, Fabrication and characterization of pseudo
2158 reference electrode based on graphene-cement composites for corrosion monitoring in
2159 reinforced concrete structure, Constr. Build. Mater. 204 (2019) 144–157.
2160 <https://doi.org/10.1016/j.conbuildmat.2019.01.169>.
- 2161 [279] A. Sassolini, N. Colozza, E. Papa, K. Hermansson, I. Cacciotti, F. Arduini, Screen-printed electrode
2162 as a cost-effective and miniaturized analytical tool for corrosion monitoring of reinforced
2163 concrete, Electrochem. Commun. 98 (2019) 69–72.
2164 <https://doi.org/10.1016/j.elecom.2018.11.023>.

- 2165 [280] Ø. Vennesland, M. Raupach, C. Andrade, Recommendation of Rilem TC 154-EMC:
2166 "Electrochemical techniques for measuring corrosion in concrete"—measurements with
2167 embedded probes, *Mater. Struct.* 40 (2007) 745–758. [https://doi.org/10.1617/s11527-006-](https://doi.org/10.1617/s11527-006-9219-4)
2168 9219-4.
- 2169 [281] A. Leibbrandt, B. Elsener, C. Hürzeler, G. Caprati, R. Flatt, R. Siegwart, Climbing robot for
2170 corrosion monitoring and sensor for potential mapping, WO2013156142A1, 2013.
2171 <https://doi.org/10.2749/2221378027963366>.
- 2172 [282] B. Elsener, C. Andrade, J. Gulikers, R. Polder, M. Raupach, Half-cell potential measurements -
2173 Potential mapping on reinforced concrete structures, *Mater. Struct.* 36 (2003) 461–671.
2174 <https://doi.org/10.1007/BF02481526>.
- 2175 [283] ASTM_C876-09, Standard test method for corrosion potentials of uncoated reinforcing steel in
2176 concrete (2009), (n.d.). <https://www.astm.org/Standards/C876.htm>.
- 2177 [284] K. Reichling, M. Raupach, J. Broomfield, J. Gulikers, V. L'Hostis, S. Kessler, K. Osterminski, I.
2178 Pepenar, U. Schneck, G. Sergi, G. Taché, Full surface inspection methods regarding
2179 reinforcement corrosion of concrete structures, *Mater. Corros.* 64 (2013) 116–127.
2180 <https://doi.org/10.1002/maco.201206625>.
- 2181 [285] E. Sassine, S. Laurens, R. François, E. Ringot, A critical discussion on rebar electrical continuity
2182 and usual interpretation thresholds in the field of half-cell potential measurements in steel
2183 reinforced concrete, *Mater. Struct.* 51 (2018) 93. <https://doi.org/10.1617/s11527-018-1221-0>.
- 2184 [286] G.Y. Koga, B. Albert, R.P. Nogueira, Revisiting the ASTM C876 standard for corrosion of
2185 reinforcing steel: On the correlation between corrosion potential and polarization resistance
2186 during the curing of different cement mortars, *Electrochem. Commun.* 94 (2018) 1–4.
2187 <https://doi.org/10.1016/j.elecom.2018.07.017>.
- 2188 [287] P. Gu, J.J. Beaudoin, Obtaining Effective Half-Cell Potential Measurements in Reinforced
2189 Concrete Structures, National R, 1998.
- 2190 [288] W. Yodsudjai, T. Pattarakittam, Factors influencing half-cell potential measurement and its
2191 relationship with corrosion level, *Measurement.* 104 (2017) 159–168.
2192 <https://doi.org/10.1016/j.measurement.2017.03.027>.
- 2193 [289] J.-F. Lataste, G. Villain, Electrical Methods, in: *Non-Destructive Test. Eval. Civ. Eng. Struct.*,
2194 Elsevier, 2018: pp. 139–172. <https://doi.org/10.1016/B978-1-78548-229-8.50004-2>.
- 2195 [290] R.B. Polder, Test methods for on site measurement of resistivity of concrete — a RILEM TC-154
2196 technical recommendation, *Constr. Build. Mater.* 15 (2001) 125–131.
2197 [https://doi.org/10.1016/S0950-0618\(00\)00061-1](https://doi.org/10.1016/S0950-0618(00)00061-1).
- 2198 [291] P. Azarsa, R. Gupta, Electrical resistivity of concrete for durability evaluation: A review, *Adv.*
2199 *Mater. Sci. Eng.* 2017 (2017) 1–30. <https://doi.org/10.1155/2017/8453095>.
- 2200 [292] F. Presuel-Moreno, Y.-Y. Wu, Y. Liu, Effect of curing regime on concrete resistivity and aging
2201 factor over time, *Constr. Build. Mater.* 48 (2013) 874–882.
2202 <https://doi.org/10.1016/j.conbuildmat.2013.07.094>.
- 2203 [293] R. du Plooy, S. Palma Lopes, G. Villain, X. Dérobert, Development of a multi-ring resistivity cell
2204 and multi-electrode resistivity probe for investigation of cover concrete condition, *NDT E Int.*
2205 54 (2013) 27–36. <https://doi.org/10.1016/j.ndteint.2012.11.007>.
- 2206 [294] R. Spragg, C. Qiao, T. Barrett, J. Weiss, Assessing a concrete's resistance to chloride ion ingress
2207 using the formation factor, *Corros. Steel Concr. Struct.* (2016) 211–238.

- 2208 <https://doi.org/10.1016/B978-1-78242-381-2.00011-0>.
- 2209 [295] A.J. Garzon, J. Sanchez, C. Andrade, N. Rebolledo, E. Menéndez, J. Fulla, Modification of four
2210 point method to measure the concrete electrical resistivity in presence of reinforcing bars, *Cem.*
2211 *Concr. Compos.* 53 (2014) 249–257. <https://doi.org/10.1016/j.cemconcomp.2014.07.013>.
- 2212 [296] R. Polder, C. Andrade, B. Elsener, Ø. Vennesland, J. Gulikers, R. Weidert, M. Raupach, Test
2213 methods for on site measurement of resistivity of concrete, *Mater. Struct.* 33 (2000) 603–611.
2214 <https://doi.org/10.1007/BF02480599>.
- 2215 [297] H. Layssi, P. Ghods, A.R. Alizadeh, M. Salehi, Electrical resistivity of concrete: Concepts,
2216 applications, and measurement techniques, *Concr. Int.* (2015) 41–46.
- 2217 [298] W.J. Weiss, R.P. Spragg, O.B. Isgor, M.T. Ley, T. Van Dam, Toward performance specifications
2218 for concrete: Linking resistivity, RCPT and diffusion predictions using the formation factor for
2219 use in specifications, in: *High Tech Concr. Where Technol. Eng. Meet*, Springer International
2220 Publishing, Cham, 2018: pp. 2057–2065. https://doi.org/10.1007/978-3-319-59471-2_235.
- 2221 [299] W.J. Weiss, T.J. Barrett, C. Qiao, H. Todak, Toward a specification for transport properties of
2222 concrete based on the formation factor of a sealed specimen, *Adv. Civ. Eng. Mater.* 5 (2016)
2223 20160004. <https://doi.org/10.1520/ACEM20160004>.
- 2224 [300] R. He, H. Ma, R.B. Hafiz, C. Fu, X. Jin, J. He, Determining porosity and pore network connectivity
2225 of cement-based materials by a modified non-contact electrical resistivity measurement:
2226 Experiment and theory, *Mater. Des.* 156 (2018) 82–92.
2227 <https://doi.org/10.1016/j.matdes.2018.06.045>.
- 2228 [301] H. Sallehi, P. Ghods, O.B. Isgor, Formation factor of fresh cementitious pastes, *Cem. Concr.*
2229 *Compos.* 91 (2018) 174–188. <https://doi.org/10.1016/j.cemconcomp.2018.05.011>.
- 2230 [302] X. Lu, Application of the Nernst-Einstein equation to concrete, *Cem. Concr. Res.* 27 (1997) 293–
2231 302. [https://doi.org/10.1016/S0008-8846\(96\)00200-1](https://doi.org/10.1016/S0008-8846(96)00200-1).
- 2232 [303] K.A. Snyder, The relationship between the formation factor and the diffusion coefficient of
2233 porous materials saturated with concentrated electrolytes: theoretical and experimental
2234 considerations, *Concr. Sci. Eng.* 3 (2001).
- 2235 [304] K.A. Snyder, X. Feng, B.D. Keen, T.O. Mason, Estimating the electrical conductivity of cement
2236 paste pore solutions from OH⁻, K⁺ and Na⁺ concentrations, *Cem. Concr. Res.* 33 (2003) 793–
2237 798. [https://doi.org/10.1016/S0008-8846\(02\)01068-2](https://doi.org/10.1016/S0008-8846(02)01068-2).
- 2238 [305] D.P. Bentz, A virtual rapid chloride permeability test, *Cem. Concr. Compos.* 29 (2007) 723–731.
2239 <https://doi.org/10.1016/j.cemconcomp.2007.06.006>.
- 2240 [306] M. Tsui Chang, P. Suraneni, O.B. Isgor, D. Trejo, W.J. Weiss, Using X-ray fluorescence to assess
2241 the chemical composition and resistivity of simulated cementitious pore solutions, *Int. J. Adv.*
2242 *Eng. Sci. Appl. Math.* 9 (2017) 136–143. <https://doi.org/10.1007/s12572-017-0181-x>.
- 2243 [307] Y. Bu, D. Luo, J. Weiss, Using Fick's second law and Nernst-Planck approach in prediction of
2244 chloride ingress in concrete materials, *Adv. Civ. Eng. Mater.* 3 (2014) 20140018.
2245 <https://doi.org/10.1520/ACEM20140018>.
- 2246 [308] C.A.J. Appelo, Solute transport solved with the Nernst-Planck equation for concrete pores with
2247 'free' water and a double layer, *Cem. Concr. Res.* 101 (2017) 102–113.
2248 <https://doi.org/10.1016/j.cemconres.2017.08.030>.
- 2249 [309] C. Qiao, A.T. Coyle, O.B. Isgor, W.J. Weiss, Prediction of chloride ingress in saturated concrete
2250 using formation factor and chloride binding isotherm, *Adv. Civ. Eng. Mater.* 7 (2018) 20170141.

- 2251 <https://doi.org/10.1520/ACEM20170141>.
- 2252 [310] V. Jafari Azad, A.R. Erbehtas, C. Qiao, O.B. Isgor, W.J. Weiss, Relating the formation factor and
2253 chloride binding parameters to the apparent chloride diffusion coefficient of concrete, *J. Mater.*
2254 *Civ. Eng.* 31 (2019) 04018392. [https://doi.org/10.1061/\(ASCE\)MT.1943-5533.0002615](https://doi.org/10.1061/(ASCE)MT.1943-5533.0002615).
- 2255 [311] O. Sengul, Use of electrical resistivity as an indicator for durability, *Constr. Build. Mater.* 73
2256 (2014) 434–441. <https://doi.org/10.1016/j.conbuildmat.2014.09.077>.
- 2257 [312] M.K. Moradillo, C. Qiao, B. Isgor, S. Reese, W.J. Weiss, Relating formation factor of concrete to
2258 water absorption, *ACI Mater. J.* 115 (2018) 887–898. <https://doi.org/10.14359/51706844>.
- 2259 [313] O.B. Isgor, W.J. Weiss, A nearly self-sufficient framework for modelling reactive-transport
2260 processes in concrete, *Mater. Struct.* 52 (2019) 3. <https://doi.org/10.1617/s11527-018-1305-x>.
- 2261 [314] R. Spragg, C. Villani, K. Snyder, D. Bentz, J.W. Bullard, J. Weiss, Factors that influence electrical
2262 resistivity measurements in cementitious systems, *Transp. Res. Rec. J. Transp. Res. Board.* 2342
2263 (2013) 90–98. <https://doi.org/10.3141/2342-11>.
- 2264 [315] Y. Wang, Y. Xi, The effect of temperature on moisture transport in concrete, *Materials (Basel).*
2265 10 (2017) 926. <https://doi.org/10.3390/ma10080926>.
- 2266 [316] A. Aït-Mokhtar, R. Belarbi, F. Benboudjema, N. Burlion, B. Capra, M. Carcassès, J.B. Colliat, F.
2267 Cussigh, F. Deby, F. Jacquemot, T. De Larrard, J.F. Lataste, P. Le Bescop, M. Pierre, S. Poyet, P.
2268 Rougeau, T. Rougelot, A. Sellier, J. Séménadisse, J.M. Torrenti, A. Trabelsi, P. Turcry, H. Yanez-
2269 Godoy, Experimental investigation of the variability of concrete durability properties, *Cem.*
2270 *Concr. Res.* 45 (2013) 21–36. <https://doi.org/10.1016/j.cemconres.2012.11.002>.
- 2271 [317] B. Lothenbach, F. Winnefeld, C. Alder, E. Wieland, P. Lunk, Effect of temperature on the pore
2272 solution, microstructure and hydration products of Portland cement pastes, *Cem. Concr. Res.*
2273 37 (2007) 483–491. <https://doi.org/10.1016/j.cemconres.2006.11.016>.
- 2274 [318] Y. Liu, F.J. Presuel-Moreno, Normalization of temperature effect on concrete resistivity by
2275 method using Arrhenius law, *ACI Mater. J.* 111 (2014) 433–442.
2276 <https://doi.org/10.14359/51686725>.
- 2277 [319] P.A. Claisse, H.I. El-Sayad, I.G. Shaaban, Permeability and pore volume of carbonated concrete,
2278 *ACI Mater. J.* 96 (1999) 378–381. <https://doi.org/10.14359/636>.
- 2279 [320] U.M. Angst, B. Elsener, On the applicability of Wenner method for resistivity measurements of
2280 concrete, *ACI Mater. J.* 111 (2014) 661–672. <https://doi.org/10.14359/51686831>.
- 2281 [321] C.-T. Chen, J.-J. Chang, W. Yeih, The effects of specimen parameters on the resistivity of
2282 concrete, *Constr. Build. Mater.* 71 (2014) 35–43.
2283 <https://doi.org/10.1016/j.conbuildmat.2014.08.009>.
- 2284 [322] M. Salehi, P. Ghods, O.B. Isgor, Numerical study on the effect of cracking on surface resistivity
2285 of plain and reinforced concrete elements, *J. Mater. Civ. Eng.* 27 (2015) 04015053.
2286 [https://doi.org/10.1061/\(ASCE\)MT.1943-5533.0001328](https://doi.org/10.1061/(ASCE)MT.1943-5533.0001328).
- 2287 [323] Ł. Sadowski, New non-destructive method for linear polarisation resistance corrosion rate
2288 measurement, *Arch. Civ. Mech. Eng.* 10 (2010) 109–116. [https://doi.org/10.1016/S1644-9665\(12\)60053-3](https://doi.org/10.1016/S1644-9665(12)60053-3).
- 2290 [324] A.Q. Nguyen, G. Klysz, F. Deby, J.-P. Balayssac, Evaluation of water content gradient using a new
2291 configuration of linear array four-point probe for electrical resistivity measurement, *Cem.*
2292 *Concr. Compos.* 83 (2017) 308–322. <https://doi.org/10.1016/j.cemconcomp.2017.07.020>.

- 2293 [325] S.G. Millard, Reinforced concrete resistivity measurement techniques, *Proc. Inst. Civ. Eng.* 91
2294 (1991) 71–88. <https://doi.org/10.1680/iicep.1991.13583>.
- 2295 [326] K.R. Gowers, S.G. Millard, Measurement of concrete resistivity for assessment of corrosion
2296 severity of steel using Wenner technique, *ACI Mater. J.* 96 (1999) 536–541.
2297 <https://doi.org/10.14359/655>.
- 2298 [327] O. Sengul, O.E. Gjørsv, Effect of embedded steel on electrical resistivity measurements on
2299 concrete structures, *ACI Mater. J.* 106 (2009) 11–18. <https://doi.org/10.14359/56311>.
- 2300 [328] F. Presuel-Moreno, Y. Liu, Y.-Y. Wu, Numerical modeling of the effects of rebar presence and/or
2301 multilayered concrete resistivity on the apparent resistivity measured via the Wenner method,
2302 *Constr. Build. Mater.* 48 (2013) 16–25. <https://doi.org/10.1016/j.conbuildmat.2013.06.053>.
- 2303 [329] M. Salehi, P. Ghods, O. Burkan Isgor, Numerical investigation of the role of embedded
2304 reinforcement mesh on electrical resistivity measurements of concrete using the Wenner probe
2305 technique, *Mater. Struct.* 49 (2016) 301–316. <https://doi.org/10.1617/s11527-014-0498-x>.
- 2306 [330] W. Morris, E.I. Moreno, A.A. Sagüés, Practical evaluation of resistivity of concrete in test
2307 cylinders using a Wenner array probe, *Cem. Concr. Res.* 26 (1996) 1779–1787.
2308 [https://doi.org/10.1016/S0008-8846\(96\)00175-5](https://doi.org/10.1016/S0008-8846(96)00175-5).
- 2309 [331] O. Sengul, O.E. Gjørsv, Electrical resistivity measurements for quality control during concrete
2310 construction, *ACI Mater. J.* 105 (2008) 541–547. <https://doi.org/10.14359/20195>.
- 2311 [332] P. Ghosh, Q. Tran, Influence of parameters on surface resistivity of concrete, *Cem. Concr.*
2312 *Compos.* 62 (2015) 134–145. <https://doi.org/10.1016/j.cemconcomp.2015.06.003>.
- 2313 [333] J. Sanchez, C. Andrade, J. Torres, N. Rebolledo, J. Fullera, Determination of reinforced concrete
2314 durability with on-site resistivity measurements, *Mater. Struct.* 50 (2017) 41.
2315 <https://doi.org/10.1617/s11527-016-0884-7>.
- 2316 [334] K. Hornbostel, C.K. Larsen, M.R. Geiker, Relationship between concrete resistivity and corrosion
2317 rate – A literature review, *Cem. Concr. Compos.* 39 (2013) 60–72.
2318 <https://doi.org/10.1016/j.cemconcomp.2013.03.019>.
- 2319 [335] C. Alonso, C. Andrade, J.A. González, Relation between resistivity and corrosion rate of
2320 reinforcements in carbonated mortar made with several cement types, *Cem. Concr. Res.* 18
2321 (1988) 687–698. [https://doi.org/10.1016/0008-8846\(88\)90091-9](https://doi.org/10.1016/0008-8846(88)90091-9).
- 2322 [336] S. Feliu, J.A. González, S. Feliu, C. Andrade, Relationship between conductivity of concrete and
2323 corrosion of reinforcing bars, *Br. Corros. J.* 24 (1989) 195–198.
2324 <https://doi.org/10.1179/000705989798270027>.
- 2325 [337] B. Yu, J. Liu, Z. Chen, Probabilistic evaluation method for corrosion risk of steel reinforcement
2326 based on concrete resistivity, *Constr. Build. Mater.* 138 (2017) 101–113.
2327 <https://doi.org/10.1016/j.conbuildmat.2017.01.100>.
- 2328 [338] R.B. Figueira, Electrochemical sensors for monitoring the corrosion conditions of reinforced
2329 concrete structures: A review, *Appl. Sci.* 7 (2017) 1157. <https://doi.org/10.3390/app7111157>.
- 2330 [339] W. Morris, A. Vico, M. Vazquez, S.R. de Sanchez, Corrosion of reinforcing steel evaluated by
2331 means of concrete resistivity measurements, *Corros. Sci.* 44 (2002) 81–99.
2332 [https://doi.org/10.1016/S0010-938X\(01\)00033-6](https://doi.org/10.1016/S0010-938X(01)00033-6).
- 2333 [340] J. Gulikers, Theoretical considerations on the supposed linear relationship between concrete
2334 resistivity and corrosion rate of steel reinforcement, *Mater. Corros.* 56 (2005) 393–403.
2335 <https://doi.org/10.1002/maco.200403841>.

- 2336 [341] S. Ahmad, An experimental study on correlation between concrete resistivity and
 2337 reinforcement corrosion rate, *Anti-Corrosion Methods Mater.* 61 (2014) 158–165.
 2338 <https://doi.org/10.1108/ACMM-07-2013-1285>.
- 2339 [342] F. Akgul, Inspection and evaluation of a network of concrete bridges based on multiple NDT
 2340 techniques, *Struct. Infrastruct. Eng.* (2020) 1–20.
 2341 <https://doi.org/10.1080/15732479.2020.1790016>.
- 2342 [343] K. Hornbostel, B. Elsener, U.M. Angst, C.K. Larsen, M.R. Geiker, Limitations of the use of
 2343 concrete bulk resistivity as an indicator for the rate of chloride-induced macro-cell corrosion,
 2344 *Struct. Concr.* 18 (2017) 326–333. <https://doi.org/10.1002/suco.201500141>.
- 2345 [344] K. Hornbostel, U.M. Angst, B. Elsener, C.K. Larsen, M.R. Geiker, On the limitations of predicting
 2346 the ohmic resistance in a macro-cell in mortar from bulk resistivity measurements, *Cem. Concr.*
 2347 *Res.* 76 (2015) 147–158. <https://doi.org/10.1016/j.cemconres.2015.05.023>.
- 2348 [345] K. Hornbostel, U.M. Angst, B. Elsener, C.K. Larsen, M.R. Geiker, Influence of mortar resistivity
 2349 on the rate-limiting step of chloride-induced macro-cell corrosion of reinforcing steel, *Corros.*
 2350 *Sci.* 110 (2016) 46–56. <https://doi.org/10.1016/j.corsci.2016.04.011>.
- 2351 [346] A.T. Coyle, R.P. Spragg, P. Suraneni, A.N. Amirkhanian, W.J. Weiss, Comparison of linear
 2352 temperature corrections and activation energy temperature corrections for electrical resistivity
 2353 measurements of concrete, *Adv. Civ. Eng. Mater.* 7 (2018) 20170135.
 2354 <https://doi.org/10.1520/ACEM20170135>.
- 2355 [347] J.M. Deus, B. Díaz, L. Freire, X.R. Nóvoa, The electrochemical behaviour of steel rebars in
 2356 concrete: an electrochemical impedance spectroscopy study of the effect of temperature,
 2357 *Electrochim. Acta.* 131 (2014) 106–115. <https://doi.org/10.1016/j.electacta.2013.12.012>.
- 2358 [348] K. Reichling, M. Raupach, N. Klitzsch, Determination of the distribution of electrical resistivity
 2359 in reinforced concrete structures using electrical resistivity tomography, *Mater. Corros.* 66
 2360 (2015) 763–771. <https://doi.org/10.1002/maco.201407763>.
- 2361 [349] K. Karhunen, A. Seppänen, A. Lehtikoinen, P.J.M. Monteiro, J.P. Kaipio, Electrical resistance
 2362 tomography imaging of concrete, *Cem. Concr. Res.* 40 (2010) 137–145.
 2363 <https://doi.org/10.1016/j.cemconres.2009.08.023>.
- 2364 [350] M.H. Loke, Tutorial: 2-D and 3-D electrical imaging surveys, 2004. www.geoelectrical.com
 2365 (accessed July 13, 2018).
- 2366 [351] D. Smyl, Electrical tomography for characterizing transport properties in cement-based
 2367 materials: A review, *Constr. Build. Mater.* 244 (2020) 118299.
 2368 <https://doi.org/10.1016/j.conbuildmat.2020.118299>.
- 2369 [352] M.A. Alhadj, S. Palma-Lopes, G. Villain, Accounting for steel rebar effect on resistivity profiles in
 2370 view of reinforced concrete structure survey, *Constr. Build. Mater.* 223 (2019) 898–909.
 2371 <https://doi.org/10.1016/j.conbuildmat.2019.07.208>.
- 2372 [353] J. Priou, Y. Lecieux, M. Chevreuil, V. Gaillard, C. Lupi, D. Leduc, E. Rozière, R. Guyard, F. Schoefs,
 2373 In situ DC electrical resistivity mapping performed in a reinforced concrete wharf using
 2374 embedded sensors, *Constr. Build. Mater.* 211 (2019) 244–260.
 2375 <https://doi.org/10.1016/j.conbuildmat.2019.03.152>.
- 2376 [354] J. Badr, Y. Fargier, S. Palma-Lopes, F. Deby, J.-P. Balayssac, S. Delepine-Lesoille, L.-M. Cottineau,
 2377 G. Villain, Design and validation of a multi-electrode embedded sensor to monitor resistivity
 2378 profiles over depth in concrete, *Constr. Build. Mater.* 223 (2019) 310–321.
 2379 <https://doi.org/10.1016/j.conbuildmat.2019.06.226>.

- 2380 [355] M. Fares, G. Villain, S. Bonnet, S. Palma Lopes, B. Thauvin, M. Thiery, Determining chloride
2381 content profiles in concrete using an electrical resistivity tomography device, *Cem. Concr.*
2382 *Compos.* 94 (2018) 315–326. <https://doi.org/10.1016/j.cemconcomp.2018.08.001>.
- 2383 [356] S. Bonnet, J.-P. Balayssac, Combination of the Wenner resistivity meter and Torrent permeameter
2384 methods for assessing carbonation depth and saturation level of concrete, *Constr. Build. Mater.*
2385 188 (2018) 1149–1165. <https://doi.org/10.1016/j.conbuildmat.2018.07.151>.
- 2386 [357] D. Smyl, M. Hallaji, A. Seppänen, M. Pour-Ghaz, Three-dimensional electrical impedance
2387 tomography to monitor unsaturated moisture ingress in cement-based materials, *Transp.*
2388 *Porous Media.* 115 (2016) 101–124. <https://doi.org/10.1007/s11242-016-0756-1>.
- 2389 [358] D. Smyl, R. Rashetnia, A. Seppänen, M. Pour-Ghaz, Can electrical resistance tomography be
2390 used for imaging unsaturated moisture flow in cement-based materials with discrete cracks?,
2391 *Cem. Concr. Res.* 91 (2017) 61–72. <https://doi.org/10.1016/j.cemconres.2016.10.009>.
- 2392 [359] E. V. Pereira, M.M. Salta, I.T.E. Fonseca, On the measurement of the polarisation resistance of
2393 reinforcing steel with embedded sensors: A comparative study, *Mater. Corros.* 66 (2015) 1029–
2394 1038. <https://doi.org/10.1002/maco.201407910>.
- 2395 [360] C. Andrade, L. Soler, C. Alonso, X.R. Nóvoa, M. Keddad, The importance of geometrical
2396 considerations in the measurement of steel corrosion in concrete by means of AC impedance,
2397 *Corros. Sci.* 37 (1995) 2013–2023. [https://doi.org/10.1016/0010-938X\(95\)00095-2](https://doi.org/10.1016/0010-938X(95)00095-2).
- 2398 [361] S. Rengaraju, L. Neelakantan, R.G. Pillai, Investigation on the polarization resistance of steel
2399 embedded in highly resistive cementitious systems – An attempt and challenges, *Electrochim.*
2400 *Acta.* 308 (2019) 131–141. <https://doi.org/10.1016/j.electacta.2019.03.200>.
- 2401 [362] O.B. Isgor, U. Angst, M. Geiker, C. Halmen, C. Hansson, J. Pacheco, D. Tepke, D. Trejo, P. Vaddey,
2402 Recommended practice for reporting experimental data produced from studies on corrosion of
2403 steel in cementitious systems, *RILEM Tech. Lett.* 4 (2019) 22–32.
2404 <https://doi.org/10.21809/rilemtechlett.2019.90>.
- 2405 [363] M. Stern, A.L. Geary, Electrochemical polarization, *J. Electrochem. Soc.* 104 (1957) 56.
2406 <https://doi.org/10.1149/1.2428496>.
- 2407 [364] A. Guyader, F. Huet, R.P. Nogueira, Polarization resistance measurements: Potentiostatically or
2408 galvanostatically?, *Corrosion.* 65 (2009) 136–144. <https://doi.org/10.5006/1.3319118>.
- 2409 [365] S. Ahmad, B. Bhattacharjee, A simple arrangement and procedure for in-situ measurement of
2410 corrosion rate of rebar embedded in concrete, *Corros. Sci.* 37 (1995) 781–791.
2411 [https://doi.org/10.1016/0010-938X\(95\)80008-5](https://doi.org/10.1016/0010-938X(95)80008-5).
- 2412 [366] A. Fahim, P. Ghods, O.B. Isgor, M.D.A. Thomas, A critical examination of corrosion rate
2413 measurement techniques applied to reinforcing steel in concrete, *Mater. Corros.* 69 (2018)
2414 1784–1799. <https://doi.org/10.1002/maco.201810263>.
- 2415 [367] A.A. Sagüés, S.C. Kranc, E.I. Moreno, The time-domain response of a corroding system with
2416 constant phase angle interfacial component: Application to steel in concrete, *Corros. Sci.* 37
2417 (1995) 1097–1113. [https://doi.org/10.1016/0010-938X\(95\)00017-E](https://doi.org/10.1016/0010-938X(95)00017-E).
- 2418 [368] C.J. Newton, J.M. Sykes, A galvanostatic pulse technique for investigation of steel corrosion in
2419 concrete, *Corros. Sci.* 28 (1988) 1051–1074. [https://doi.org/10.1016/0010-938X\(88\)90101-1](https://doi.org/10.1016/0010-938X(88)90101-1).
- 2420 [369] B. Elsener, O. Klinghoffer, T. Frolund, E. Rislund, Y. Schiegg, H. Böhni, Assessment of
2421 reinforcement corrosion by means of galvanostatic pulse technique, in: *Repair Concr. Struct.*,
2422 *Svolvær, Norway, 1997*: pp. 391–400.

- 2423 [370] A. Poursaee, Potentiostatic transient technique, a simple approach to estimate the corrosion
2424 current density and Stern–Geary constant of reinforcing steel in concrete, *Cem. Concr. Res.* 40
2425 (2010) 1451–1458. <https://doi.org/10.1016/j.cemconres.2010.04.006>.
- 2426 [371] J.E. Ramón, J.M. Gandía-Romero, R. Bataller, M. Alcañiz, M. Valcuende, J. Soto, Potential step
2427 voltammetry: an approach for corrosion rate measurement of reinforcements in concrete,
2428 *Cem. Concr. Compos.* (2020) 103590. <https://doi.org/10.1016/j.cemconcomp.2020.103590>.
- 2429 [372] D.M. Bastidas, J.A. González, S. Feliu, A. Cobo, J.M. Miranda, A quantitative study of concrete-
2430 embedded steel corrosion using potentiostatic pulses, *Corrosion.* 63 (2007) 1094–1100.
2431 <https://doi.org/10.5006/1.3278327>.
- 2432 [373] P. Rodrí, J.A. González, Use of the coulostatic method for measuring corrosion rates of
2433 embedded metal in concrete, *Mag. Concr. Res.* 46 (1994) 91–97.
2434 <https://doi.org/10.1680/mac.1994.46.167.91>.
- 2435 [374] G.K. Glass, An assessment of the coulostatic method applied to the corrosion of steel in
2436 concrete, *Corros. Sci.* 37 (1995) 597–605. [https://doi.org/10.1016/0010-938X\(94\)00156-Z](https://doi.org/10.1016/0010-938X(94)00156-Z).
- 2437 [375] V. Feliu, J.A. González, S. Feliu, Modelling of the steel-concrete interface to obtain information
2438 on reinforcement bar corrosion, *J. Appl. Electrochem.* 35 (2005) 429–436.
2439 <https://doi.org/10.1007/s10800-004-8348-0>.
- 2440 [376] S. Feliu, J.A. González, M.L. Escudero, S. Feliu, M.C. Andrade, Possibilities of the guard ring for
2441 electrical signal confinement in the polarization measurements of reinforcements, *Corrosion.*
2442 46 (1990) 1015–1020. <https://doi.org/10.5006/1.3585049>.
- 2443 [377] A. Fahim, Corrosion of reinforcing steel in concrete: monitoring techniques and mitigation
2444 strategies, University of New Brunswick, 2018.
- 2445 [378] P. V. Nygaard, M.R. Geiker, Measuring the corrosion rate of steel in concrete - effect of
2446 measurement technique, polarisation time and current, *Mater. Corros.* 63 (2012) 200–214.
2447 <https://doi.org/10.1002/maco.201005792>.
- 2448 [379] S. Laurens, P. Hénocq, N. Rouleau, F. Deby, E. Samson, J. Marchand, B. Bissonnette, Steady-
2449 state polarization response of chloride-induced macrocell corrosion systems in steel reinforced
2450 concrete — numerical and experimental investigations, *Cem. Concr. Res.* 79 (2016) 272–290.
2451 <https://doi.org/10.1016/j.cemconres.2015.09.021>.
- 2452 [380] U. Angst, M. Büchler, A new perspective on measuring the corrosion rate of localized corrosion,
2453 *Mater. Corros.* 71 (2020) 808–823. <https://doi.org/10.1002/maco.201911467>.
- 2454 [381] D.G. John, P.C. Searson, J.L. Dawson, Use of AC impedance technique in studies on steel in
2455 concrete in immersed conditions, *Br. Corros. J.* 16 (1981) 102–106.
2456 <https://doi.org/10.1179/000705981798275002>.
- 2457 [382] M.E. Orazem, B. Tribollet, *Electrochemical Impedance Spectroscopy*, 2nd Edition, Wiley, 2017.
- 2458 [383] D. V. Ribeiro, J.C.C. Abrantes, Application of electrochemical impedance spectroscopy (EIS) to
2459 monitor the corrosion of reinforced concrete: A new approach, *Constr. Build. Mater.* 111 (2016)
2460 98–104. <https://doi.org/10.1016/j.conbuildmat.2016.02.047>.
- 2461 [384] G. Liu, Y. Zhang, M. Wu, R. Huang, Study of depassivation of carbon steel in simulated concrete
2462 pore solution using different equivalent circuits, *Constr. Build. Mater.* 157 (2017) 357–362.
2463 <https://doi.org/10.1016/j.conbuildmat.2017.09.104>.
- 2464 [385] J.-P. Diard, B. Le Gorrec, C. Montella, *Handbook of Electrochemical Impedance Spectroscopy -*
2465 *Electrical Circuits Containing CPEs*, 2013.

- 2466 [386] M.E. Orazem, B. Tribollet, Electrical Circuits, in: *Electrochem. Impedance Spectrosc.*, John Wiley
2467 & Sons, Inc., Hoboken, NJ, USA, 2017: pp. 75–88. <https://doi.org/10.1002/9781119363682.ch4>.
- 2468 [387] M.E. Orazem, B. Tribollet, Equivalent Circuit Analogs, in: *Electrochem. Impedance Spectrosc.*,
2469 John Wiley & Sons, Inc., Hoboken, NJ, USA, 2017: pp. 191–206.
2470 <https://doi.org/10.1002/9781119363682.ch9>.
- 2471 [388] M.E. Orazem, B. Tribollet, Constant-Phase Elements, in: *Electrochem. Impedance Spectrosc.*,
2472 John Wiley & Sons, Inc., Hoboken, NJ, USA, 2017: pp. 395–419.
2473 <https://doi.org/10.1002/9781119363682.ch14>.
- 2474 [389] M.R. Shoar Abouzari, F. Berkemeier, G. Schmitz, D. Wilmer, On the physical interpretation of
2475 constant phase elements, *Solid State Ionics*. 180 (2009) 922–927.
2476 <https://doi.org/10.1016/j.ssi.2009.04.002>.
- 2477 [390] M. Keddad, H. Takenouti, X.R. Nóvoa, C. Andrade, C. Alonso, Impedance measurements on
2478 cement paste, *Cem. Concr. Res.* 27 (1997) 1191–1201. [https://doi.org/10.1016/S0008-
2479 8846\(97\)00117-8](https://doi.org/10.1016/S0008-8846(97)00117-8).
- 2480 [391] Z. Xu, P. Gu, P. Xie, J.J. Beaudoin, Application of A.C. impedance techniques in studies of porous
2481 cementitious materials: (II): Relationship between ACIS behavior and the porous
2482 microstructure, *Cem. Concr. Res.* 23 (1993) 853–862. [https://doi.org/10.1016/0008-
2483 8846\(93\)90039-C](https://doi.org/10.1016/0008-8846(93)90039-C).
- 2484 [392] X. Hu, C. Shi, X. Liu, J. Zhang, G. de Schutter, A review on microstructural characterization of
2485 cement-based materials by AC impedance spectroscopy, *Cem. Concr. Compos.* 100 (2019) 1–
2486 14. <https://doi.org/10.1016/j.cemconcomp.2019.03.018>.
- 2487 [393] B. Díaz, X.R. Nóvoa, M.C. Pérez, Study of the chloride diffusion in mortar: A new method of
2488 determining diffusion coefficients based on impedance measurements, *Cem. Concr. Compos.*
2489 28 (2006) 237–245. <https://doi.org/10.1016/j.cemconsomp.2006.01.009>.
- 2490 [394] I. Sánchez, M.P. López, J.M. Ortega, M.Á. Climent, Impedance spectroscopy: An efficient tool to
2491 determine the non-steady-state chloride diffusion coefficient in building materials, *Mater.*
2492 *Corros.* 62 (2011) 139–145. <https://doi.org/10.1002/maco.201005775>.
- 2493 [395] H. Mercado-Mendoza, S. Lorente, X. Bourbon, The diffusion coefficient of ionic species through
2494 unsaturated materials, *Transp. Porous Media.* 96 (2013) 469–481.
2495 <https://doi.org/10.1007/s11242-012-0100-3>.
- 2496 [396] S. Chakri, I. Frateur, M.E. Orazem, E.M.M. Sutter, T.T.M. Tran, B. Tribollet, V. Vivier, Improved
2497 EIS analysis of the electrochemical behaviour of carbon steel in alkaline solution, *Electrochim.*
2498 *Acta.* 246 (2017) 924–930. <https://doi.org/10.1016/j.electacta.2017.06.096>.
- 2499 [397] R. Vedalakshmi, S. Manoharan, H.-W. Song, N. Palaniswamy, Application of harmonic analysis
2500 in measuring the corrosion rate of rebar in concrete, *Corros. Sci.* 51 (2009) 2777–2789.
2501 <https://doi.org/10.1016/j.corsci.2009.07.014>.
- 2502 [398] U.M. Angst, B. Elsener, Measuring corrosion rates: A novel AC method based on processing and
2503 analysing signals recorded in the time domain, *Corros. Sci.* 89 (2014) 307–317.
2504 <https://doi.org/10.1016/j.corsci.2014.09.013>.
- 2505 [399] H. Wojtas, Determination of corrosion rate of reinforcement with a modulated guard ring
2506 electrode; analysis of errors due to lateral current distribution, *Corros. Sci.* 46 (2004) 1621–
2507 1632. <https://doi.org/10.1016/j.corsci.2003.10.007>.
- 2508 [400] S. Feliu, J.A. González, J.M. Miranda, V. Feliu, Possibilities and problems of in situ techniques

- 2509 for measuring steel corrosion rates in large reinforced concrete structures, *Corros. Sci.* 47
2510 (2005) 217–238. <https://doi.org/10.1016/j.corsci.2004.04.011>.
- 2511 [401] A. Poursaeed, C.M. Hansson, Galvanostatic pulse technique with the current confinement guard
2512 ring: The laboratory and finite element analysis, *Corros. Sci.* 50 (2008) 2739–2746.
2513 <https://doi.org/10.1016/j.corsci.2008.07.017>.
- 2514 [402] P. V. Nygaard, M.R. Geiker, B. Elsener, Corrosion rate of steel in concrete: evaluation of
2515 confinement techniques for on-site corrosion rate measurements, *Mater. Struct.* 42 (2009)
2516 1059–1076. <https://doi.org/10.1617/s11527-008-9443-1>.
- 2517 [403] A. Clément, S. Laurens, G. Arliguie, F. Deby, Numerical study of the linear polarisation resistance
2518 technique applied to reinforced concrete for corrosion assessment, *Eur. J. Environ. Civ. Eng.* 16
2519 (2012) 491–504. <https://doi.org/10.1080/19648189.2012.668012>.
- 2520 [404] O. Gepreags, C. Hansson, A comparative evaluation of three commercial instruments for field
2521 measurements of reinforcing steel corrosion rates, *J. ASTM Int.* (2005).
2522 <https://doi.org/10.1520/JAI11789>.
- 2523 [405] J. Marchand, S. Laurens, Y. Protière, E. Samson, A numerical study of polarization tests applied
2524 to corrosion in reinforced concrete, *Spec. Publ.* 312 (2016) 1–12.
- 2525 [406] J. Zhang, P.J.M. Monteiro, H.F. Morrison, Noninvasive surface measurement of corrosion
2526 impedance of reinforcing bar in concrete—Part 1: Experimental results, *ACI Mater. J.* 98 (2001)
2527 116–125. <https://doi.org/10.14359/10195>.
- 2528 [407] S.S. Hubbard, J. Zhang, P.J.M. Monteiro, J.E. Peterson, Y. Rubin, Experimental detection of
2529 reinforcing bar corrosion using nondestructive geophysical techniques, *ACI Mater. J.* 100 (2003)
2530 501–510. <https://doi.org/10.14359/12957>.
- 2531 [408] P.J.M. Monteiro, F. Morrison, W. Frangos, Non-destructive measurement of corrosion state of
2532 reinforcing steel in concrete, *ACI Mater. J.* 95 (1998) 704–709. <https://doi.org/10.14359/414>.
- 2533 [409] J. Zhang, P.J.M. Monteiro, H.F. Morrison, Noninvasive surface measurement of corrosion
2534 impedance of reinforcing bar in concrete—Part 2: Forward modeling, *ACI Mater. J.* 99 (2002)
2535 242–249. <https://doi.org/10.14359/11969>.
- 2536 [410] J. Zhang, P.J.M. Monteiro, H.F. Morrison, M. Mancio, Noninvasive surface measurement of
2537 corrosion impedance of reinforcing bar in concrete—Part 3: Effect of geometry and material
2538 properties, *ACI Mater. J.* 101 (2004) 273–280.
- 2539 [411] A. Fahim, P. Ghods, R. Alizaded, M. Salehi, S. Decarufel, CEPRA: A new test method for rebar
2540 corrosion rate measurement, *Adv. Electrochem. Tech. Corros. Monit. Lab. Corros. Meas.*
2541 *STP1609* (2019) 59–80. <https://doi.org/10.1520/STP160920170227>.
- 2542 [412] Y.-C. Lim, T. Noguchi, S.-W. Shin, Formulation of a nondestructive technique for evaluating steel
2543 corrosion in concrete structures, *ISIJ Int.* 49 (2009) 275–283.
2544 <https://doi.org/10.2355/isijinternational.49.275>.
- 2545 [413] Y.-C. Lim, T. Noguchi, S. Shin, Corrosion evaluation by estimating the surface resistivity of
2546 reinforcing bar, *J. Adv. Concr. Technol.* 8 (2010) 113–119. <https://doi.org/10.3151/jact.8.113>.
- 2547 [414] C. Andrade, I. Martínez, M. Castellote, Feasibility of determining corrosion rates by means of
2548 stray current-induced polarisation, *J. Appl. Electrochem.* 38 (2008) 1467–1476.
2549 <https://doi.org/10.1007/s10800-008-9591-6>.
- 2550 [415] C. Andrade, I. Martínez, Metal corrosion rate determination of different solutions and
2551 reinforced concrete specimens by means of a noncontacting corrosion method, *Corrosion.* 66

- 2552 (2010) 056001-056001–10. <https://doi.org/10.5006/1.3430465>.
- 2553 [416] C. Andrade, J. Sanchez, I. Martinez, N. Rebolledo, Analogue circuit of the inductive polarization
2554 resistance, *Electrochim. Acta.* 56 (2011) 1874–1880.
2555 <https://doi.org/10.1016/j.electacta.2010.09.057>.
- 2556 [417] M. Keddam, X.R. Nóvoa, V. Vivier, The concept of floating electrode for contact-less
2557 electrochemical measurements: Application to reinforcing steel-bar corrosion in concrete,
2558 *Corros. Sci.* 51 (2009) 1795–1801. <https://doi.org/10.1016/j.corsci.2009.05.006>.
- 2559 [418] M. Keddam, X.R. Nóvoa, B. Puga, V. Vivier, Impedance based method for non-contact
2560 determination of the corrosion rate in buried metallic structures, *Eur. J. Environ. Civ. Eng.* 15
2561 (2011) 1097–1103. <https://doi.org/10.1080/19648189.2011.9695296>.
- 2562 [419] J. Yu, A. Sasamoto, M. Iwata, Wenner method of impedance measurement for health evaluation
2563 of reinforced concrete structures, *Constr. Build. Mater.* 197 (2019) 576–586.
2564 <https://doi.org/10.1016/j.conbuildmat.2018.11.121>.
- 2565 [420] C.L. Alexander, M.E. Orazem, Indirect electrochemical impedance spectroscopy for corrosion
2566 detection in external post-tensioned tendons: 1. Proof of concept, *Corros. Sci.* 164 (2020)
2567 108331. <https://doi.org/10.1016/j.corsci.2019.108331>.
- 2568 [421] C.L. Alexander, M.E. Orazem, Indirect impedance for corrosion detection of external post-
2569 tensioned tendons: 2. Multiple steel strands, *Corros. Sci.* 164 (2020) 108330.
2570 <https://doi.org/10.1016/j.corsci.2019.108330>.
- 2571 [422] F. Abdulsamad, N. Florsch, Assessing the high frequency behavior of non-polarizable electrodes
2572 for spectral induced polarization measurements, *J. Appl. Geophys.* 135 (2016) 449–455.
2573 <https://doi.org/10.1016/j.jappgeo.2016.01.001>.
- 2574 [423] C.L. Alexander, Impedance spectroscopy: The influence of surface heterogeneity and
2575 application to corrosion monitoring of bridge tendons, University of Florida, 2017.
- 2576 [424] R. Rodrigues, J. Gance, S. Gaboreau, I. Ignatiadis, S. Betelu, Electrochemical Measurement
2577 System and Method for Monitoring a Concrete Structure, EP19188380, 2019.
- 2578 [425] C. Andrade, J.A. González, Quantitative measurements of corrosion rate of reinforcing steels
2579 embedded in concrete using polarization resistance measurements, *Mater. Corros.* 29 (1978)
2580 515–519. <https://doi.org/10.1002/maco.19780290804>.
- 2581 [426] G. Song, Theoretical analysis of the measurement of polarisation resistance in reinforced
2582 concrete, *Cem. Concr. Compos.* 22 (2000) 407–415. [https://doi.org/10.1016/S0958-9465\(00\)00040-8](https://doi.org/10.1016/S0958-9465(00)00040-8).
- 2584 [427] C. Alonso, C. Andrade, X.R. Nóvoa, M. Izquierdo, M.C. Pérez, Effect of protective oxide scales in
2585 the macrogalvanic behaviour of concrete reinforcements, *Corros. Sci.* 40 (1998) 1379–1389.
2586 [https://doi.org/10.1016/S0010-938X\(98\)00040-7](https://doi.org/10.1016/S0010-938X(98)00040-7).
- 2587 [428] D.A. Jones, N.D. Greene, Electrochemical measurement of low corrosion rates, *Corrosion.* 22
2588 (1966) 198–205. <https://doi.org/10.5006/0010-9312-22.7.198>.
- 2589 [429] D.A. Jones, Principles and Prevention of Corrosion, 2nd Edition, Prentice Hall, Upper Saddle
2590 River, N.J., 1996.
- 2591 [430] E. Gileadi, E. Kirowa-Eisner, Some observations concerning the Tafel equation and its relevance
2592 to charge transfer in corrosion, *Corros. Sci.* 47 (2005) 3068–3085.
2593 <https://doi.org/10.1016/j.corsci.2005.05.044>.

- 2594 [431] J. Ge, O.B. Isgor, Effects of Tafel slope, exchange current density and electrode potential on the
 2595 corrosion of steel in concrete, *Mater. Corros.* 58 (2007) 573–582.
 2596 <https://doi.org/10.1002/maco.200604043>.
- 2597 [432] J.A. González, J.M. Miranda, N. Birbilis, S. Feliu, Electrochemical techniques for studying
 2598 corrosion of reinforcing steel: Limitations and advantages, *Corrosion*. 61 (2005) 37–50.
 2599 <https://doi.org/10.5006/1.3278158>.
- 2600 [433] B. Yu, L. Yang, M. Wu, B. Li, Practical model for predicting corrosion rate of steel reinforcement
 2601 in concrete structures, *Constr. Build. Mater.* 54 (2014) 385–401.
 2602 <https://doi.org/10.1016/j.conbuildmat.2013.12.046>.
- 2603 [434] J.A. González, A. Molina, M.L. Escudero, C. Andrade, Errors in the electrochemical evaluation of
 2604 very small corrosion rates—I. Polarization resistance method applied to corrosion of steel in
 2605 concrete, *Corros. Sci.* 25 (1985) 917–930. [https://doi.org/10.1016/0010-938X\(85\)90021-6](https://doi.org/10.1016/0010-938X(85)90021-6).
- 2606 [435] I. Martínez, C. Andrade, Polarization resistance measurements of bars embedded in concrete
 2607 with different chloride concentrations: EIS and DC comparison, *Mater. Corros.* 62 (2011) 932–
 2608 942. <https://doi.org/10.1002/maco.200905596>.
- 2609 [436] J.A. González, A. Molina, M.L. Escudero, C. Andrade, Errors in the electrochemical evaluation of
 2610 very small corrosion rates—II. Other electrochemical techniques applied to corrosion of steel
 2611 in concrete, *Corros. Sci.* 25 (1985) 519–530. [https://doi.org/10.1016/0010-938X\(85\)90030-7](https://doi.org/10.1016/0010-938X(85)90030-7).
- 2612 [437] M. Kouřil, P. Novák, M. Bojko, Limitations of the linear polarization method to determine
 2613 stainless steel corrosion rate in concrete environment, *Cem. Concr. Compos.* 28 (2006) 220–
 2614 225. <https://doi.org/10.1016/j.cemconcomp.2006.01.007>.
- 2615 [438] U. Angst, M. Büchler, On the applicability of the Stern-Geary relationship to determine
 2616 instantaneous corrosion rates in macro-cell corrosion, *Mater. Corros.* 66 (2015) 1017–1028.
 2617 <https://doi.org/10.1002/maco.201407997>.
- 2618 [439] B. Elsener, Corrosion rate of steel in concrete—Measurements beyond the Tafel law, *Corros.*
 2619 *Sci.* 47 (2005) 3019–3033. <https://doi.org/10.1016/j.corsci.2005.06.021>.
- 2620 [440] C. Andrade, C. Alonso, J. Sarría, Corrosion rate evolution in concrete structures exposed to the
 2621 atmosphere, *Cem. Concr. Compos.* 24 (2002) 55–64. [https://doi.org/10.1016/S0958-9465\(01\)00026-9](https://doi.org/10.1016/S0958-9465(01)00026-9).
- 2622
- 2623 [441] C. Andrade, Propagation of reinforcement corrosion: principles, testing and modelling, *Mater.*
 2624 *Struct.* 52 (2019) 2. <https://doi.org/10.1617/s11527-018-1301-1>.
- 2625 [442] C. Andrade, J. Sarría, C. Alonso, Relative humidity in the interior of concrete exposed to natural
 2626 and artificial weathering, *Cem. Concr. Res.* 29 (1999) 1249–1259.
 2627 [https://doi.org/10.1016/S0008-8846\(99\)00123-4](https://doi.org/10.1016/S0008-8846(99)00123-4).
- 2628 [443] J. Jiang, Y. Yuan, Development and prediction strategy of steel corrosion rate in concrete under
 2629 natural climate, *Constr. Build. Mater.* 44 (2013) 287–292.
 2630 <https://doi.org/10.1016/j.conbuildmat.2013.03.033>.
- 2631 [444] T. Jaśniok, M. Jaśniok, Influence of rapid changes of moisture content in concrete and
 2632 temperature on corrosion rate of reinforcing steel, *Procedia Eng.* 108 (2015) 316–323.
 2633 <https://doi.org/10.1016/j.proeng.2015.06.153>.
- 2634 [445] C. Andrade, A. Castillo, Evolution of reinforcement corrosion due to climatic variations, *Mater.*
 2635 *Corros.* 54 (2003) 379–386. <https://doi.org/10.1002/maco.200390087>.
- 2636 [446] C. Boschmann Käthler, U.M. Angst, G. Ebell, B. Elsener, Chloride-induced reinforcement

- 2637 corrosion in cracked concrete: the influence of time of wetness on corrosion propagation,
2638 *Corros. Eng. Sci. Technol.* (2020) 1–10. <https://doi.org/10.1080/1478422X.2020.1789371>.
- 2639 [447] V. Bouteiller, J.-F. Cherrier, V. L’Hostis, N. Rebolledo, C. Andrade, E. Marie-Victoire, Influence of
2640 humidity and temperature on the corrosion of reinforced concrete prisms, *Eur. J. Environ. Civ.*
2641 *Eng.* 16 (2012) 471–480. <https://doi.org/10.1080/19648189.2012.668004>.
- 2642 [448] B. Yu, J. Liu, B. Li, Improved numerical model for steel reinforcement corrosion in concrete
2643 considering influences of temperature and relative humidity, *Constr. Build. Mater.* 142 (2017)
2644 175–186. <https://doi.org/10.1016/j.conbuildmat.2017.03.045>.
- 2645 [449] A. Chauhan, U.K. Sharma, Influence of temperature and relative humidity variations on non-
2646 uniform corrosion of reinforced concrete, *Structures.* 19 (2019) 296–308.
2647 <https://doi.org/10.1016/j.istruc.2019.01.016>.
- 2648 [450] Y.A. Villagrán Zaccardi, A. Bértora, A.A. Di Maio, Temperature and humidity influences on the
2649 on-site active marine corrosion of reinforced concrete elements, *Mater. Struct.* 46 (2013) 1527–
2650 1535. <https://doi.org/10.1617/s11527-012-9994-z>.
- 2651 [451] V. Bouteiller, E. Marie-Victoire, C. Cremona, Mathematical relation of steel thickness loss with
2652 time related to reinforced concrete contaminated by chlorides, *Constr. Build. Mater.* 124 (2016)
2653 764–775. <https://doi.org/10.1016/j.conbuildmat.2016.07.078>.
- 2654 [452] A. Michel, P.V. Nygaard, M.R. Geiker, Experimental investigation on the short-term impact of
2655 temperature and moisture on reinforcement corrosion, *Corros. Sci.* 72 (2013) 26–34.
2656 <https://doi.org/10.1016/j.corsci.2013.02.006>.
- 2657 [453] U.M. Angst, Durable concrete structures: Cracks & corrosion and corrosion & cracks, in: G.
2658 Pijaudier-Cabot, P. Grassl, C. La Borderi (Eds.), 10th Int. Conf. Fract. Mech. Concr. Concr. Struct.,
2659 Bayonne, France, 2019: pp. 1–10. <https://doi.org/10.21012/FC10.233307>.
- 2660 [454] M. Jaśniok, T. Jaśniok, Evaluation of maximum and minimum corrosion rate of steel rebars in
2661 concrete structures, based on laboratory measurements on drilled cores, *Procedia Eng.* 193
2662 (2017) 486–493. <https://doi.org/10.1016/j.proeng.2017.06.241>.
- 2663 [455] D. Breyse, G. Klysz, X. Dérobert, C. Sirieix, J.F. Lataste, How to combine several non-destructive
2664 techniques for a better assessment of concrete structures, *Cem. Concr. Res.* 38 (2008) 783–793.
2665 <https://doi.org/10.1016/j.cemconres.2008.01.016>.
- 2666 [456] G. Loreto, M. Di Benedetti, A. De Luca, A. Nanni, Assessment of reinforced concrete structures
2667 in marine environment: a case study, *Corros. Rev.* 37 (2019) 57–69.
2668 <https://doi.org/10.1515/corrrev-2018-0046>.
- 2669 [457] L. Sadowski, Methodology for assessing the probability of corrosion in concrete structures on
2670 the basis of half-cell potential and concrete resistivity measurements, *Sci. World J.* 2013 (2013)
2671 714501. <https://doi.org/10.1155/2013/714501>.
- 2672 [458] V. Garnier, B. Piwakowski, O. Abraham, G. Villain, C. Payan, J.F. Chaix, Acoustic techniques for
2673 concrete evaluation: Improvements, comparisons and consistency, *Constr. Build. Mater.* 43
2674 (2013) 598–613. <https://doi.org/10.1016/j.conbuildmat.2013.01.035>.
- 2675 [459] P. Ziehl, M. ElBatanouny, Acoustic emission monitoring for corrosion damage detection and
2676 classification, in: *Corros. Steel Concr. Struct.*, Woodhead Publishing, 2016: pp. 193–209.
2677 <https://doi.org/10.1016/B978-1-78242-381-2.00010-9>.
- 2678 [460] C. Van Steen, L. Pahlavan, M. Wevers, E. Verstrynge, Localisation and characterisation of
2679 corrosion damage in reinforced concrete by means of acoustic emission and X-ray computed

- 2680 tomography, *Constr. Build. Mater.* 197 (2019) 21–29.
2681 <https://doi.org/10.1016/j.conbuildmat.2018.11.159>.
- 2682 [461] M.R. Clark, D.M. McCann, M.C. Forde, Application of infrared thermography to the non-
2683 destructive testing of concrete and masonry bridges, *NDT E Int.* 36 (2003) 265–275.
2684 [https://doi.org/10.1016/S0963-8695\(02\)00060-9](https://doi.org/10.1016/S0963-8695(02)00060-9).
- 2685 [462] X. Dérobert, Z.M. Sbartai, J. Dumoulin, Electromagnetic Methods, in: *Non-Destructive Test.*
2686 *Eval. Civ. Eng. Struct.*, Elsevier, 2018: pp. 87–137. <https://doi.org/10.1016/B978-1-78548-229-8.50003-0>.
2687
- 2688 [463] W. Wai-Lok Lai, X. Dérobert, P. Annan, A review of ground penetrating radar application in civil
2689 engineering: A 30-year journey from locating and testing to imaging and diagnosis, *NDT E Int.*
2690 96 (2018) 58–78. <https://doi.org/10.1016/j.ndteint.2017.04.002>.
- 2691 [464] F. Tosti, C. Ferrante, Using ground penetrating radar methods to investigate reinforced
2692 concrete structures, *Surv. Geophys.* (2019) 1–46. <https://doi.org/10.1007/s10712-019-09565-5>.
2693
- 2694 [465] X. Dérobert, J. Iaquina, G. Klysz, J.-P. Balayssac, Use of capacitive and GPR techniques for the
2695 non-destructive evaluation of cover concrete, *NDT E Int.* 41 (2008) 44–52.
2696 <https://doi.org/10.1016/j.ndteint.2007.06.004>.
- 2697 [466] S. Hong, H. Wiggenhauser, R. Helmerich, B. Dong, P. Dong, F. Xing, Long-term monitoring of
2698 reinforcement corrosion in concrete using ground penetrating radar, *Corros. Sci.* 114 (2017)
2699 123–132. <https://doi.org/10.1016/j.corsci.2016.11.003>.
- 2700 [467] M. Fares, Y. Fargier, G. Villain, X. Derobert, S. Palma Lopes, Determining the permittivity profile
2701 inside reinforced concrete using capacitive probes, *NDT E Int.* 79 (2016) 150–161.
2702 <https://doi.org/10.1016/j.ndteint.2016.01.002>.
- 2703 [468] A. Voss, P. Hosseini, M. Pour-Ghaz, M. Vauhkonen, A. Seppänen, Three-dimensional electrical
2704 capacitance tomography – A tool for characterizing moisture transport properties of cement-
2705 based materials, *Mater. Des.* 181 (2019) 107967.
2706 <https://doi.org/10.1016/j.matdes.2019.107967>.
- 2707 [469] R. du Plooy, G. Villain, S. Palma Lopes, A. Ihamouten, X. Dérobert, B. Thauvin, Electromagnetic
2708 non-destructive evaluation techniques for the monitoring of water and chloride ingress into
2709 concrete: a comparative study, *Mater. Struct.* 48 (2015) 369–386.
2710 <https://doi.org/10.1617/s11527-013-0189-z>.
- 2711 [470] X. Dérobert, J.F. Lataste, J.-P. Balayssac, S. Laurens, Evaluation of chloride contamination in
2712 concrete using electromagnetic non-destructive testing methods, *NDT E Int.* 89 (2017) 19–29.
2713 <https://doi.org/10.1016/j.ndteint.2017.03.006>.
- 2714 [471] Y. Seguí Femenias, U. Angst, F. Moro, B. Elsener, Development of a novel methodology to assess
2715 the corrosion threshold in concrete based on simultaneous monitoring of pH and free chloride
2716 concentration, *Sensors*. 18 (2018) 3101. <https://doi.org/10.3390/s18093101>.
- 2717 [472] Z. Zhang, J. Hu, Y. Ma, Y. Wang, H. Huang, Z. Zhang, J. Wei, S. Yin, Q. Yu, A state-of-the-art review
2718 on Ag/AgCl ion-selective electrode used for non-destructive chloride detection in concrete,
2719 *Compos. Part B Eng.* (2020) 108289. <https://doi.org/10.1016/j.compositesb.2020.108289>.
- 2720 [473] O. Anterrieu, B. Giroux, E. Gloaguen, C. Carde, Non-destructive data assimilation as a tool to
2721 diagnose corrosion rate in reinforced concrete structures, *J. Build. Eng.* 23 (2019) 193–206.
2722 <https://doi.org/10.1016/j.jobbe.2019.01.033>.

